



저작자표시-비영리-변경금지 2.0 대한민국

이용자는 아래의 조건을 따르는 경우에 한하여 자유롭게

- 이 저작물을 복제, 배포, 전송, 전시, 공연 및 방송할 수 있습니다.

다음과 같은 조건을 따라야 합니다:



저작자표시. 귀하는 원저작자를 표시하여야 합니다.



비영리. 귀하는 이 저작물을 영리 목적으로 이용할 수 없습니다.



변경금지. 귀하는 이 저작물을 개작, 변형 또는 가공할 수 없습니다.

- 귀하는, 이 저작물의 재이용이나 배포의 경우, 이 저작물에 적용된 이용허락조건을 명확하게 나타내어야 합니다.
- 저작권자로부터 별도의 허가를 받으면 이러한 조건들은 적용되지 않습니다.

저작권법에 따른 이용자의 권리는 위의 내용에 의하여 영향을 받지 않습니다.

이것은 [이용허락규약\(Legal Code\)](#)을 이해하기 쉽게 요약한 것입니다.

[Disclaimer](#)

工學博士學位論文

**Fabrication of SiO₂/TiO₂ Core/Shell &
Hollow Nanospheres and Their
Applications: Photocatalyst, Drug
Delivery, and Electrorheological Fluid**

실리카/티타니아 코어/셸과 중공구조
구형나노입자의 제조와 응용: 광촉매,
약물전달체, 전기유변유체

2012年 8月

서울대학교 大學院

化學生物工學部

金 粲 會

Fabrication of SiO ₂ /TiO ₂ Core/Shell & Hollow Nanospheres and Their Applications: Photocatalyst, Drug Delivery, and Electrorheological Fluid					
2012					
金榮會					
↑ 2cm ↓					
	↑ 2.5cm ↓	↑ 4cm ↓	↑ 3cm ↓	↑ 2cm ↓	

Fabrication of SiO₂/TiO₂ Core/Shell & Hollow Nanospheres and Their Applications: Photocatalyst, Drug Delivery, and Electrorheological Fluid

실리카/티타니아 코어/셸과 중공구조 구형나노입자의 제조와 응용:
광촉매, 약물전달체, 전기유변유체

指導教授 張 正 植

이 論文을 工學博士 學位論文으로 提出함

2012年 6月

서울大學校 大學院
化學生物工學部
金 榮 會

金榮會의 工學博士 學位論文을 認准함

2012年 6月

委 員 長 _____ (인)

副委員長 _____ (인)

委 員 _____ (인)

委 員 _____ (인)

委 員 _____ (인)

**Fabrication of SiO₂/TiO₂ Core/Shell &
Hollow Nanospheres and Their
Applications: Photocatalyst, Drug
Delivery, and Electrorheological Fluid**

by

Chanhoi Kim

Submitted to the Graduate School of Seoul National
University in Partial Fulfillment of the Requirements for the
Degree of Doctor of Philosophy

August, 2012

Thesis Adviser: Jyongsik Jang

학위논문 원문제공 서비스에 대한 동의서

본인의 학위논문에 대하여 서울대학교가 아래와 같이 학위논문 제공하는 것에 동의합니다.

1. 동의사항

- ① 본인의 논문을 보존이나 인터넷 등을 통한 온라인 서비스 목적으로 복제할 경우 저작물의 내용을 변경하지 않는 범위 내에서의 복제를 허용합니다.
- ② 본인의 논문을 디지털화하여 인터넷 등 정보통신망을 통한 논문의 일부 또는 전부의 복제, 배포 및 전송 시 무료로 제공하는 것에 동의합니다.

2. 개인(저작자)의 의무

본 논문의 저작권을 타인에게 양도하거나 또는 출판을 허락하는 등 동의 내용을 변경하고자 할 때는 소속대학(원)에 공개의 유보 또는 해지를 즉시 통보하겠습니다.

3. 서울대학교의 의무

- ① 서울대학교는 본 논문을 외부에 제공할 경우 저작권 보호장치(DRM)를 사용하여야 합니다.
- ② 서울대학교는 본 논문에 대한 공개의 유보나 해지 신청 시 즉시 처리해야 합니다.

논문제목: Fabrication of SiO₂/TiO₂ Core/Shell & Hollow Nanospheres and Their Applications

학위구분 : 석사 □ · 박사 ■

학 과 : 화학생물공학부

학 번 : 2007-23081

연 락 처 : 02-880-8348

저 작 자 : 김 찬 회 (인)

제 출 일 : 2012 년 8 월 일

서울대학교총장 귀하

Abstract

Fabrication of SiO₂/TiO₂ Core/Shell & Hollow Nanospheres and Their Applications: Photocatalyst, Drug Delivery, and Electrorheological Fluid

Chanhoi Kim

School of Chemical and Biological Engineering

The Graduate School

Seoul National University

Nanomaterials are very small materials which have smaller size than 100 nanometers in at least one dimension. These materials exhibit distinctive characteristics induced by extremely high surface area to volume ratio of the materials. The distinctive characteristics of nanomaterials has been paid a considerable attention and widely used in many areas such as electronics, optics, energy management, structural materials, functional surfaces, construction, information technology, pharmaceutical and medical field, and so on. Thus, a large effort has been devoted to synthesis of conventional

materials in nanoscale size over the last decade.

These days, fabrication and design of nanostructures which have various shapes and sizes have been highlighted as main research theme in nanotechnology. Fabrication and design of nanostructures in various shapes and sizes have made it possible to not only enhance performances, but also develop new functions in many fields. Typical nanostructures widely studied are core/shell nanoparticles and hollow nanoparticles.

Core/shell nanoparticles are structured nanoparticles that consist of a core of one material and a coating shell of another material. The introduced shell layer provides an understanding of factor governing colloidal interactions and stabilization. Core/shell nanostructures tailor the surface properties of particles and are accomplished by coating or encapsulating core materials within shell of preferred material. The introduced core can serve color, fluorescence, magnetism, drug reservoir, *etc.* The coating shell layer on core materials changes the charge, functionality, and reactivity of the surface, resulting in increased stability, and dispersibility. For these reasons, core/shell materials have the crucial meaning in the application fields.

Hollow nanoparticle is a special kind of core/shell nanoparticle having emptiness as a core. The void space of hollow nanostructures could lead to low density, large specific area, modulate refractive index, mechanical and

thermal stabilities, and surface permeability. These hollow nanoparticles have a great possibility in various application fields such as catalysis, coatings, composite materials, cosmetics, dyes, ink, artificial cells, and fillers. Furthermore, the large fraction of void space in hollow nanoparticles can be used as a carrier for controllable release of drugs in the pharmaceutical fields.

This dissertation describes novel method to fabricate $\text{SiO}_2/\text{TiO}_2$ core/shell and hollow nanospheres and their applications. SiO_2/N -doped TiO_2 core/shell nanospheres, $\text{SiO}_2/\text{TiO}_2$ hollow nanospheres, and Ba-doped $\text{SiO}_2/\text{TiO}_2$ hollow nanospheres are fabricated using colloidal SiO_2 as templates. The prepared nanomaterials are applied to photocatalyst for decomposition of organic molecules, nanocarrier for targeted drug delivery, and efficient ER fluid, respectively. Each nanosphere was deliberately designed and customized for superior performance in specific applications.

Keywords: Nanomaterials; Nanoparticle; Colloidal nanosphere; Core/shell nanosphere; Hollow nanosphere; SiO_2 ; Silica; TiO_2 ; Titania; BaTiO_3 ; Barium titanate; Photocatalyst; Drug delivery; Electrorheological fluid.

Student Number: 2007-23081

List of Abbreviations

ATP: adenosine triphosphate

Ba-HNS: Barium doped SiO₂/TiO₂ hollow nanosphere

BET: Brunauer-Emmett-Teller

CPT: camptothecin

DDS: drug delivery system

DLS: dynamic light scattering

DRS: diffuse reflectance spectra

EDX: energy-dispersive X-ray spectroscopy

ER: electrorheological

FACS: flow cytometry

FITC: fluorescein isothiocyanate

GER: giant electrorheological

HNS: SiO₂/TiO₂ hollow nanosphere

HR-TEM: high resolution-transmission electron microscopy

ICP: Inductively coupled plasma

N-TiO₂: nitrogen-doped titania

PBS: phosphate buffered saline

SNTCN: SiO₂/nitrogen-doped TiO₂ core/shell nanosphere

TEM: transmission electron microscopy

TOC: total organic carbon

TTIP: titanium(IV) tetraisopropoxide

VDP: vapor deposition polymerization

XPS: X-ray photoelectron spectroscopy

XRD: X-ray diffraction

List of Figures

- Figure 1.** Surface area to volume ratio of materials as a function of size.
- Figure 2.** Surface area to volume ratio of spherical materials as a function of diameter.
- Figure 3.** A schematic diagram of the fabrication of nanostructure via template method.
- Figure 4.** Diverse properties of core/shell nanoparticles changing the composition of core and shell.
- Figure 5.** TEM images of (A) silica particle and silica/PMMA core/shell particles with various shell thickness (MMA/silica weight ratio of (B) 0.25, (C) 0.75, and (D) 1.5).
- Figure 6.** Various nanostructures with (A) spherical, (B) cubic, and (C) cylindrical topologies synthesized using Kirkendall effect.
- Figure 7.** The migration of a metal (Ni) occurring at the interface between a metal (Ni) and an alloy (NiO) during synthesis of NiO hollow nanoparticle. (1) Nickel diffuses across the Ni/NiO interface only and (2) vacancies are injected at the interface and diffuse to the void. (3) The void nucleates when vacancies supersaturate. (4) The shell remains the same thickness where the void nucleated,

because little lateral Ni diffusion occurs along the void/shell interface or in the NiO shell. (5) Toward the end of oxidation, the core becomes a small ball whose oxidation might be slowed by the reduced Ni/NiO interfacial area and the thick NiO layer through which Ni cations must diffuse.

Figure 8. A schematic diagram of mechanism of photocatalytic reaction.

Figure 9. A schematic diagram of the microstructure change of ER fluid.

Figure 10. A schematic diagram of the fabrication of SiO₂/N-doped TiO₂ core/shell nanospheres.

Figure 11. TEM image of SiO₂ nanospheres with an average diameter of 30 nm.

Figure 12. TEM image of SNTCNs calcined at 250 °C with diameter of 40 nm.

Figure 13. Size distributions of (A) SiO₂ nanospheres and (B) SNTCN250.

It was prepared by measuring the diameters of hundred SiO₂ nanospheres and SNTCNs directly from TEM images.

Figure 14. Full-scale X-ray photoelectron spectroscopy spectra of SNTCNs calcined at different temperatures (150, 250, 350, 450, and 550 °C).

Figure 15. Enlarged N 1s regions of the SNTCN calcined at different

temperatures (150, 250, 350, 450, and 550 °C).

Figure 16. Full-scale X-ray photoelectron spectroscopy spectra of SNTCNs calcined at 250 °C with various volume ratio of triethylamine to TTIP.

Figure 17. Enlarged N 1s regions of SNTCNs calcined at 250 °C with various volume ratio of triethylamine to TTIP.

Figure 18. Uv-vis diffuse reflectance spectroscopy spectra for P-25 and SNTCNs calcined at different temperatures.

Figure 19. Uv-vis diffuse reflectance spectroscopy spectra for NSTCS calcined at 250 °C with various volume ratio of triethylamine to TTIP.

Figure 20. Structure of methylene blue.

Figure 21. Photodecomposition of methylene blue by P-25 and SNTCNs calcined at different temperatures

Figure 22. Photodecomposition of methylene blue by P-25 and SNTCNs calcined at 250 °C with various volume ratio of triethylamine to TTIP.

Figure 23. XRD patterns of SNTCNs with different calcination temperatures.

Figure 24. TEM images of Degussa P-25.

Figure 25. TEM images of SNTCN550.

Figure 26. A schematic illustration of fabrication of antibody conjugated silica/titania hollow nanospheres (HNS) containing CPT.

Figure 27. TEM images of silica/titania hollow nanospheres (HNSs) with an average diameter of 50 nm at (A) low and (B) high magnification.

Figure 28. SEM image of HNSs with an average diameter of 50 nm.

Figure 29. Energy dispersive X-ray (EDX) spectra of (A) the $\text{SiO}_2/\text{TiO}_2$ core/shell nanospheres and (B) the hollow nanospheres.

Figure 30. Size distributions of (A) HNSs and (B) herceptin conjugated HNSs (HER-HNSs) measured by electrophoretic light scattering spectroscopy (ELS).

Figure 31. Nitrogen adsorption isotherm of the hollow nanospheres

Figure 32. Pore size distribution of HNSs.

Figure 33. Time-dependent release profile of CPT from HNS into 0.1 M phosphate buffer solution (PBS) and DMSO.

Figure 34. Live cell fluorescent images of SK-BR-3 human breast cancer cells incubated with $10 \mu\text{g mL}^{-1}$ of HNS, HER-HNS, HNS-CPT, HER-HNS-CPT or the same concentration of CPT in PBS (20 ng mL^{-1}) for 24 h. Cells were stained with annexin V conjugated Alexa 488 (aV; green) and propidium iodide (PI; red) for

visualizing apoptosis and necrosis in cells. DIC images were obtained at the same time, corresponding to the fluorescent images (Scale bars: 20 μm).

Figure 35. Live cell fluorescent images of SK-BR-3 cells treated with 10 $\mu\text{g mL}^{-1}$ of HNS-CPT and HER-HNS-CPT for 30 min, 2 h, and 12 h. Cells were stained with annexin V conjugated Alexa 488 (aV; green) and propidium iodide (PI; red) for visualizing apoptosis and necrosis in cells. DIC images were obtained at the same time, corresponding to the fluorescent images (Scale bars: 20 μm).

Figure 36. Quantitative assessment of apoptosis and necrosis conducted by flow cytometry analysis with aV and PI double staining. SK-BR-3 was incubated with 25 $\mu\text{g mL}^{-1}$ of the nanospheres or the same concentration of CPT in PBS (50 ng mL^{-1}) for A) 24 h and B) 48 h. Each experiment was performed in triplicate.

Figure 37. Live cell fluorescent images of SK-BR-3 cells incubated with A) CPT suspension in 0.1 M PBS, and B) CPT dissolved in DMSO. Apoptotic and necrotic cells were stained with aV and PI. DIC images were acquired at the same time, corresponding to the fluorescent images (Scale bars: 20 μm).

Figure 38. Cellular uptake of HNS and HER-HNS in SK-BR-3 cells ($25\ \mu\text{g mL}^{-1}$) for 24 h. TEM images show HNS and HER-HNS internalized in the cells. Lower images display magnified regions bounded by red boxes in the TEM images of HNS and HER-HNS, respectively. White arrows indicate location of HNSs and HER-HNSs.

Figure 39. Viability for SK-BR-3 human breast cancer cells incubated with CPT, HNS, HER-HNS, HNS-CPT, and HER-HNS-CPT for 24 h. CPT was used at CPT-equivalent concentrations (20, 50, and $200\ \text{ng mL}^{-1}$). Viability was measured by quantifying the amount of ATP in metabolically active cells. Values exhibit mean \pm SD and each experiment was performed in triplicate. *Statistically significant difference from control ($P < 0.05$).

Figure 40. Viability for RAW264.7 mouse macrophage cells incubated with CPT, HNS, HER-HNS, HNS-CPT, and HER-HNS-CPT for 24 h. CPT was used at CPT-equivalent concentrations (20, 50, and $200\ \text{ng mL}^{-1}$). Viability was measured by quantifying the amount of ATP in metabolically active cells. Values exhibit mean \pm SD and each experiment was performed in triplicate. *Statistically significant difference from control ($P < 0.05$).

Figure 41. Viability for SK-BR-3 human breast cancer cells incubated with CPT, HNS, HER-HNS, HNS-CPT, and HER-HNS-CPT in DMEM for 24 h. CPT was used at CPT equivalent concentrations (20, 50, and 200 ng mL⁻¹). Viability was measured by quantifying the amount of ATP in metabolically active cells. Values exhibit mean \pm SD and each experiment was performed in triplicate. *Statistically significant difference from control (P<0.05).

Figure 42. Schematic illustration for fabrication of Ba-HNSs from SiO₂/TiO₂ core/shell nanospheres.

Figure 43. TEM images of (A) the SiO₂/TiO₂ core/shell nanospheres and (B) the Ba-HNSs.

Figure 44. Nitrogen adsorption isotherm of the SiO₂/TiO₂ core/shell nanospheres and the Ba-HNSs.

Figure 45. TEM images of the HNPs fabricated by the same method for Ba-HNSs except that Ba²⁺ ions were alternated with NH₄⁺ ions.

Figure 46. EDX spectra of (A) Ba-HNSs and (B) the SiO₂/TiO₂ core/shell nanospheres. The signal of carbon originated from the carbon tape to fix the samples.

Figure 47. XRD patterns of the Ba-HNSs and the HNSs.

Figure 48. (A) Full-scale X-ray photoelectron spectroscopy spectra and (B) Ba 3d photoelectron spectra of the Ba-HNSs and the HNSs.

Figure 49. Ti 2p photoelectron spectra of the Ba-HNSs and the HNSs. Red and blue spectra are assigned to TiO_2 and BaTiO_3 , respectively.

Figure 50. O 1s photoelectron spectra of the Ba-HNSs and the HNSs. Red and blue spectra are assigned to $\text{SiO}_2/\text{TiO}_2$ composite and BaTiO_3 , respectively.

Figure 51. Si 2p photoelectron spectra of the Ba-HNSs and the HNSs. Red and blue spectra are assigned to SiO_2 and BaSiO_3 , respectively.

Figure 52. Photograph of ER fluids based on 25 vol% of Ba-HNSs and commercial BaTiO_3 nanopowders.

Figure 53. TEM image of the commercial BaTiO_3 nanopowders.

Figure 54. Microscope images of electrorheological chain formation in ER fluid of Ba-HNSs (5 vol% in silicon oil) under an applied electric field of 1 kV/mm. The gap between two electrodes was fixed to 1.0 mm.

Figure 55. Dynamic yield stress as a function of volume fraction for ER fluids based on the Ba-HNSs, the HNSs and the Ba-TiO_3 nanopowders under 5 kV/mm of electric field strength. The fitting lines serve to guide the eye.

Figure 56. Dynamic yield stress of ER fluids based on the Ba-HNSs, the HNSs and the Ba-TiO₃ nanopowders as a function of electric field strength (25 vol% in silicon oil). The fitting lines serve to guide the eye.

Figure 57. Change in the shear stress of ER fluids based on the Ba-HNSs and the HNSs (25 vol% in silicon oil) under switching on and off the applied electric field. Applied electric field is switched on and off alternately. t_1 and t_2 are times it takes to reach 90 % of maximum shear stress under electric field of 5 kV/mm.

List of Tables

Table 1. Classification of colloids.

Table 2. Elemental contents of N-doped TiO₂ shell measured by analysis of XPS binding energy peaks. Total N (1s) includes doped nitrogen and absorbed nitrogen content.

Table 3. BET surface area of Degussa P-25 and NSTCS calcined at different temperature.

Table 4. Elemental contents of Ba-HNS and HNS by EDX analysis. Carbon and oxygen contents were excluded because they originated from carbon tape to fix Ba-HNS and HNS.

Contents

Abstract.....	i
List of Abbreviations.....	iv
List of Figures.....	vi
List of Tables.....	xv
Contents	xvi
Chapter 1 Introduction	1
1.1 Background	1
1.1.1 Nanostructures	1
1.1.1.1 Nanomaterials	1
1.1.1.2 Colloidal nanoparticles.....	5
1.1.1.3 Template method for nanostructures	8
1.1.1.4 Core/shell nanoparticles	10
1.1.1.5 Hollow nanoparticles	12
1.1.2 Characteristics of SiO ₂ and TiO ₂	17
1.1.2.1 SiO ₂	17
1.1.2.2 TiO ₂	18

1.1.3	Application fields.....	19
1.1.3.1	Photocatalysts.....	19
1.1.3.2	Drug delivery system	22
1.1.3.3	Electrorheological fluids	24
1.2	Objectives and Outline of the study	27
1.2.1	Objectives	27
1.2.2	Outline	27
Chapter 2 Experimental Details		33
2.1	SiO ₂ /TiO ₂ core/shell nanospheres for photocatalyst under visible light.....	33
2.1.1	Fabrication of SiO ₂ /N-doped TiO ₂ core/shell nanospheres.....	33
2.1.2	Visible light photocatalytic properties of SiO ₂ /N-doped TiO ₂ core/shell nanospheres.....	34
2.2	SiO ₂ /TiO ₂ hollow nanospheres for targeted drug delivery system	35
2.2.1	Fabrication of SiO ₂ /TiO ₂ hollow nanospheres	35
2.2.2	Antibody conjugation on SiO ₂ /TiO ₂ hollow nanospheres.....	36
2.2.3	Anticancer drug loading into antibody conjugation on SiO ₂ /TiO ₂ hollow nanospheres.....	36

2.2.4	Drug delivery properties of Antibody conjugation on SiO ₂ /TiO ₂ hollow nanospheres with anticancer drug.....	37
2.3	Ba-doped SiO ₂ /TiO ₂ hollow nanospheres for efficient electrorheological fluid	41
2.3.1	Fabrication of Ba-doped SiO ₂ /TiO ₂ hollow nanospheres from SiO ₂ /TiO ₂ core/shell nanospheres	41
2.3.2	Fabrication of ER fluid based on Ba-doped SiO ₂ /TiO ₂ hollow nanospheres.....	42
2.3.3	Electrorheological properties of ER fluid based on Ba- doped SiO ₂ /TiO ₂ hollow nanospheres.....	42
2.4	Instrumental	44
Chapter 3 Results and Discussion		46
3.1	SiO ₂ /TiO ₂ core/shell nanospheres for photocatalyst under visible light.....	46
3.1.1	Fabrication of SiO ₂ /N-doped TiO ₂ core/shell nanospheres.....	46
3.1.2	Visible light photocatalytic properties of SiO ₂ /N-doped TiO ₂ core/shell nanospheres.....	59
3.2	SiO ₂ /TiO ₂ hollow nanospheres for targeted drug delivery system	72

3.2.1	Fabrication of SiO ₂ /TiO ₂ hollow nanospheres	72
3.2.2	Antibody conjugation on SiO ₂ /TiO ₂ hollow nanospheres.....	78
3.2.3	Anticancer drug loading into antibody conjugation on SiO ₂ /TiO ₂ hollow nanospheres.....	80
3.2.4	Drug delivery properties of Antibody conjugation on SiO ₂ /TiO ₂ hollow nanospheres with anticancer drug.....	85
3.3	Ba-doped SiO ₂ /TiO ₂ hollow nanospheres for efficient electrorheological fluid	98
3.3.1	Fabrication of Ba-doped SiO ₂ /TiO ₂ hollow nanospheres from SiO ₂ /TiO ₂ core/shell nanospheres	98
3.3.2	Fabrication of ER Fluid based on Ba-doped SiO ₂ /TiO ₂ hollow nanospheres.....	113
3.3.3	Electrorheological properties of ER fluid based on Ba- doped SiO ₂ /TiO ₂ hollow nanospheres.....	126
Chapter 4 Conclusions		124
References		128
국문초록		140

Chapter 1 Introduction

1.1 Background

1.1.1 Nanostructures

1.1.1.1 Nanomaterials

In the past few decades, nanomaterials attract tremendous attention in physics, chemistry, engineering, and biology [1-3]. The fabrication and application of nanomaterials with novel properties have been one of the century's key technology developments in various technological fields such as electronics, energy management, structural materials, functional surfaces, construction, and information technology, but also in the pharmaceutical and medical field [4-6]. Nanomaterials have smaller size than 100 nanometers (nm) in at least one dimension [7], though this term is sometimes also used for materials smaller than one micrometer. As materials become small, surface area to volume ratio of the materials increases (**Figure 1**). Additionally, surface area to volume ratio increases exponentially as a function of diameter reduction. **Figure 2** shows that spherical particles in

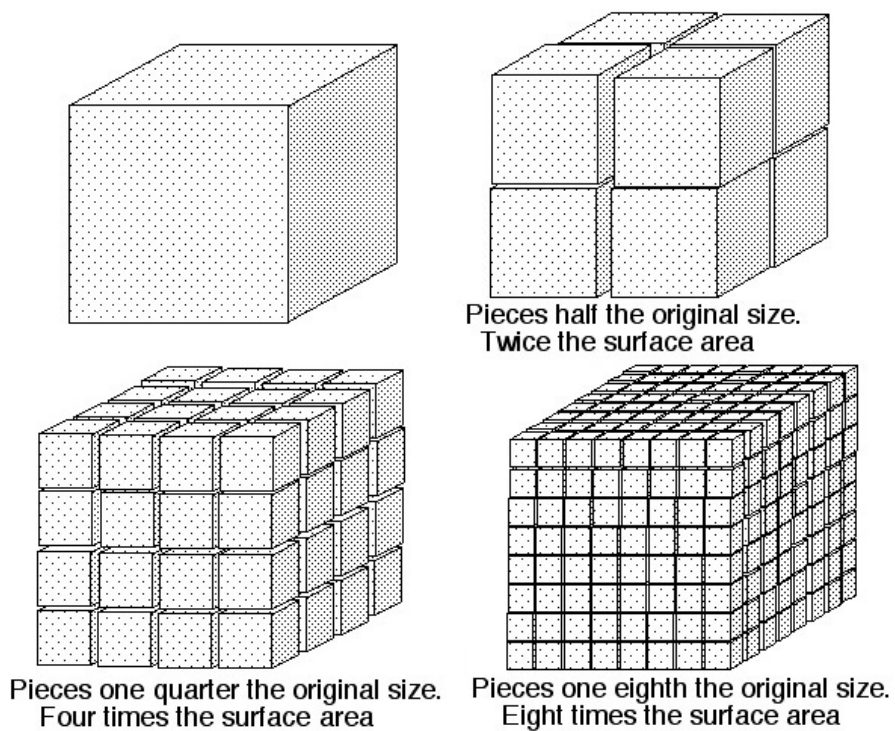


Figure 1. Surface area to volume ratio of materials as a function of size.

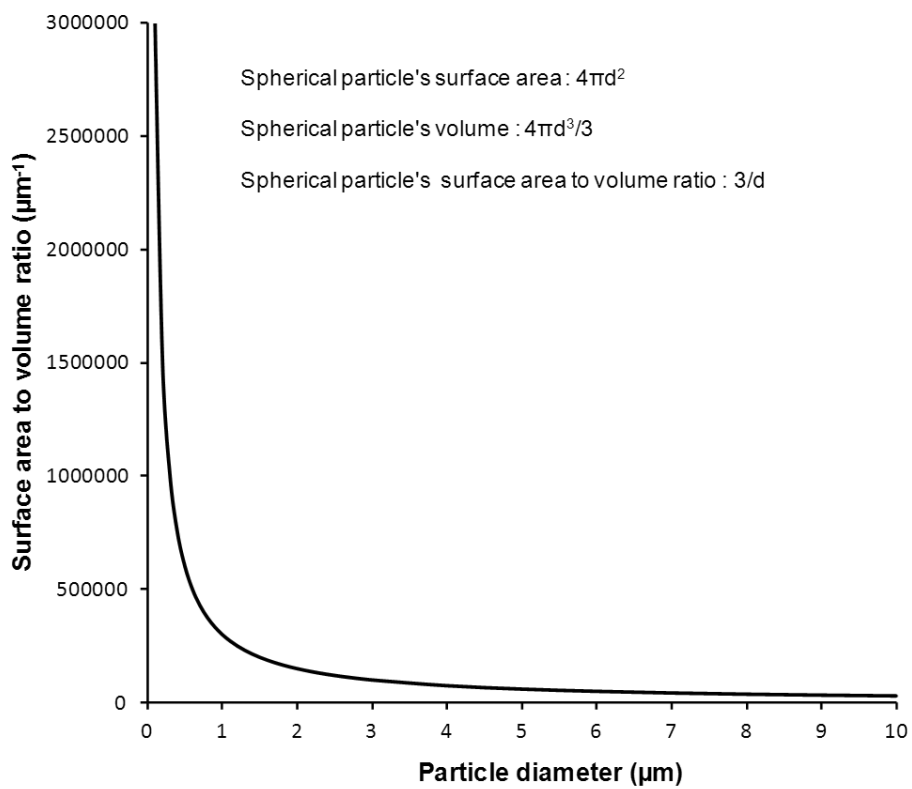


Figure 2. Surface area to volume ratio of spherical materials as a function of diameter.

nanometer scale have extremely high surface area to volume ratio in comparison to micrometer scale. Tremendous surface-to-volume ratio of nanomaterials makes unique and useful properties different with their corresponding bulk materials. A typical example is the “quantum size effect” where the electronic properties of solids are altered with great reductions in particle size [8]. This effect does not come into play by going from macro to micro dimensions. However, it becomes pronounced when the nanometer size range is reached. A certain number of physical properties alter with the change from macroscopic systems. Besides change of physical properties, small dimensions of nanomaterials also enable recent advances in the development of electronic, electrochemical, chemical, rheological applications as well as biological fields such as drug delivery, gene therapy, and medical diagnostics. Furthermore, nanomaterials have the many atoms on the surface and interface which can make contact with other materials. Due to this property, synthesis of nanomaterials has been widely studied in catalyst, absorbents, composite fillers, etc for performance improvement.

To date, diverse nanostructured materials such as nanoparticles, nanorods, nanofibers, nanotubes and mesoporous materials were prepared by various preparation methods [9-12]. A rich variety of chemical and physical techniques have been developed for the size- and shape-control of nano-

materials which shows unique and exceptional properties compared to conventional bulk materials. Despite a large number of achievements in nanomaterials, lots of studies to fabricate the novel class of nanomaterials are still reported for specific functions and performance improvements. Lately, techniques for mass production of uniform nanomaterials have also received considerable attention to use them in industry.

1.1.1.2 Colloidal nanoparticles

Colloid science is involved in branches of chemistry, physics, nanoscience and other fields dealing with colloids, which are heterogeneous systems consisting of a mechanical mixture of particles between 1 nm and 1000 nm dispersed in a continuous medium [13]. A colloidal system is comprised of two separate phases, a dispersed phase (or internal phase) and a continuous phase (or dispersion medium). A colloidal system may be solid, liquid, or gaseous (**Table 1**). The colloidal particles of dispersed component are only suspended in the mixture, unlike in a solution, in which they are completely dissolved. Colloids are familiar in our life, and so have been of scientific and technological interest. In addition to naturally occurring colloids, modern chemistry utilizes nanomaterials to create colloids with

Table 1. Classification of colloids.

Medium/Phases		Dispersed phase		
		Gas	Liquid	Solid
Continuous medium	Gas	None	Liquid aerosol (e.g. fog, mist)	Solid aerosol (e.g. cloud, smoke)
	Liquid	Foam (e.g. whipped cream)	Emulsion (e.g. milk, hand cream)	Sol (e.g. blood, pigmented ink)
	Solid	Solid foam (e.g. aerosol, Styrofoam)	Gel (e.g. jelly, opal)	Solid Sol (e.g. pearl, cranberry glass)

diverse and tailored composition in recent years. With synthetic capability for a variety of colloidal nanomaterials, efforts are poured over to develop their modular assembly as a general strategy for nanostructured materials with new properties [14-18]. Also, the nano sized colloidal materials exhibit quantum size effects and have attracted attention because of their unique properties and the potential to exploit them in what has been termed, somewhat loosely, “nanotechnology”. For “nano-devices” or “nanoapplications”, the reliable routes for colloidal structures with controllable surface, size, and composition have been required.

As mentioned above, colloid are dispersed or suspended in the solvent and the dispersion of colloidal nanoparticles could be understood by the proper characterization of the particle-solution interface [19]. Most colloids generally have a surface electric charge when dispersed in a polar medium such as water. The electric charge can be brought about through the ionization of surface functional groups on the colloid, ion adsorption, and unequal ion dissolution of the colloidal materials. An important consequence of the charge on the particle surface is that an electrical double layer around the colloid is produced in polar solutions. The double layer consists of a surface charge and a diffuse ion region in which ions are distributed in response to the electrical forces operating in the system and random thermal

motion. Therefore, under solution conditions of low ionic strength and moderate surface potentials, the electrostatic repulsion between particles is normally sufficient to prevent the attractive forces from causing the particles to aggregate. This property is useful in fabrication of uniform and well-dispersed nanomaterials. Furthermore, these colloidal nanomaterials are widely used as templates for synthesis of nanostructures with varied shapes.

1.1.1.3 Template methods for nanostructures

Numerous synthetic routes for nanostructured materials has been developed for last few decades. Among various ways, template method is widely preferred to prepare nanomaterials [20-23]. Template method is based on the inclusion of guests such as inorganic or organic components inside the void space of host materials (**Figure 3**). These voids play a role of the template and nanomaterials with versatile structures are synthesized by manipulating shape, size, and orientation of the template. The template synthesizing route of nanostructures includes soft template and hard template methods. While the former exploits molecular self-assembly as template to form nanostructures, the latter replicates nanostructure of template by physical or chemical interactions. Surfactant, cyclodextrin, and liquid crystal



Figure 3. A schematic diagram of the fabrication of nanostructure via template method.

are typical soft templates and inorganic nanoparticles, polymeric colloids, and anodic aluminum oxide (AAO) membranes are widely used as hard template.

1.1.1.4 Core/shell nanoparticles

Core/shell nanoparticles are structured nanoparticles that consist of a core of one material and a coating shell of another material. The core/shell nanoparticles are considered to be important in the area of colloid and interface science. The introduced shell layer provides an understanding of factor governing colloidal interactions and stabilization. Core/shell nanostructures tailor the surface properties of particles and are accomplished by coating or encapsulating core materials within shell of preferred material. The introduced shell layer on core materials changes the charge, functionality, and reactivity of the surface, resulting in increased stability, and dispersibility [24-27].

In addition to surface chemistry, core/shell materials have the crucial meaning in the application fields owing to physical and chemical characteristics. The composition of the core and shell can be diversified to give a wide range of different properties (**Figure 4**). Therefore, methods to

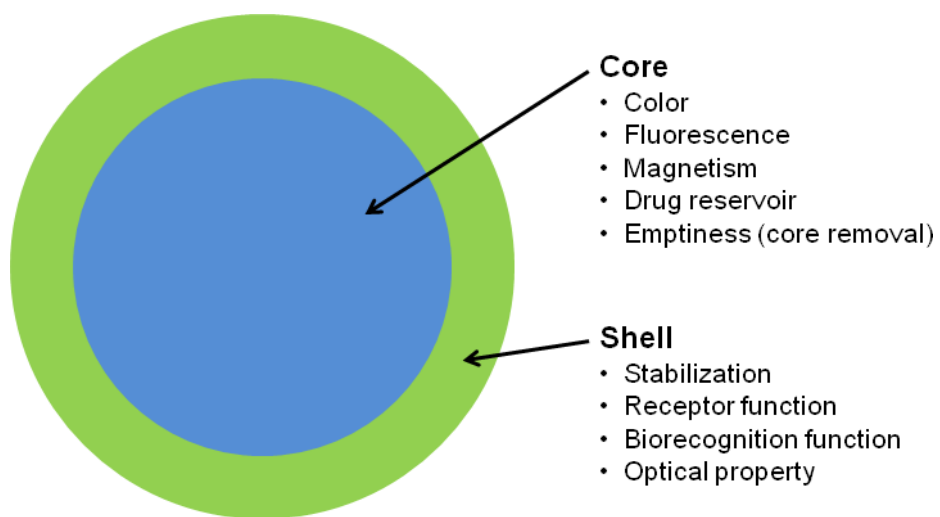


Figure 4. Diverse properties of core/shell nanoparticles changing the composition of core and shell.

engineer multifunctional core/shell nanomaterials with controlled precision have been studied. Among several strategies, vapor deposition polymerization allows the simple way for inorganic particle/polymer core/shell materials [28]. Vapor deposition polymerization facilitates easy control of polymer shell thickness by tuning the amount of monomer as shown in **Figure 5**.

1.1.1.5 Hollow nanoparticles

Lately, the synthesis of hollow nanoparticles has attracted much attention in the chemistry and material communities [29-33]. The void space of hollow nanostructures could lead to low density, large specific area, modulate refractive index, mechanical and thermal stabilities, and surface permeability. These hollow nanoparticles have a great possibility in various application fields such as catalysis, coatings, composite materials, cosmetics, dyes, ink, artificial cells, and fillers [34]. Furthermore, the large fraction of void space in hollow nanoparticles can be used as a carrier for controllable release of drugs in the pharmaceutical fields [35].

Thus, numerous strategies were employed for the preparation of hollow nanostructures. Major routes to hollow nanostructures are as follows:

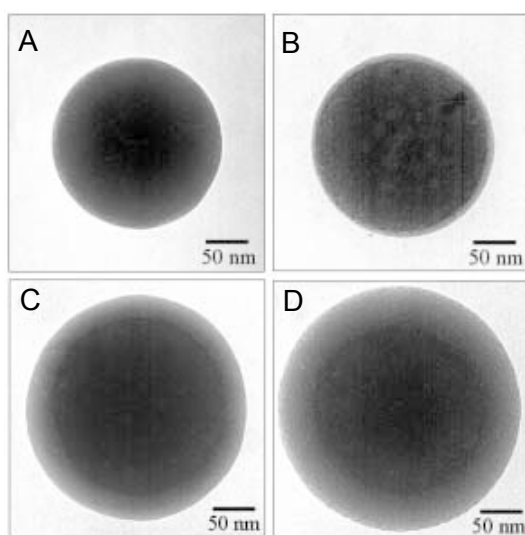


Figure 5. TEM images of (A) silica particle and silica/PMMA core/shell particles with various shell thickness (MMA/silica weight ratio of (B) 0.25, (C) 0.75, and (D) 1.5) [36].

1) template method, b) sonochemical method, and c) hydrothermal method. Among these methods, the use of sacrificial templates has proven successful to fabricate hollow spherical nanoparticles. Polymer nanoparticles such as latexes and polymeric micelles have been largely used as the sacrificial templates because it is easy to control the size, morphology, and surface functionality of the polymer nanoparticles. In general, latex particles are utilized for fabricating hollow particles with relatively larger diameters ranging from sub-micrometers to micrometers, while polymeric micelles are employed for smaller hollow particles with diameters of less than one hundred nanometers.

Although there have been many studies of the polymeric templates to fabricate hollow nanoparticles [37-40], a few has reported the use of inorganic templates due to their difficulty of core removal. However, it is possible to synthesize hollow nanoparticles with small size and uniform size distribution by the templates of inorganic nanoparticles in comparison to the polymeric templates. Lately, sacrificial template method using Kirkendall effect has a great deal of interest as an alternative synthetic way of versatile hollow nanostructures (**Figure 6**). The Kirkendall effect is the migration of markers occurring when markers are placed at the interface between a metal and an alloy, and the whole is heated to a temperature where diffusion is

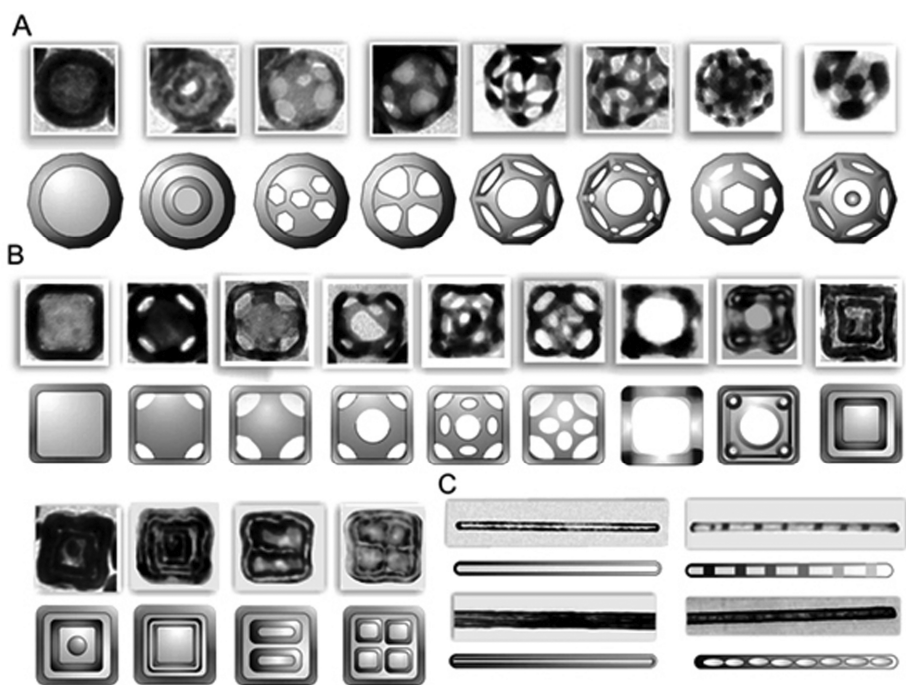


Figure 6. Various nanostructures with (A) spherical, (B) cubic, and (C) cylindrical topologies synthesized using Kirkendall effect [41].

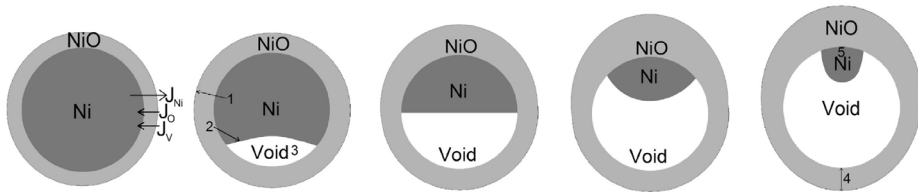


Figure 7. The migration of a metal (Ni) occurring at the interface between a metal (Ni) and an alloy (NiO) during synthesis of NiO hollow nanoparticle. (1) Nickel diffuses across the Ni/NiO interface only and (2) vacancies are injected at the interface and diffuse to the void. (3) The void nucleates when vacancies supersaturate. (4) The shell remains the same thickness where the void nucleated, because little lateral Ni diffusion occurs along the void/shell interface or in the NiO shell. (5) Toward the end of oxidation, the core becomes a small ball whose oxidation might be slowed by the reduced Ni/NiO interfacial area and the thick NiO layer through which Ni cations must diffuse [42].

possible; the markers will move towards the alloy region (**Figure 7**). The advances in fabrication of hollow nanoparticle have provided new opportunities to versatile application fields. However, for highly enhanced performance in application fields, it is still challenging to prepare uniform and non-agglomerated hollow nanomaterials with controllable size in the nanometer

1.1.2 Characteristics of SiO₂ and TiO₂

1.1.2.1 SiO₂

The chemical compound silicon dioxide, also known as silica, is an oxide of silicon with the chemical formula SiO₂. It is most commonly found in nature as sand or quartz, as well as in the cell walls of diatoms [43]. Silica is used primarily in the production of glass for windows, drinking glasses, beverage bottles, optical fibers and many other uses. Besides glass, it was important materials in many whiteware ceramics and food additives.

In these days, silica has received considerable attention in nanotechnology due to its easily controllable and diverse shapes by many synthetic ways, biocompatibility, and facile surface modification. One of the most widely used silica form in nanotechnology is colloidal silica, which is

employed for filler of composites, support of nanomaterials, template to fabricate nanomaterials, and so on. Mesoporous silica is a recently developed form of silica in nanotechnology [44,45]. It has large surface area and pore volume suitable for high performance catalyst supports, drug delivery, and biosensors [46-48]. Above these forms, various silica nanostructures have been reported and studied in diverse application fields.

1.1.2.1 TiO_2

Titanium dioxide, also known as titania, is the naturally occurring oxide of titanium, chemical formula TiO_2 . In general, TiO_2 is found to be rutile, anatase, and brookite forms in nature. The most crystalline form is rutile since it is equilibrium phase at all temperatures [49,50]. The metastable anatase and brookite phases both convert to rutile at high temperature [51].

TiO_2 has been commonly used as a pigment which is included in paints, plastics, cosmetics, and foods. Additionally, TiO_2 particles are good sources as sunscreen and thickener in cosmetic and skin care products. Recently, TiO_2 has received considerable attention due to its adequate properties for photocatalyst [52] and solar energy conversion based on dye, polymer, or quantum dot sensitized solar cells [53-55]. Since enlarging active site or

manipulating structure can enhance performances of the aforementioned catalysts and devices based on TiO_2 , there is a necessity for fabrication of TiO_2 nanomaterials. However, it is difficult to control fabrication of TiO_2 nanomaterials due to fast and strong reactivity of TiO_2 precursor such as titanium(IV) isopropoxide, titanium tetrachloride, titanium(IV) butoxide, etc. To overcome this problem, a large effort has been devoted to fabrication of TiO_2 nanomaterials. Although various TiO_2 nanomaterials have been prepared from versatile synthetic routes, it should be still required to fabricate the novel class of TiO_2 nanomaterials to tap the potential of TiO_2 as a material for renewable energy conversion.

1.1.3 Application fields

1.1.3.1 Photocatalysts

Photocatalyst can create electron-hole pairs generating free radicals able to undergo secondary reactions, when it is exposed to the photons (**Figure 8**). The strong oxidative potential of the positive holes from photocatalyst creates hydroxyl radicals by oxidizing water. The hydroxyl radicals have highly chemical reactivity, so much so that it can oxidize

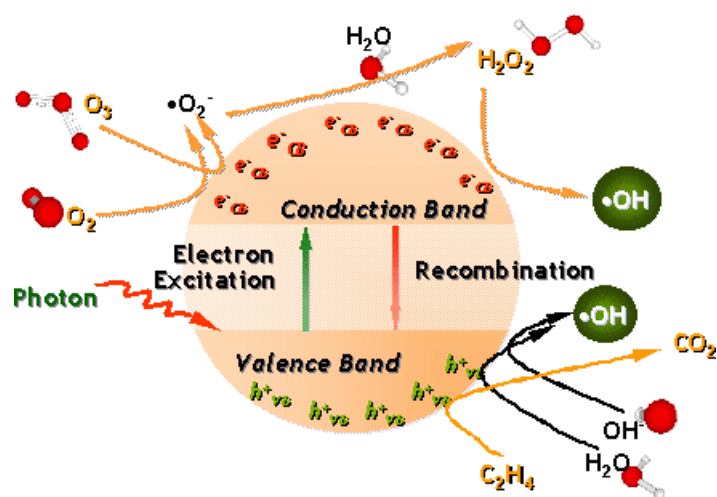


Figure 8. A schematic diagram of mechanism of photocatalytic reaction.

oxygen or organic materials directly. Such strong oxidization power of photocatalysts could be applied for the potential fields including water splitting, self-cleaning surface, and decomposition of organic pollutants [56-60].

TiO₂, ZnO, CdS, CdSe are well-known as a photocatalyst; TiO₂ is the most frequently used source for photocatalyst due to its low cost, abundant reserves, non-toxicity, chemical inertness, and photostability [61-63]. A considerable study has focused on improving the photocatalytic activities of TiO₂ by several methods [64-66]. In general, TiO₂ exhibits the restricted photocatalytic activity by the UV light as small fraction (5%) of the sunlight. Considering that the population of visible light in the sun light is as high as 45 % [67], it is necessary that TiO₂ have strong photocatalytic activity under visible light irradiation. To achieve the efficient photocatalytic activity from both visible and UV light in solar energy, TiO₂ has been doped with metallic and nonmetallic dopants such as transition metals, novel metals, rare earth metal, carbon, nitrogen, and sulfur [68-73]. From these researches, the doped TiO₂ showed the shift of absorption edge and resulted in the enhanced photocatalytic activity under visible light.

Besides the shift of TiO₂ adsorption edge, reducing recombination of photogenerated electron-hole pairs is widely used approach to enhance the

photocatalytic activity [74-76]. Introduction of novel metals, quantum dots, or carbon based materials on surface of TiO_2 enables the photogenerated electron-hole pairs to be separated for long time, which involves increase of photocatalytic activity.

1.1.3.2 Drug delivery system

Drug delivery system (DDS) is the process of administering an existing pharmaceutical compound to achieve a better therapeutic effect in humans or animals. Drug delivery technologies place great emphasis on modification of drug release profile, absorption, distribution and elimination for the benefit of improving product efficacy and safety, as well as patient convenience and compliance. Routes to delivery drugs are varied from injection to non-invasive peroral depending on properties of the drugs, and preferred routes are different chronologically. DDS has attracted a great deal of interest since developed drugs by DDS researches have low cost, require short research & development time, and show high probability of success in comparison to the conventional development of new pharmaceuticals.

Current efforts in DDSs are largely divided into two different types, sustained release formulations in which the drug is released over a period of

time in a controlled manner from a formulation and targeted delivery in which the drug is only active in the target area of the body. Of these, targeted delivery is considered as an ideal DDS, and a large effort has been devoted to development of targeted delivery of existing drugs. The advantages to the targeted delivery system is the reduction in the frequency of the dosages taken by the patient, having a more uniform effect of the drug, reduction of drug side effects, and reduced fluctuation in circulating drug levels, which are especially suitable characteristics to use anticancer drugs.

Recent advances in the synthesis of nanomaterials provided the key to achieve targeted DDS of anticancer using the nanomaterials as drug carriers [77-80]. The strategy for delivering nanocarriers to tumor was categorized into two ways: a) passive targeting such as nanoparticle (≤ 100 nm) accumulation into tumor *via* enhanced permeation and retention (EPR) effect and b) active targeting including ligand-receptor interaction between nanoparticle surface and cell membrane receptor [81]. For efficient anticancer drug delivery, both strategies could be employed to nanocarriers (e.g., small nanoparticles under 100 nm with monoclonal antibody grafting).

1.1.3.3 Electrorheological fluids

Electro-responsive electrorheological (ER) fluids are suspension of extremely fine non-conducting particles in an electrically insulating fluid, which show fascinating field-induced rheological properties such as a rapid and reversible change in suspension microstructures under an applied electrical field [82-86]. By controlling the electric field strength to vary the fibril structures, a micro structural transition of ER fluids from fluid-like to solid-like is obtained (**Figure 9**). All physical and mechanical changes induced by the applied electric fields are instantaneous (within a millisecond) and are reversible upon removal of the field. From schematic picture, particles form chains that span the gap between the field-generating electrodes. The reversible property of ER response, the significant change in viscosity and yield stress, and the short response times observed in these systems are desirable characteristics for various engineering applications such as torque transducers, vibration attenuators, control systems, and ER polishing. Therefore, ER phenomenon has been extensively studied due to the broad potential applications and scientific interests.

However, in spite of the broad interest, applications have been hampered by the weakness of the ER effect. Recently, nanomaterials have

been served into ER suspensions and are expected to provide the novel paradigm such as the giant electrorheological (GER) effect [87-89]. Considering that there is a little literature for nanostructure-based ER suspensions, it is important to investigate the parameter and effect of nanomaterials on ER system.

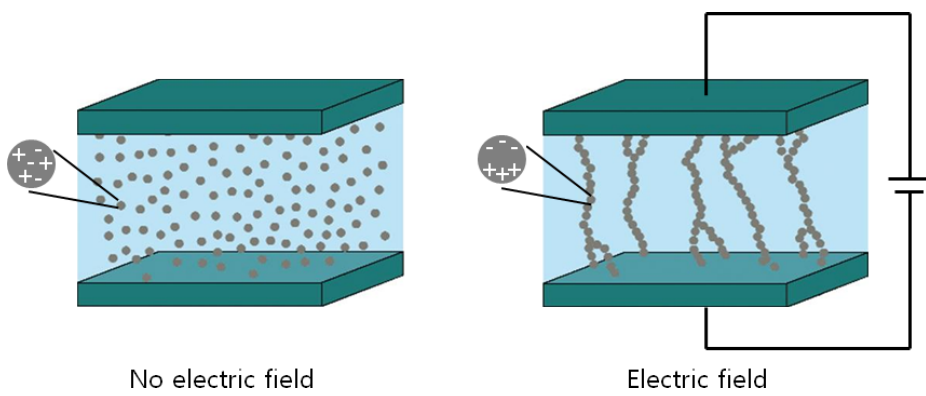


Figure 9. A schematic diagram of the microstructure change of ER fluid.

1.2 Objectives and Outline of the study

1.2.1 Objectives

The aim of this dissertation proposes novel method to fabricate $\text{SiO}_2/\text{TiO}_2$ core/shell and hollow nanospheres and their applications. SiO_2/N -doped TiO_2 core/shell nanospheres, $\text{SiO}_2/\text{TiO}_2$ hollow nanospheres, and Ba-doped $\text{SiO}_2/\text{TiO}_2$ hollow nanospheres are fabricated using colloidal SiO_2 as templates. The prepared nanomaterials are applied to photocatalyst for decomposition of organic molecules, nanocarrier for targeted drug delivery, and efficient ER fluid, respectively. Each nanosphere was deliberately designed and customized for superior performance in specific applications.

1.2.2 Outline

This dissertation focuses on the fabrication of $\text{SiO}_2/\text{TiO}_2$ core/shell and hollow nanospheres and their applications. In viewpoint of prepared nanomaterials and application field, this dissertation involves the following subtopics;

1. SiO₂/N-doped TiO₂ core/shell nanospheres for photocatalyst under visible light irradiation
2. SiO₂/TiO₂ hollow nanospheres for targeted drug delivery system
3. Ba-doped SiO₂/TiO₂ hollow nanospheres for efficient electrorheology fluid

A detailed outline of the study is as follows:

1. Doping of TiO₂ has offered shifting absorption edge from the UV light region to the visible light region [68-73]. Especially, large efforts have been devoted to synthesis of nitrogen-doped TiO₂ nanoparticles (N-TiO₂ NPs) by various synthetic routes [90-93]. Generally, sol-gel method allows simple procedure and practical applications of N-TiO₂ NPs [94]. However, titanium alkoxide as TiO₂ precursor reacts too fast to control the well defined nanostructure in sol-gel method. To manipulate size and shape, templates such as SiO₂ and polystyrene particles have been introduced in the synthetic method [95-97]. Nevertheless, it is still difficult to fabricate uniform N-TiO₂ NPs with diameters under 100 nm using templates mediated sol-gel method [98,99]. Furthermore, most of previous studies have reported high calcination temperature over 400 °C is required for N-TiO₂. It causes

aggregation of N-TiO₂ NPs, which impoverishes photocatalytic efficiency and makes it difficult to apply the N-TiO₂ NPs for coating process, polymer composites, and liquid suspensions. Therefore, technique to fabricate N-TiO₂ NPs with uniform diameter under low temperature treatment to prevent aggregation is imperative for N-TiO₂ NPs [100]. Although much attention has been paid to the study of them, they are still challenging.

In this dissertation, the facile fabrication of uniform SiO₂/N-doped TiO₂ core/shell nanospheres (SNTCN) using SiO₂ template sol-gel method and low temperature treatment is reported. It was conducted with investigation regarding influences of various calcination temperatures and triethylamine on nitrogen doping, visible light absorption and the decompositions of methylene blue under visible light. It allows us to find important factors for N-doped TiO₂ to be used as efficient photocatalyst under visible light irradiation.

2. Recently, camptothecin (CPT) has attracted a great deal of interest as the most promising anticancer drugs [101-106]. However, the clinical application of CPT has been restricted because of its poor water solubility and lactone ring hydrolysis [107,108]. CPT is readily carboxylated, resulting in binding with human serum albumin and losing antitumor activity [109].

Therefore, the encapsulation of CPT is strongly needed to overcome its intrinsic characteristics.

Drug carriers have been widely studied to surmount these clinical inadequacies of CPT and to deliver it into tumor. Advances in the synthesis of nanomaterials provided the key to overcome these problems. The strategy for delivering nanocarriers to tumor was categorized into two ways: a) passive targeting such as nanoparticle (≤ 100 nm) accumulation into tumor by enhanced permeation and retention (EPR) effect and b) active targeting including ligand-receptor interaction between nanoparticle surface and cell membrane receptor [81]. For efficient drug delivery, both strategies could be employed to nanocarriers (e.g., small nanoparticles under 100 nm with monoclonal antibody grafting). Another important factor for the efficient intracellular delivery of nanocarriers is ‘binding site barrier effect’, which occurs when bound nanocarriers to targeted cells block penetration of other non-bound carriers into the tissue [110,111]. To reduce this phenomenon, the nanocarriers attached on the cell surface should be rapidly eliminated by internalization of them. It is known that uniform nanospheres with diameter of *ca.* 50 nm is the most optimum size for cellular uptake of nanoparticles *via* receptor-mediated endocytosis [112-114]. Although the enhancement of anticancer drug efficacy has been well documented, the advancement of the

drug selectivity and toxicity has rarely been carried out. Accordingly, there is necessity for novel anticancer drug loaded immuno-hollow nanoparticle in order to enhance the drug delivery efficacy for cancer cells with low toxicity toward normal cells.

In this dissertation, the fabrication of monodisperse $\text{SiO}_2/\text{TiO}_2$ hollow nanospheres (HNSs) with uniform diameter of *ca.* 50 nm is reported. In addition, HNSs are surface-modified with anti-[human epidermal growth factor receptor 2] monoclonal antibody (herceptin) for targeting human breast cancer SK-BR-3 cells, and encapsulated hydrophobic CPT for targeted drug delivery and low toxicity. Herceptine conjugated HNS shows notable potentials for cancer therapy: uniform size (50 nm), facile antibody conjugation, simple drug loading process, efficient CPT delivery, high selectivity for cancer cells, high uptake ratio into cells, and low toxicity.

3. Electrorheological (ER) fluids are smart materials having the ability to change their rheological property under applied electric field strength [115-117]. The ER fluids are generally composed of polarizable solid particles dispersed in an insulating medium. Under an electric field, the dispersed particles are polarized and attracted to each other to form chain-like or column-like structures along the external electric field direction. The

rheological changes in ER fluid are very fast and reversible. The ER properties are largely dependent to the parameters concerning in electrostatic interaction, including high dielectric constant and dielectric loss which are recognized as the basic factors determining ER performance [118-120]. According to the factors, various materials have been studied and applied for ER fluids with high ER activity [121-127]. Of these materials, Ba-doped TiO₂ have attracted a great deal of interest due to high dielectric constant which is an important factor of efficient ER fluids. A number of studies have reported synthesis of Ba-doped TiO₂ and application to ER fluid. However, relatively little attention has been paid to the control of Ba-doped TiO₂ nanostructures which allow tremendous improvement of ER performance [128-130].

In this dissertation, Ba-doped SiO₂/TiO₂ hollow nanospheres were fabricated from SiO₂/TiO₂ core/shell nanospheres by facile method. The intrinsic characteristics and unique nanostructure of the Ba-doped SiO₂/TiO₂ hollow nanospheres endowed excellent ER performance. Moreover, by facile and mass production of the nanostructure, our suggested ER system was proved to be readily applied for a practical use.

2.1 SiO₂/TiO₂ core/shell nanospheres for photocatalyst under visible light

2.1.1 Fabrication of SiO₂/N-doped TiO₂ core/shell nanospheres

SiO₂/N-doped TiO₂ core/shell nanospheres (SNTCNs) were fabricated in a stepwise manner via sol-gel reaction. A colloidal SiO₂ was prepared via Stöber method for synthesis of SNTCNs [131]. Absolute Ethanol (158 mL), deionized water (2.8 mL), ammonia solution (30 wt%, 7.8 mL), and tetraethyl orthosilicate (TEOS, 5.8 mL) were mixed and stirred at 60 °C for 12 h. After the reaction, 58 mL of acetonitrile was added to as-prepared colloidal SiO₂. Then, the mixed solution containing 7.2 mL of titanium (IV) isopropoxide (TTIP), 36 mL of ethanol, 12 mL of acetonitrile, and various volume of triethylamine (7.2 mL ~ 18 mL) was added to the colloidal SiO₂. At this time, the colloidal SiO₂ was cooled down to 5 °C. TTIP selectively reacts on the surface of SiO₂ nanospheres due to ammonium ions used in Stöber method on their surface. Low temperature synthesis allows uniform TiO₂ shell to form on SiO₂ nanospheres. The mixture was vigorously stirred

for 12 h. Subsequently, the resulting white solution was dried in oven at 100 °C. The final product was obtained by calcination of dried white powder at different temperatures from 150 to 550 °C.

2.1.2 Visible light photocatalytic properties of SiO₂/N-doped TiO₂ core/shell nanospheres

The photocatalytic activities of the SNTCNs were measured using the photodecomposition of methylene blue with concentration at 45 µM. Degussa P-25 was used as a controlled TiO₂ sample. For the photodecomposition, 10 mg of photocatalyst was dispersed in a 20 mL of methylene blue aqueous solution and the solution was stirred in a dark room for 12 h to achieve the absorption equilibrium. Osram XBO 150-W xenon arc lamp installed in a light-condensing lamp housing (PTI, A1010S) was used as a source of visible light irradiation to the solution. A 455 nm cut-off filter was mounted on the lamp housing and the temperature of the solution was maintained at room temperature by water jacket during the overall degradation process. The decomposition of total organic carbon (TOC) was also performed using TOC analyzer (GE, GE Sievers 5310C).

2.2 SiO₂/TiO₂ hollow nanospheres for targeted drug delivery system

2.2.1 Fabrication of SiO₂/TiO₂ hollow nanospheres

In a synthesis of SiO₂/TiO₂ hollow nanospheres (HNSs), colloidal SiO₂ was prepared *via* Stöber method. Tetraethyl orthosilicate (2.9 mL) was added into solution of ethanol (79 mL) and ammonia solution (3.9 mL). The mixture solution was stirred for 12 h at 60 °C. After the synthesis, 29 mL of acetonitrile was added to as-prepared colloidal SiO₂. Then, 3.6 mL of titanium (IV) isopropoxide (TTIP), 18 mL of ethanol, and 6 mL of acetonitrile were mixed. The mixed solution was reacted with the colloidal SiO₂ at 5 °C for 12 h. The resulting products, SiO₂/TiO₂ core/shell nanospheres were precipitated by centrifugation and supernatant was removed. Subsequently, 50 mL of ammonia solution (10 wt%) was treated with the resulting SiO₂/TiO₂ core/shell nanospheres for 24 h. Re-deposition of etched silica occurred under basic condition, resulting HNS comprised of silica and titania. After the reaction, the as-prepared HNSs were isolated from the solution by centrifugation (Mega 17R, Hanil Science and Industrial) and re-dispersed in 50 mL of water. Above-mentioned procedure

was repeated twice to remove ammonia solution.

2.2.2 Antibody conjugation on SiO₂/TiO₂ hollow nanospheres

First of all, 0.5 mL of N-(2-aminoethyl)-3-amino-propyl-trimethoxy-silane was reacted with HNSs (1 mg) in 50 mL of ethanol to introduce amine groups onto HNSs for antibody conjugation. After the silane coupling reaction for 12 h, HNSs were washed several times with deionized water. Subsequently, 10 mg of HNSs, 10 mg of NHS and 50 mg of EDC were added to 2 mL of 0.1 M PBS. Then, 0.2 mL of herceptin was added to the PBS solution to attach herceptin on the surface of HNSs *via* carbodiimide chemistry [132-134]. The reaction was carried out for 4 h at room temperature. Finally, the as-prepared herceptin conjugated HNSs were isolated from the solution by centrifugation (Mega 17R, Hanil Science and Industrial) and re-dispersed in 5 mL of 0.1 M PBS.

2.2.3 Anticancer drug loading into antibody conjugation on SiO₂/TiO₂ hollow nanospheres

For loading the drug molecules into the cavity of HER-HNSs, 50 mg of

HER-HNSs was dispersed in camptothecin (CPT) solution (6 mg of CPT dissolved in 3 mL of DMSO). After the mixture was stirred for 24 h, CPT-loaded HER-HNSs were retrieved using centrifugation and dried in a vacuum oven with an oil pump at 30 °C for 48 h to remove DMSO. The CPT-loaded HER-HNSs were washed twice with 0.1 M PBS to remove CPT adsorbed on surface of HER-HNS.

2.2.4 Drug delivery properties of Antibody conjugation on SiO₂/TiO₂ hollow nanospheres with anticancer drug

SK-BR-3 human breast cancer cells and RAW 264.7 mouse macrophages were used to evaluate drug delivery properties of HER-HNSs. SK-BR-3 and RAW 264.7 were obtained from American Type Culture Collection (ATCC, Manassas, VA, USA) and cultured in 75 T flasks. SK-BR-3 cells were maintained in RPMI-1640 medium with 300 mg L⁻¹ L-glutamine, 10% fetal bovine serum, 1% penicillin/streptomycin solution, 25 mM sodium bicarbonate, and 25 mM 4-(2-hydroxyethyl)-1-piperazineethanesulfonic acid (HEPES). RAW 264.7 cells were cultured in Dulbecco's Modified Eagle Medium (DMEM) with 4 mM L-glutamine, 1 mM sodium pyruvate, 10% fetal bovine serum, and 1%

penicillin/streptomycin solution. These cells were grown in an incubator at 37 °C with 5% CO₂ control and 100% humidity. The media were changed every 2 days or as required.

For live cell observation of apoptosis and necrosis in the cells, they were plated at a density of 3000 cells per well in 8-well Lab-Tek™ II Chambered cover glass (Nunc, Thermo Fisher Scientific, USA) and cultured with 10 µg mL⁻¹ of HNS samples (20 ng mL⁻¹ CPT-equivalent) for 24 h. After treatment, the annexin V (aV)/propidium iodide (PI) double staining were carried out by following supplier's instructions (Vybrant apoptosis assay kit, Molecular Probes, Invitrogen, Grand Island, NY). Live cell fluorescent images were obtained using Delta Vision® RT imaging system (Applied Precision, Issaquah, WA) and Cascade II electronmultiplying charge-coupled device (EMCCD) camera. Using a fluorescence microscope with appropriate filters, the apoptotic and necrotic cells were distinguished. The emission wavelength of aV conjugated Alexa Fluor® 488 and PI is 530 nm and 585 nm, respectively. While early apoptic and necrotic cells have green and red fluorescence respectively, viable cells do not exhibit any fluorescence due to impermeability of dyes. Late apoptotic cells exhibit both green and red fluorescence.

To quantify apoptotic and necrotic cells by flow cytometry, the ratio of

apoptosis and necrosis was evaluated by aV and PI staining followed by flow cytometric measurement of the fluorescence. Cells were incubated in dishes (1×10^5 cells) and $25 \mu\text{g mL}^{-1}$ of HNS samples (50 ng mL^{-1} CPT-equivalent) were added. Cells were suspended in PBS by washing them with 0.1 M PBS. Subsequently, the aV and PI staining was performed as described for live cell observation of apoptosis and necrosis. Flow cytometric analysis was conducted by FACSCalibur™ flow cytometry (Becton Dickinson, USA).

The effect of herceptin on cellular uptake in SK-BR-3 cells was analyzed using transmission electron microscopy (TEM). SK-BR-3 cells were cultured in 4-well Lab-Tek II chamber slides (Nunc, Thermo Fisher Scientific, USA) until 80% confluence. After exposure to $25 \mu\text{g mL}^{-1}$ HNS and HER-HNS for 24 h, cells were fixed with karnovsky's fixative (mixed with 2% paraformaldehyde and 2% glutaraldehyde) at 4 °C for 2 h. The samples were washed with deionized water and the post fixation was conducted using 1% osmium tetroxide at 4 °C for 2 h. The fixed samples were washed twice with 0.1 M PBS, stained with 0.5% uranyl acetate, and then dehydrated using graded ethanol and propylene oxide. Cells were finally embedded in spurr's resin and sectioned by ultramicrotomy. The samples were observed by TEM (JEM1010, JEOL) at 80 kV.

The viabilities of various HNS samples or free-CPT treated cells were measured using Cell-Titer[®] glow luminescent cell viability assay (Promega, Madison, WI). This evaluation is based on amount of adenosine triphosphate (ATP) in metabolically active cells. The luminescence is observed when the beetle luciferin is converted into oxyluciferin by a recombinant luciferase in the presence of ATP. It means that the luminescence intensity is proportional to presence of ATP in cells. For the assay, cells were plated (1.5×10^4 cells mL^{-1}) in black opaque 96-well plates and treated with 10, 25, and 100 $\mu\text{g mL}^{-1}$ of the HNS samples (20, 50, and 200 ng mL^{-1} CPT-equivalent) for 24 h. After incubation, supernatant was removed and carried out according to manufacturer's instructions. Cell viabilities were determined by Victor³ Multilabel Readers (Perkin Elmer, Boston, MA, USA).

2.3 Ba-doped SiO₂/TiO₂ hollow nanospheres for efficient electrorheological fluid

2.3.1 Fabrication of Ba-doped SiO₂/TiO₂ hollow nanospheres from SiO₂/TiO₂ core/shell nanospheres

Synthesis of colloidal SiO₂ *via* Stöber method was first step in fabrication of Ba-doped SiO₂/TiO₂ hollow nanospheres (Ba-HNSs). Tetraethyl orthosilicate (17.4 mL) was added into solution of ethanol (475 mL) and ammonia solution (23.4 mL). The mixture solution was stirred for 12 h at 60 °C. After the synthesis, 175 mL of acetonitrile was added to as-prepared colloidal SiO₂. Then, 21.6 mL of titanium (IV) isopropoxide (TTIP), 108 mL of ethanol, and 36 mL of acetonitrile were mixed. The mixed solution was reacted with the colloidal SiO₂ at 5 °C for 12 h. The resulting products, SiO₂/TiO₂ core/shell nanospheres were precipitated by centrifugation and supernatant was removed. The SiO₂/TiO₂ core/shell nanospheres were re-dispersed in Ba(OH)₂ aqueous solution of 500 mL (0.1 M) and treated with sonication for 3 h. Re-deposition of etched silica occurred under basic condition, resulting Ba-HNSs. After the reaction, the Ba-HNSs were isolated from the solution by centrifugation (Mega 17R,

Hanil Science and Industrial) and re-dispersed in deionized water. It was repeated for washing excessive $\text{Ba}(\text{OH})_2$ on surface of Ba-HNSs. Finally, the Ba-HNSs were dried in a vacuum oven at 60 °C.

2.3.2 Fabrication of ER fluid based on Ba-doped $\text{SiO}_2/\text{TiO}_2$ hollow nanospheres

Prepared Ba-HNSs were dried in a vacuum oven at 60 °C for 24 h to remove moisture. Then, the Ba-HNSs were dispersed in silicon oil (poly(methylphenylsiloxane), viscosity = 100 cSt). Concentration of ER fluid was 15 vol% and no additives were added to the ER fluid. For uniform dispersion of Ba-HNSs in the silicon oil, the ER fluid was milled for 30 min. ER fluid of HNS and commercial BaTiO_3 nanopowder (Sigma-Aldrich) was prepared respectively by the same method to compare ER properties of the Ba-HNS based ER fluid with those of HNS and commercial BaTiO_3 nanopowder based ER fluid.

2.3.3 Electrorheological properties of ER fluid based on Ba-doped $\text{SiO}_2/\text{TiO}_2$ hollow nanospheres

The ER properties of the Ba-HNS and commercial BaTiO_3 nanopowder based ER fluids were examined respectively via rheometer (AR

2000 Advanced Rheometer, TA Instruments) with a concentric cylinder conical geometry of 15 mm cup radius, a high-voltage generator (Trek 677B), and a temperature controller. To start a run, an ER fluid is placed between cup and rotor with a gap distance of 1.00 mm, and DC voltage is applied to the plate. An electric field was applied for 3 min to obtain an equilibrium chain-like or columnar structure before applying shear. All measurements were made at a room temperature, and the shear rate was varied from 0.1 to 1000 s^{-1} .

2.4 Instrumental

Transmission electron microscopy (TEM) images were taken with JEOL EM-2000 EX II microscope or Carl Zeiss LIBRA 120 microscope. For TEM observation, the nanomaterials were diluted in water or ethanol and the diluted solution was deposited on a copper grid coated with carbon film. The scanning transmission electron microscopy images and energy-dispersive X-ray spectroscopy (EDX) analysis data were obtained using a JEOL JSM-6700F.

The spectra of X-ray photoelectron spectroscopy (XPS) were obtained by Sigma probe (Thermo). The nitrogen adsorption-desorption isotherms were measured on a ASAP 2010 (Micrometrics Co.) at 77 K. The isotherms were used to calculate the Brunauer-Emmett-Teller (BET) surface area, total pore volume, and pore size distribution. The pore size distribution was obtained by Barrett-Joyner-Halenda (BJH) method. Powder X-ray diffraction (XRD) measurements were carried out using an M18XHF-SRA (Mac Science) diffractometer equipped with a CuK α radiation source ($\lambda = 1.5406$ Å) at 40 kV and 300 mA (12 kW). The X-ray diffraction peaks were collected between 20° and 80° with a scan rate of 4° min⁻¹. The UV-visible diffuse reflectance spectra (DRS) were recorded by a PerkinElmer Lambda

35 spectrometer and diffuse reflectance spectroscopy accessory. The change in optical density of samples was measured using S-3100 (SCINCO). The decomposition of total organic carbon (TOC) was also performed using TOC analyzer (GE, GE Sievers 5310C). The zeta potential and particle size distribution of samples were determined using a DLS-7000 (Otsuka Electronics).

Chapter 3 Results and Discussion

3.1 SiO₂/TiO₂ core/shell nanospheres for photocatalyst under visible light

3.1.1 Fabrication of SiO₂/N-doped TiO₂ core/shell nanospheres

SiO₂/N-doped TiO₂ core/shell nanospheres (SNTCNs) were fabricated in a stepwise manner via sol-gel reaction. The overall synthetic procedure for the SNTCNs is illustrated in **Figure 10**. First, SiO₂ nanospheres with an average diameter of approximately 30 nm were synthesized by Stöber method. Then, N-doped TiO₂ layer was formed on the surface of SiO₂ nanospheres by simultaneous hydrolysis of TTIP and triethylamine at ammonia ions on surface of SiO₂ nanosphere. Finally, SNTCNs were obtained after calcination, from 150 °C to 550 °C. The prepared SNTCNs were observed by transmission electron microscope (TEM). **Figure 11** and **12** shows TEM images of SiO₂ nanospheres and SNTCNs with the calcination at 250 °C (SNTCN250), respectively. An average diameter of the SiO₂ cores was *ca.* 30 nm and SNTCNs with an average diameter of *ca.* 40 nm have uniformity after encapsulation of N-doped TiO₂ layer and

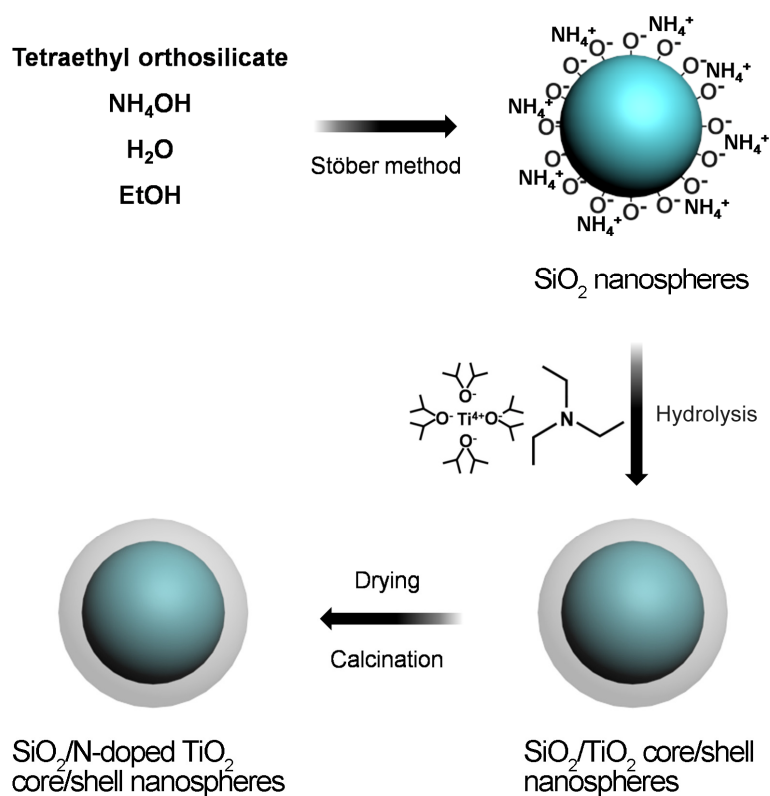


Figure 10. A schematic diagram of the fabrication of $\text{SiO}_2/\text{N-doped TiO}_2$ core/shell nanospheres.

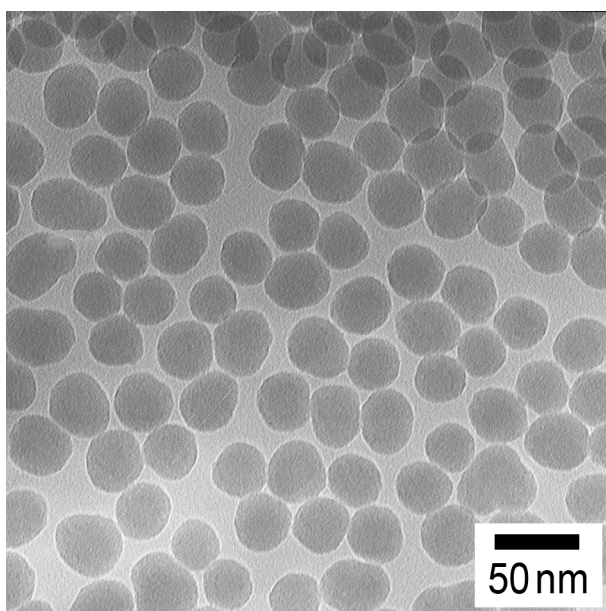


Figure 11. TEM image of SiO₂ nanospheres with an average diameter of 30 nm.

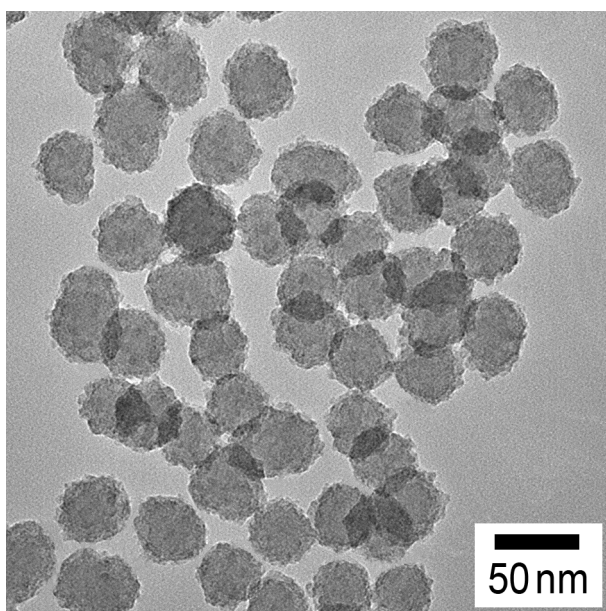


Figure 12. TEM image of SNTCNs calcined at 250 °C with diameter of 40 nm.

calcination at 250 °C. These TEM images clearly prove difference of diameter and surface morphology between SiO₂ nanospheres and SNTCNs. Size distributions of SiO₂ nanospheres and SNTCNs also display diameter of the nanospheres increases after formation of TiO₂ shell (**Figure 13**). Considering these data, the TiO₂ shell was successfully formed onto surface of SiO₂ nanospheres.

For validation of nitrogen doping into TiO₂, X-ray photoelectron spectroscopy (XPS) analysis was performed. **Figure 14** presents full-scale XPS spectra of SNTCNs with calcination at different temperatures from 150 °C to 550 °C. N-doped TiO₂ shells of these SNTCNs were fabricated by co-hydrolysis of TTIP and triethylamine in the ratio of 1:2. All spectra show typical characteristics of TiO₂ and nitrogen. Especially, N 1s binding energy peak around 400 eV implies that nitrogen was incorporated into TiO₂ lattice [135]. The enlarged N 1s regions of the XPS spectra were also obtained for more detail analysis of N-doping (**Figure 15**). Two peaks were detected at 399.5 and 401.5 eV in all the XPS spectra of SNTCNs. The former peak is related to O-Ti-N or NO in a metal lattice, and the latter peak is related to N₂ or N-H absorbed on the TiO₂ surface [136]. Judging from these data, the peak at 399.5 eV represents nitrogen incorporated into the TiO₂ lattice, and the peak at 401.5 eV indicates triethylamine absorbed on the TiO₂ surface.

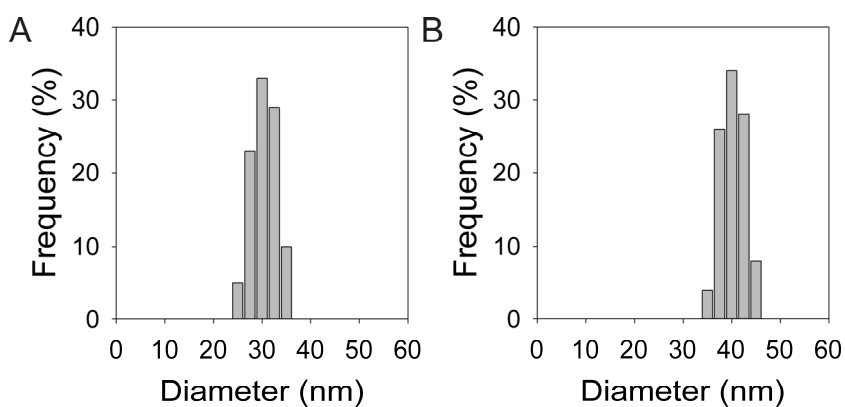


Figure 13. Size distributions of (A) SiO₂ nanospheres and (B) SNTCN250.

It was prepared by measuring the diameters of hundred SiO₂ nanospheres and SNTCNs directly from TEM images.

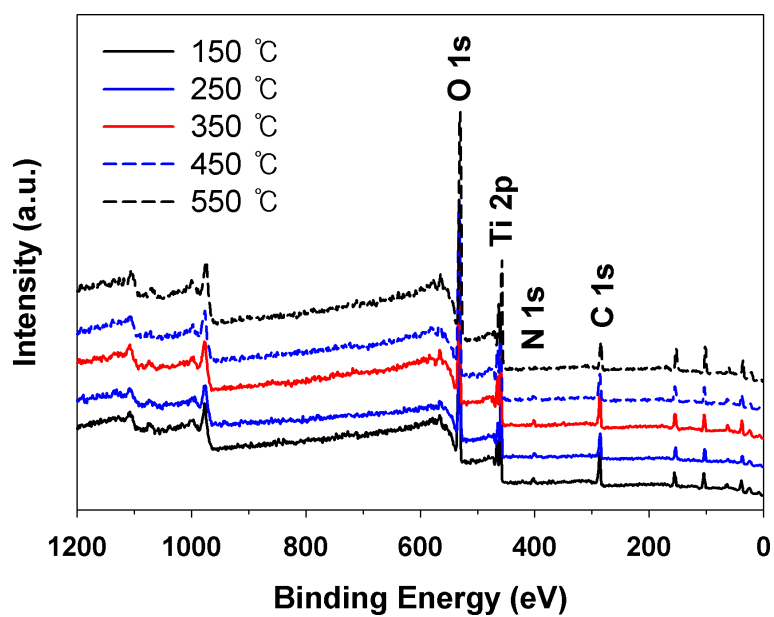


Figure 14. Full-scale X-ray photoelectron spectroscopy spectra of SNTCNs calcined at different temperatures (150, 250, 350, 450, and 550 °C).

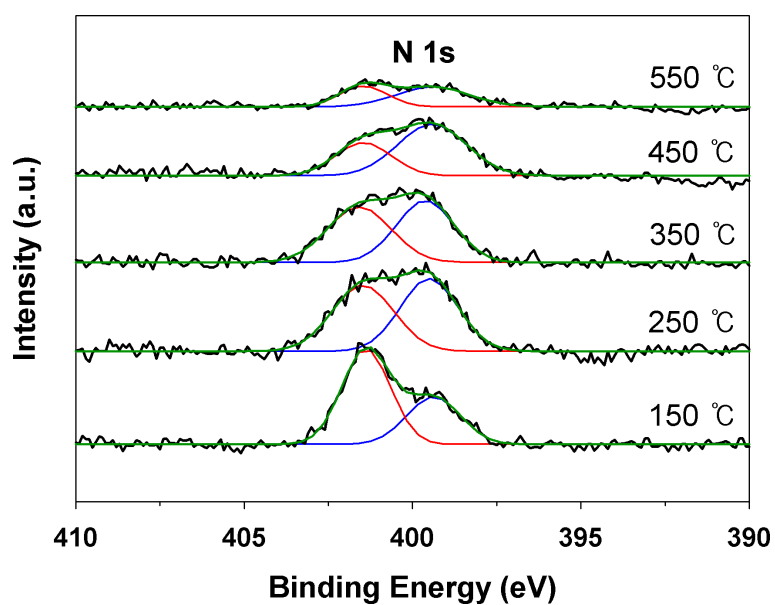


Figure 15. Enlarged N 1s regions of the SNTCN calcined at different temperatures (150, 250, 350, 450, and 550 °C).

The area of N 1s peaks vary with increasing the calcination temperature of SNTCNs, which means the amount of N-doping in TiO₂ is different as calcination temperature of SNTCNs changes. Total amount of nitrogen decreased above 250 °C due to desorption of triethylamine on the TiO₂ and replacement of doped nitrogen by oxygen at elevated temperature [137]. Although total nitrogen contents of SNTCNs at 150 and 250 °C are almost equal, the ratio of doped nitrogen to absorbed nitrogen is higher in the latter. These data denote that high calcination temperature increases the population of incorporating nitrogen into TiO₂ and replacing doped nitrogen with oxygen increase simultaneously. As a result, the highest nitrogen doping of SNTCN (5%) was obtained at 250 C° (**Table 2**). Total nitrogen (absorbed nitrogen and doped nitrogen), doped nitrogen, titanium, and oxygen content of N-doped TiO₂ shell were calculated by area of N 1s, Ti 2p, and O 1s binding energy peaks.

Effect of the amount of nitrogen dopant on nitrogen doping level into TiO₂ lattice was also investigated. The volume ratio of triethylamine to TTIP was changed from 1:1 to 2.5:1 and all SNTCNs exhibited characteristic XPS spectra of N-doped TiO₂ (**Figure 16**). When the ratio of triethylamine to TTIP increased, nitrogen doping level into TiO₂ lattice increased. However the ratio of triethylamine to TTIP did not affect nitrogen doping level

significantly compared to calcination temperature (**Figure 17**). The nitrogen doping was saturated when the ratio of triethylamine/TTIP was over 2.

Table 2. Elemental contents of N-doped TiO₂ shell measured by analysis of XPS binding energy peaks. Total N (1s) includes doped nitrogen and absorbed nitrogen content.

Calcination temperature /°C	O (1s) /atomic %	Ti (2p) /atomic %	Total N (1s) /atomic %	Doped-N (1s) /atomic %
150	62	29	9	3
250	62	29	9	5
350	63	29	8	4
450	66	29	5	3
550	69	29	2	1

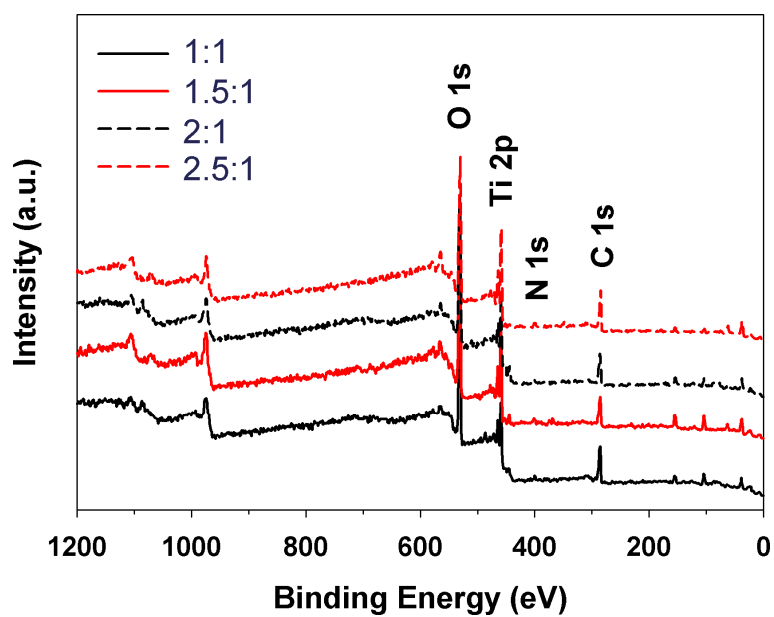


Figure 16. Full-scale X-ray photoelectron spectroscopy spectra of SNTCNs calcined at 250 °C with various volume ratio of triethylamine to TTIP.

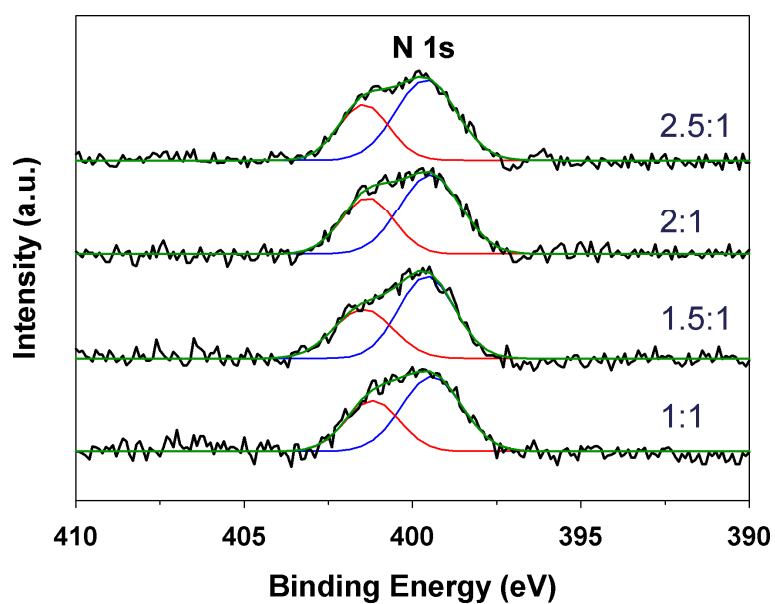


Figure 17. Enlarged N 1s regions of SNTCNs calcined at 250 °C with various volume ratio of triethylamine to TTIP.

3.1.2 Visible light photocatalytic properties of SiO₂/N-doped TiO₂ core/shell nanospheres

The optical absorptions of SNTCNs were characterized by UV-visible diffuse reflectance spectroscopy (DRS). **Figure 18** presents the spectra for SNTCNs with various calcination temperatures. All SNTCNs have the enhanced absorption over the visible light region ($\lambda > 400$ nm) in comparison with commercial TiO₂ nanoparticle, Degussa P-25. It was selected as control material, which is widely used for photocatalyst. The optical absorption in the visible light region grew upon increasing the calcination temperature until 250 °C and decreased over the calcination temperature of 250 °C. SNTCN250 had the most enhanced absorption. The optical absorption behavior in the visible light region was similar to the XPS result. These results imply that the visible light absorption for SNTCN strongly depends on the amount of the doped nitrogen. As expected, the visible light absorption increased with increasing the amount of doped nitrogen. The saturation of visible light absorption occurred when the ratio of triethylamine to TTIP was 2:1 and the ratio had small effect on nitrogen doping level in comparison to calcination temperature (**Figure 19**). It is also in accord with the XPS result.

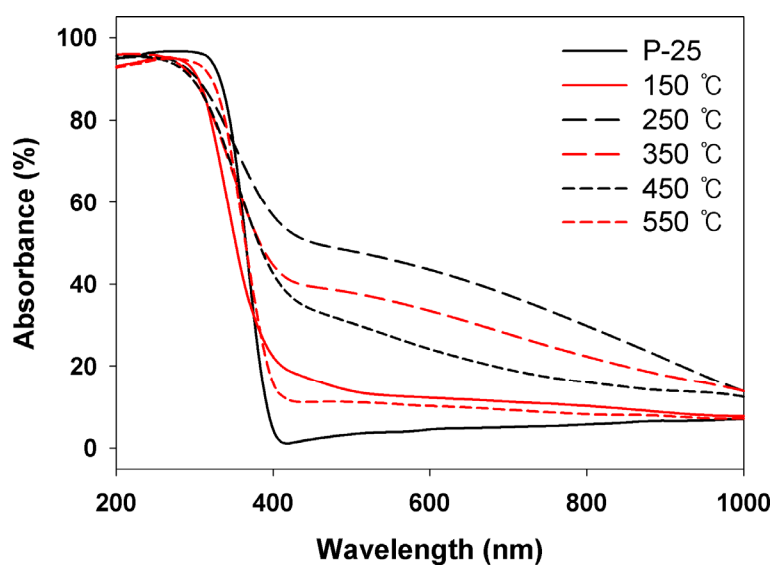


Figure 18. Uv-vis diffuse reflectance spectroscopy spectra for P-25 and SNTCNs calcined at different temperatures.

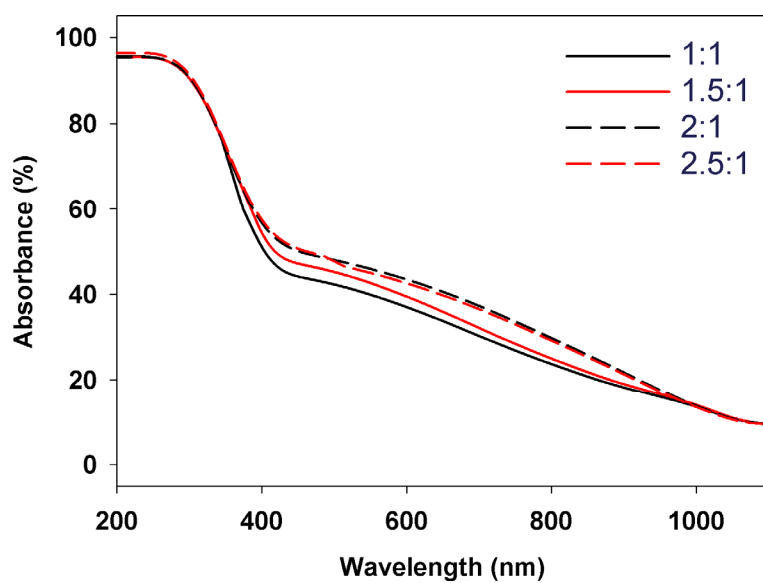


Figure 19. Uv-vis diffuse reflectance spectroscopy spectra for NSTCS calcined at 250 °C with various volume ratio of triethylamine to TTIP.

The photocatalyzed bleaching of dye molecules dissolved in a test solution was conducted as a photocatalytic activity test system which was widely used in many cases [138,139]. To examine the activity in aqueous solutions, methylene blue was selected as probe molecule (**Figure 20**). The change in optical density of methylene blue was measured by UV-visible spectroscopy as a function of visible light irradiation time. The first-order rate constant k was also calculated by fitting the experimental data. With the exception of the SNTCN150, all SNTCN showed higher photocatalytic activity in comparison with P-25. Photocatalytic activity of SNTCN increased with elevation of calcination temperature, and gradually decreased when the temperature was over 250 °C (**Figure 21**). SNTCN250 exhibited the best performance as a photocatalyst. The k of SNTCN250 was 0.362 h⁻¹, and it was 14 times larger than that of P-25, 0.025 h⁻¹. Judging from XPS spectra, DRS spectra, and photodecomposition of methylene blue, the nitrogen doping level and the visible light absorption play a key factor in enhancing photocatalytic efficiency under visible light irradiation. The photocatalytic activities of SNTCNs with various volume ratio of triethylamine to TTIP were also investigated (**Figure 22**). According to expectation from the XPS and DRS spectra, the photocatalytic activities of SNTCNs were not significantly affected by the volume ratio of triethylamine

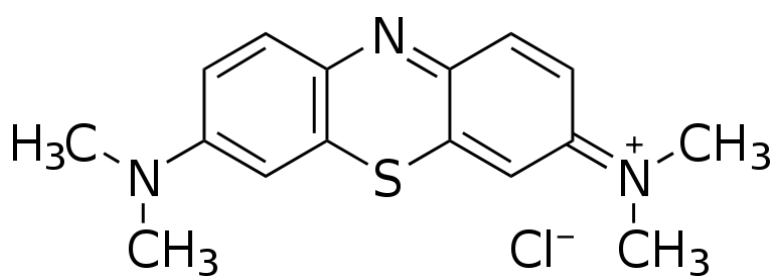


Figure 20. Structure of methylene blue.

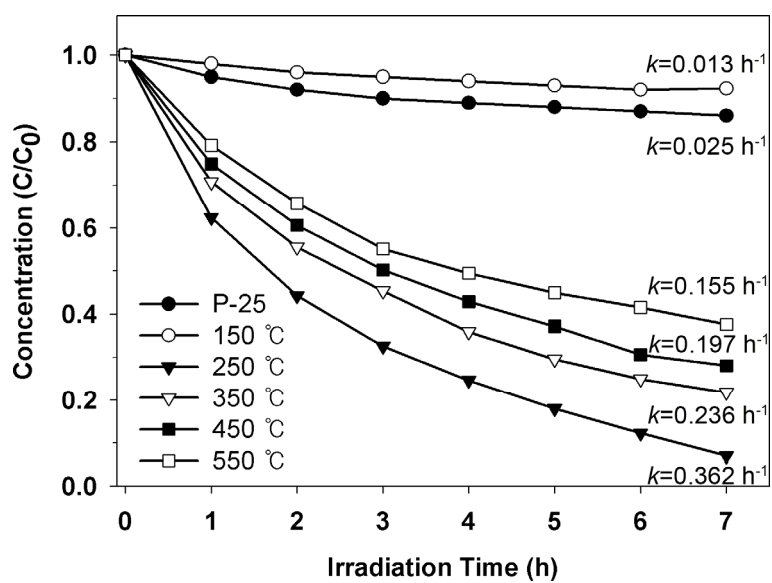


Figure 21. Photodecomposition of methylene blue by P-25 and SNTCNs calcined at different temperatures.

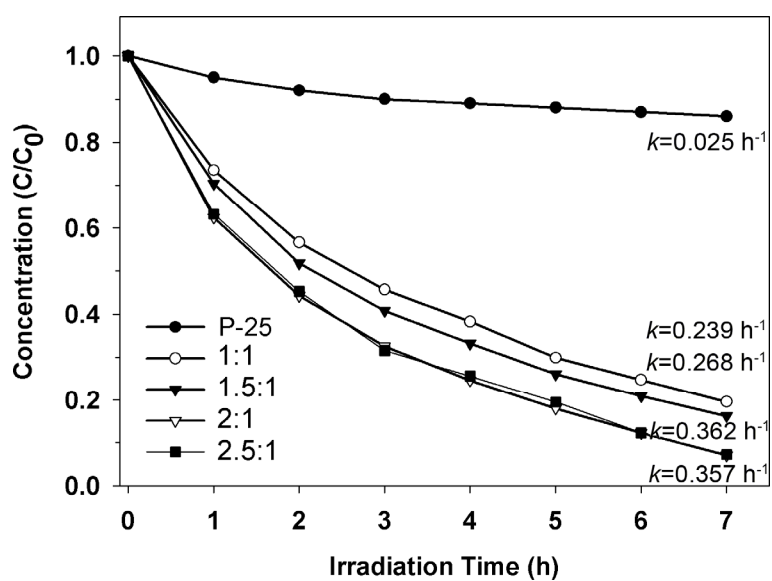


Figure 22. Photodecomposition of methylene blue by P-25 and SNTCNs calcined at 250 °C with various volume ratio of triethylamine to TTIP.

to TTIP. However, against expectation, SNTCN150 showed lower photocatalytic efficiency than SNTCN550 although SNTCN150 had higher nitrogen doping level than SNTCN550. It was originated from low crystalline content of SNTCN150 in contrast with SNTCN550 (**Figure 23**), because the calcination temperature of 150 °C was not enough to form nanocrystals. SNTCN250, 350, and 450 also have no significant XRD patterns of anatase crystallinity. However it was reported in previous study that TiO₂ particles calcined over 200 °C have mixtures of crystalline and amorphous particles [137]. Besides the nitrogen doping and the crystallinity, surface area of SNTCN is another important factor for photocatalytic activity. Surface area of SNTCN250 was 6 and 1.6 times higher than P-25 and SNTCN550 respectively although they have similar diameter (**Table 3**). This difference is caused by the aggregation of nanoparticles. **Figure 24** shows irregular and agglomerated TiO₂ nanoparticles of P-25. SNTCN550 also has aggregation of nanoparticles caused by high calcination temperature (**Figure 25**). It is noteworthy that the surface areas of SNTCN calcined below 250 °C were almost unchanged. This result means that SNTCN250 has the highest photocatalytic activity without aggregation after calcination.

Furthermore, TOC analysis could demonstrate that mineralization was connected with this photocatalytic decomposition of dye. The general dye

decomposition was comprised of the reaction from dye molecule to uncolored intermediates and the reaction from uncolored intermediates to mineralized products [140,141]. Between the two reactions, the later could be significant process because it is related to increased biodegradability and decreased toxicity. Under visible irradiation for 7 h, SNTCN150, SNTCN250, SNTCN350, SNTCN450, SNTCN550 and P-25 exhibited the TOC loss value of 1, 62, 41, 35, 29, and 3 % over the dye solution. It showed that mineralization step was involved in decomposition of methylene blue.

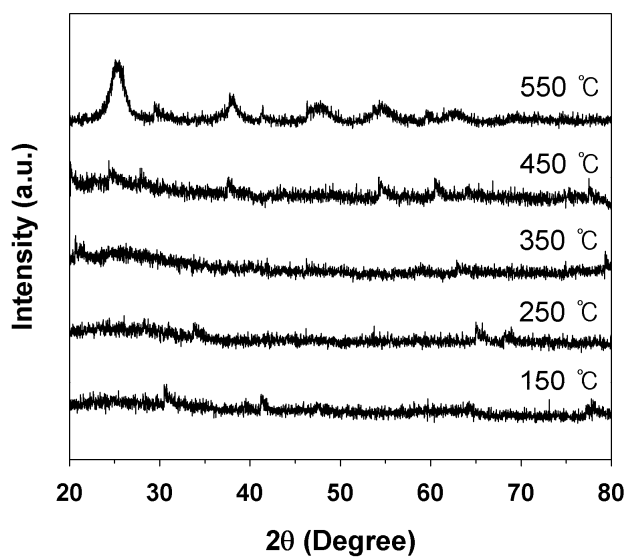


Figure 23. XRD patterns of SNTCNs with different calcination temperatures.

Table 3. BET surface area of Degussa P-25 and NSTCS calcined at different temperature.

Samples	BET Surface Area ^a /m ² g ⁻¹
N150	303
N250	302
N350	270
N450	232
N550	184
Degussa P-25	51

^a Calculated by Brunauer-Emmett-Teller method

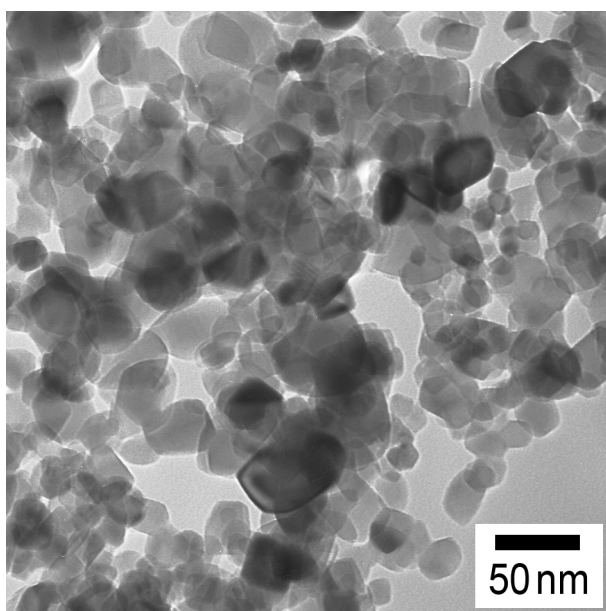


Figure 24. TEM images of Degussa P-25.

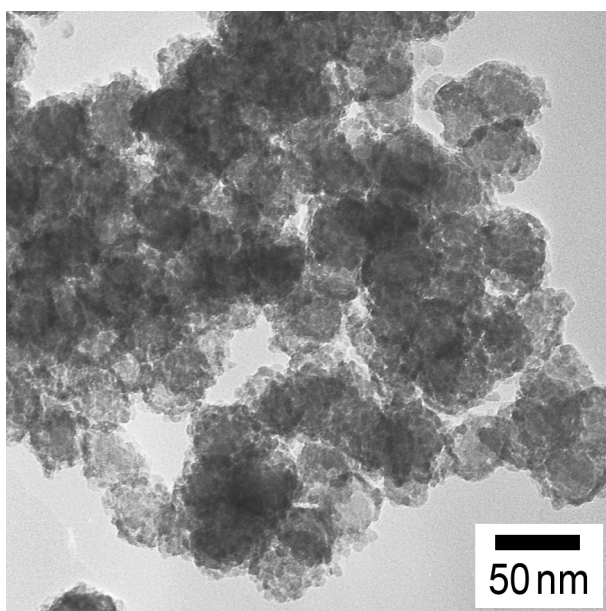


Figure 25. TEM images of SNTCN550.

3.2 SiO₂/TiO₂ hollow nanospheres for targeted drug delivery system

3.2.1 Fabrication of SiO₂/TiO₂ hollow nanospheres

Silica/titania hollow nanospheres (HNSs) were fabricated *via* the dissolution and re-deposition method of silica which was reported in previous study [142]. The overall experimental procedure of antibody conjugated HNSs fabrication for drug delivery is schematically illustrated in **Figure 26**. HNSs were evolved from SiO₂/TiO₂ core/shell nanospheres of *ca.* 45 nm in diameter which was obtained from introduction of TiO₂ layer on the silica nanospheres. In ammonia aqueous solution, the SiO₂/TiO₂ core/shell nanospheres were transformed into HNSs *via* the reversible process of dissolution and re-deposition of SiO₂. It is considered that SiO₂ in basic condition is dissolved by weakening siloxane bonds and coordinating hydroxide ion to Si atoms [143]. In contrast, TiO₂ is not etched due to its chemical inertness. **Figure 27** represents transmission electron microscope (TEM) images of HNSs at low and high magnification, which shows HNSs have large cavity suitable for drug storage. Scanning electron microscope (SEM) image exhibits monodisperse of HNSs with an average diameter of

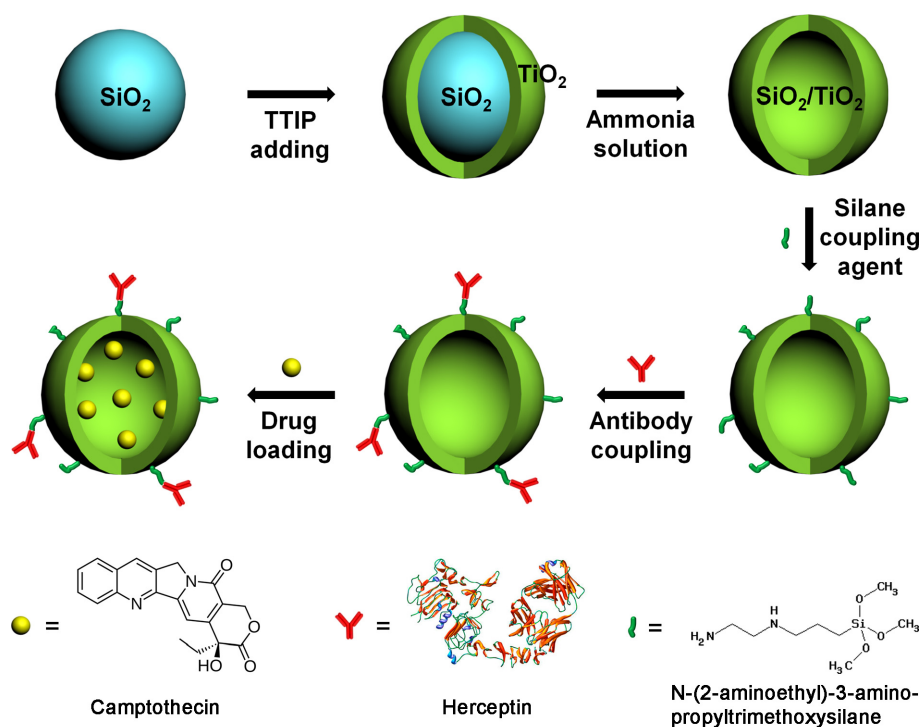


Figure 26. A schematic illustration of fabrication of antibody conjugated silica/titania hollow nanospheres (HNS) containing CPT.

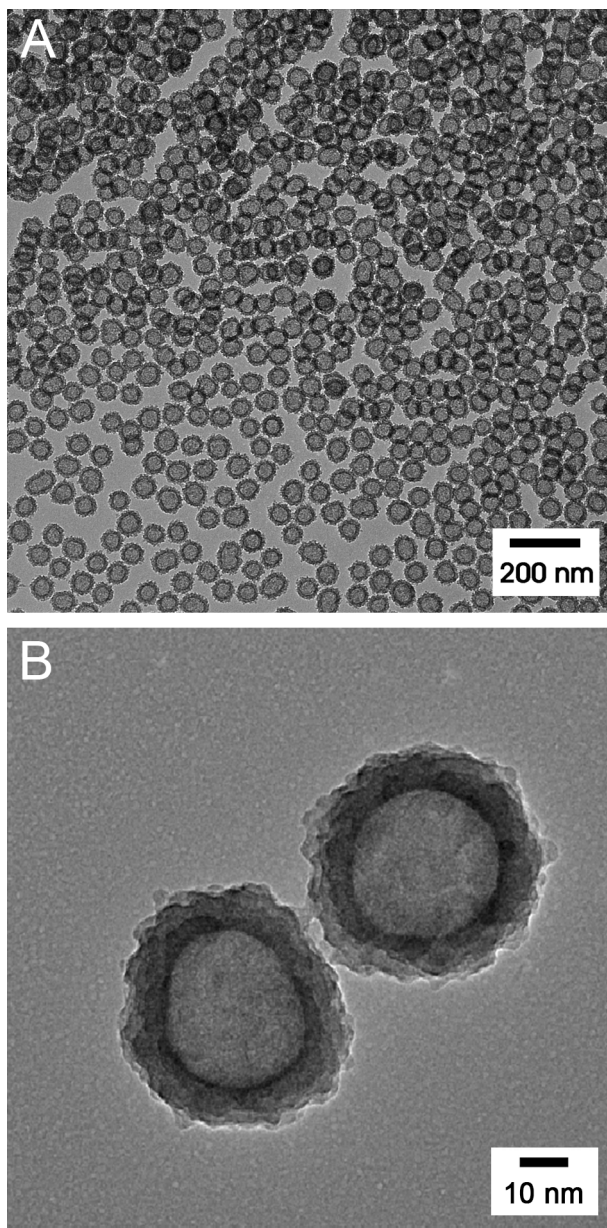


Figure 27. TEM images of $\text{SiO}_2/\text{TiO}_2$ hollow nanospheres (HNSs) with an average diameter of 50 nm at (A) low and (B) high magnification.

ca. 50 nm (**Figure 28**). Energy disperse X-ray spectroscopy (EDX) results indicated that the atomic ratio between Si and Ti was altered from 60:40 (core/shell nanosphere) to 52:48 (HNSs) due to silica etching and re-deposition process (**Figure 29**).

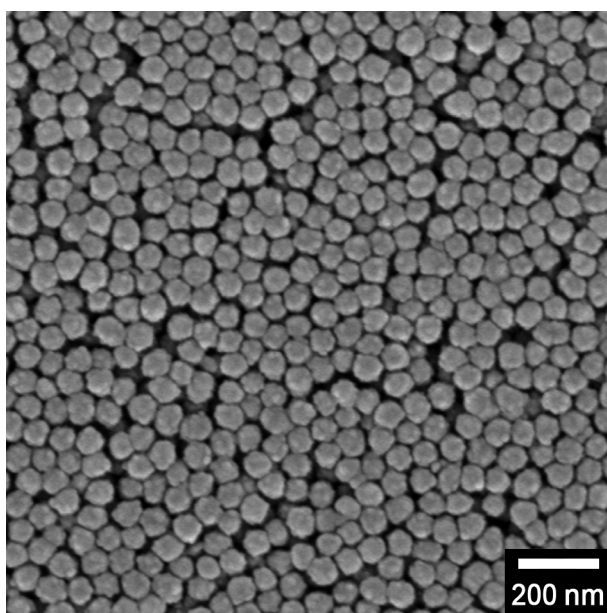


Figure 28. SEM image of HNSs with an average diameter of 50 nm.

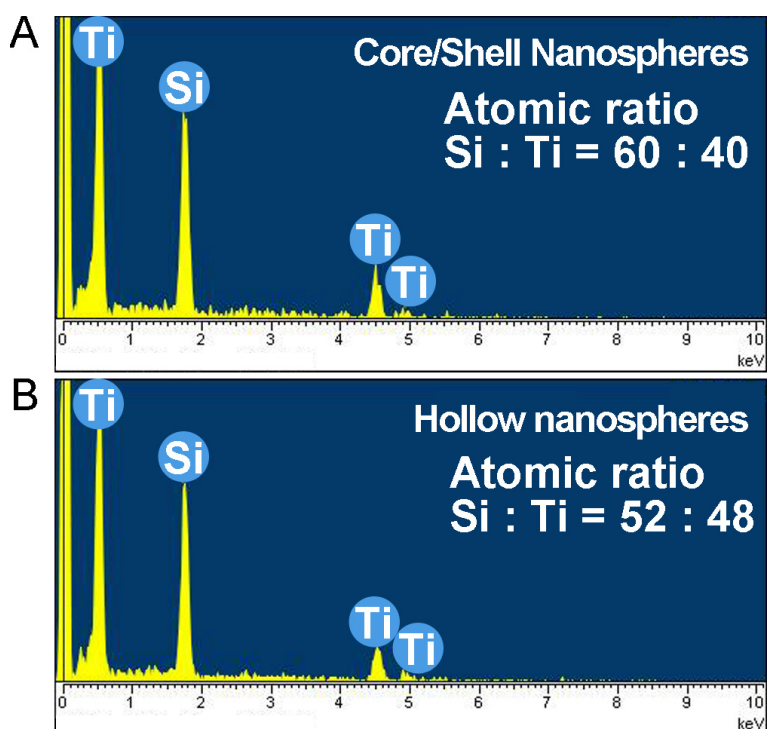


Figure 29. Energy dispersive X-ray spectroscopy (EDX) spectra of (A) the $\text{SiO}_2/\text{TiO}_2$ core/shell nanospheres and (B) the hollow nanospheres.

3.2.2 Antibody conjugation on SiO₂/TiO₂ hollow nanospheres

Herceptin as a breast cancer cell targeting ligand was attached to the amine-functionalized HNSs *via* conventional N-ethyl-N'-(3-dimethylamino-propyl) carbodiimide hydrochloride (EDC)/N-hydroxysuccinimide (NHS) activation (HER-HNSs). Electrophoretic light scattering spectroscopy (ELS) data revealed an average diameter of 49.8 nm and narrow size distribution of HNSs. After herceptin modification, the hydrodynamic diameter of HNSs increased from 49.8 nm to 59.7 nm (**Figure 30**), and the zeta potential varied from -53.5 mV to -37.0 mV. Considering these facts, the monoclonal antibody herceptin was fruitfully grafted onto surface of the HNS.

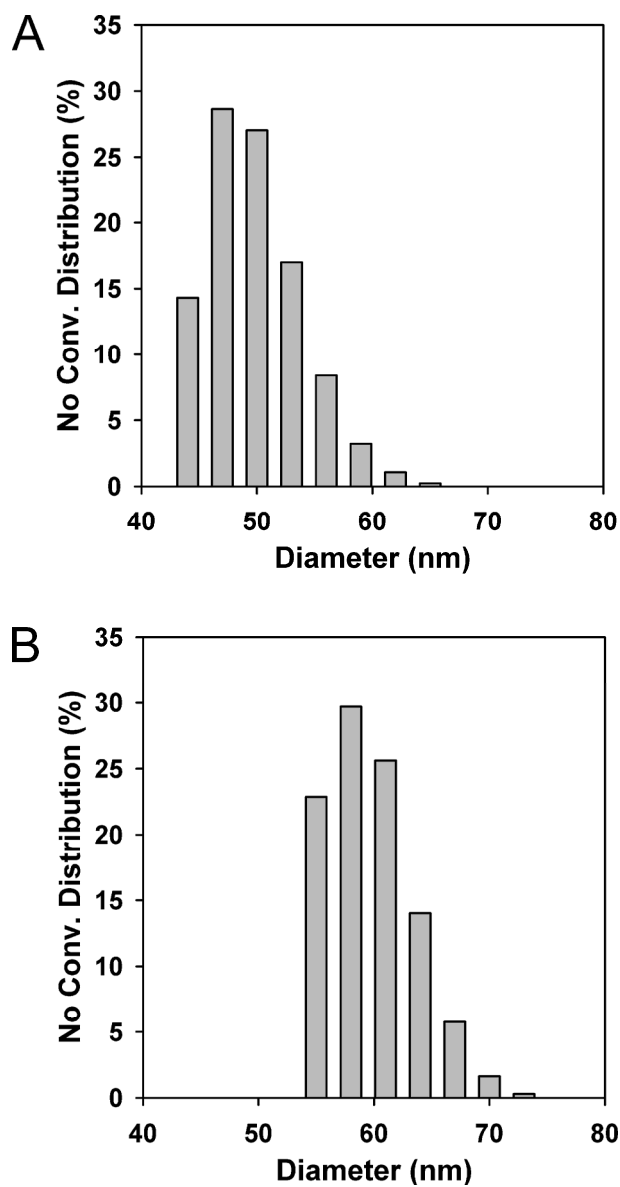


Figure 30. Size distributions of (A) HNSs and (B) herceptin conjugated HNSs (HER-HNSs) measured by electrophoretic light scattering spectroscopy (ELS).

3.2.3 Anticancer drug loading into antibody conjugation on SiO₂/TiO₂ hollow nanospheres

Analyses for the nitrogen adsorption isotherm and the pore size distribution curve of HNSs were conducted to clarify textural properties of HNSs. A type IV curve of hysteresis adsorption-desorption isotherm was observed, indicating mesoporous materials (**Figure 31**). The pore volume and Brunauer-Emmett-Teller (BET) surface area are 1.07 cm³ g⁻¹ and 246 m² g⁻¹ respectively. The cavity size of HNSs was found be centered around 2.5 nm and 29.2 nm by measuring the Barrett-Joyner-Halenda (BJH) pore distribution (**Figure 32**). Considering TEM image and pore distribution of HNSs, HNS has cavity with an average diameter of 29.2 nm and porous wall with pore of 2.5 nm. Judging from size of most anticancer drugs' molecule, the textural properties of HNSs offer potential capability to load guest molecules into the cavity for the application of drug delivery.

In vitro release profile of herceptin conjugated HNSs for CPT was measured using UV/Vis spectroscopy (**Figure 33**). CPT of *ca.* 20 µg was loaded into HER-HNS of 10 mg (57.412 nmol). Remarkably, although diameter of HER-HNS is only 1/3 of mesoporous silica nanoparticle (130 nm in diameter), the loading capacity is about 3 times higher than the

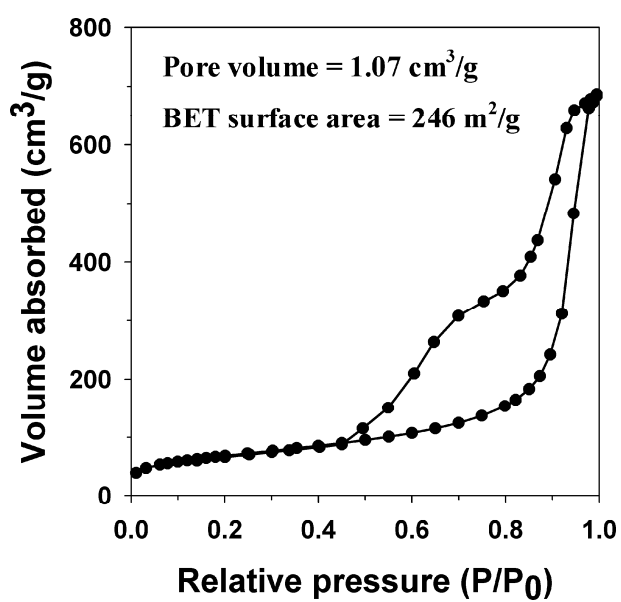


Figure 31. Nitrogen adsorption isotherm of the HNSs.

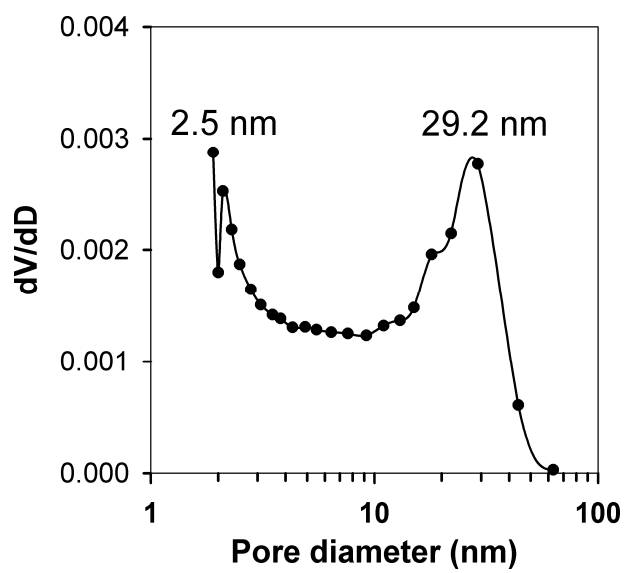


Figure 32. Pore size distribution of HNSs.

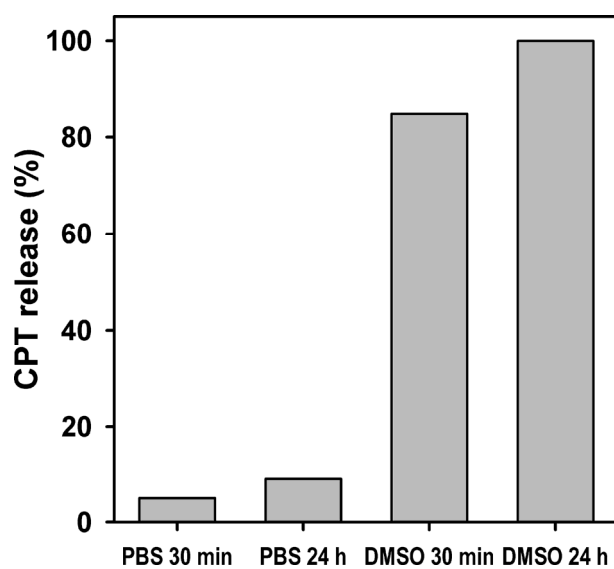


Figure 33. Time-dependent release profile of CPT from HNS into 0.1 M phosphate buffer solution (PBS) and DMSO.

reported loading capacity (16 nmol of CPT per 10 mg of the mesoporous silica nanoparticles) using DMSO as the loading solvent [144]. Release profile of HNSs for CPT was dependent with solvent. In 0.1 M phosphate buffer solution (PBS), HER-HNS released only *ca.* 5% and 9% of CPT for 30 min and 24 h due to the hydrophobicity of CPT, respectively. However, HER-HNS in DMSO released *ca.* 86% and 100% of CPT for 30 min and 24 h, respectively. This result demonstrated that HER-HNS could effectively deliver CPT into cancer cells with minimal leakage [144]. Considering these data, HER-HNSs with a large hollow cavity are very suitable for using *in vitro* CPT delivery carrier.

3.2.4 Drug delivery properties of Antibody conjugation on SiO₂/TiO₂ hollow nanospheres with anticancer drug

To investigate HNSs for an anticancer drug carrier, the effect of HNSs to SK-BR-3 human breast cancer cells was examined. **Figure 34** represents live cell images of SK-BR-3 treated with HNSs for 24 h. Cells were stained with annexin V conjugated Alexa 488 (aV; green) and propidium iodide (PI; red) for visualizing apoptosis and necrosis, respectively. Unstained cells categorized as viable cells, and green/red fluorescent labels were classified as early apoptotic/necrotic cells. Dual stained cells were defined as late apoptotic cells. In case of free-CPT, SK-BR-3 demonstrated no staining with aV and PI (**Figure 34 left column**). However, when the cells were incubated with CPT and HNS-CPT, some apoptotic cells appeared (**Figure 34 right column**). In particular, SK-BR-3 treated with HER-HNS-CPT broke apart into large amount of small apoptotic bodies, which revealed significant cell death.

Efficient anticancer therapy *via* HER-HNS-CPT was proved in live cell fluorescent images for 30 min, 2 h, and 12 h (**Figure 35**). For 2 h incubation, the cells with HER-HNS-CPT represented late apoptosis compared with healthy cells treated with HNS-CPT. Furthermore, HER-HNS-CPT treated

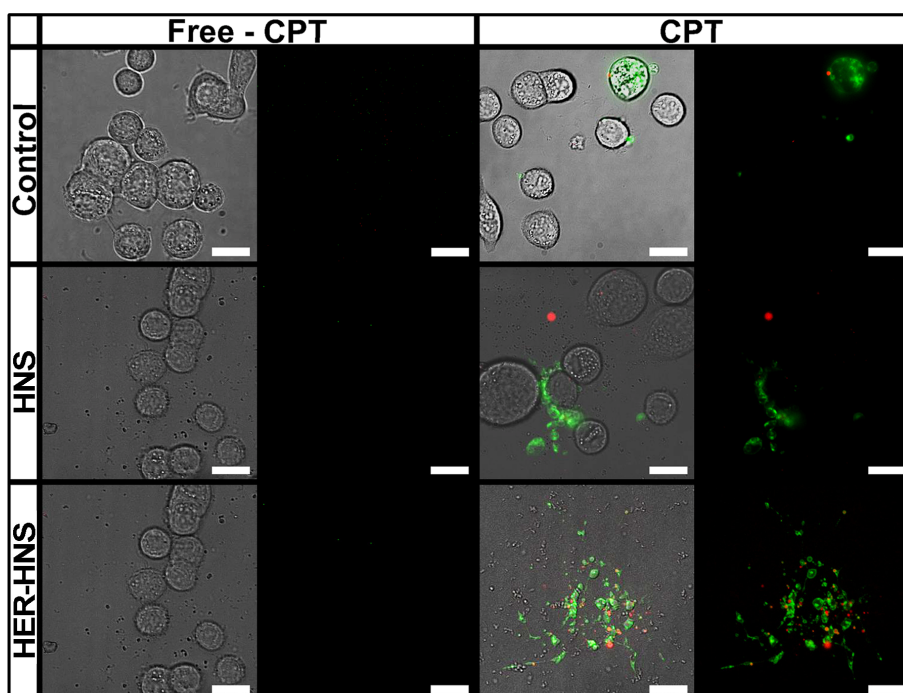


Figure 34. Live cell fluorescent images of SK-BR-3 human breast cancer cells incubated with $10 \mu\text{g mL}^{-1}$ of HNS, HER-HNS, HNS-CPT, HER-HNS-CPT or the same concentration of CPT in PBS (20 ng mL^{-1}) for 24 h. Cells were stained with annexin V conjugated Alexa 488 (aV; green) and propidium iodide (PI; red) for visualizing apoptosis and necrosis in cells. DIC images were obtained at the same time, corresponding to the fluorescent images (Scale bars: $20 \mu\text{m}$).

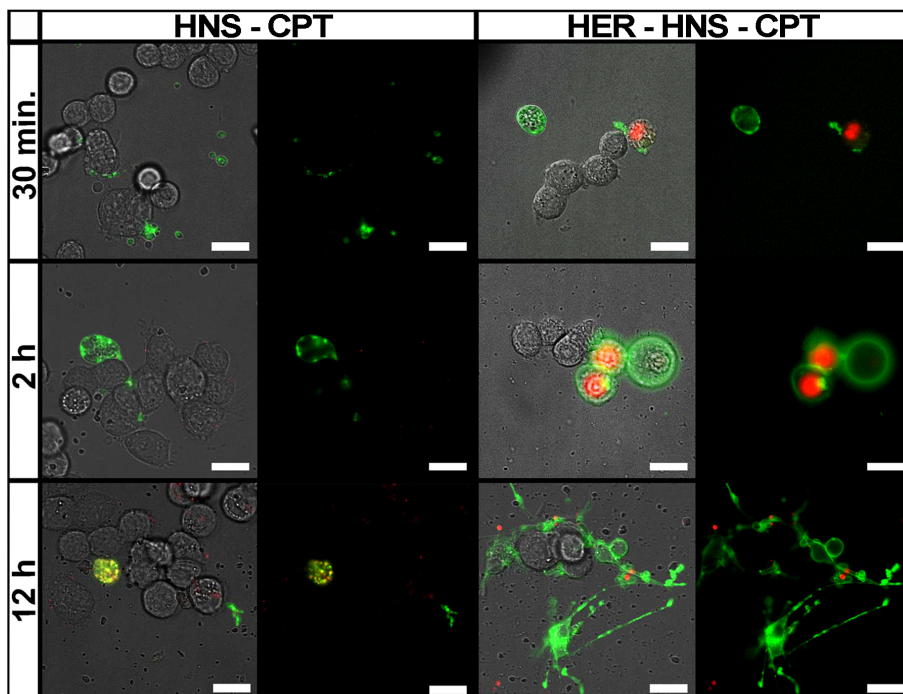


Figure 35. Live cell fluorescent images of SK-BR-3 cells treated with $10 \mu\text{g mL}^{-1}$ of HNS-CPT and HER-HNS-CPT for 30 min, 2 h, and 12 h. Cells were stained with annexin V conjugated Alexa 488 (aV; green) and propidium iodide (PI; red) for visualizing apoptosis and necrosis in cells. DIC images were obtained at the same time, corresponding to the fluorescent images (Scale bars: $20 \mu\text{m}$).

-cells broke apart into apoptotic bodies while the majority of the cells with HNS-CPT were still alive.

Flow cytometric analysis was performed for quantifying apoptotic and necrotic cells incubated with HNSs for 24 h and 48 h (**Figure 36A and B**). Statistical values were obtained from dot plots using WinMDI software, based on the aV-/PI-, (viable cell), aV+/PI- (early apoptosis), aV-/PI+ (necrosis), and aV+/PI+ (late apoptosis). Compared with HER-HNS and HNS-CPT by flow cytometry analysis, the enhanced apoptosis (23%) was achieved by HER-HNS-CPT which is over 3 fold efficient than CPT and HNS-CPT (7%) in the treatment for 24 h. In comparison with the results for 24 h, the apoptosis induced by HER-HNS-CPT for 48 h increased (from 23% to 39%), while those by CPT and HNS-CPT for 48 h remained unchanged (from 7% to 7%). These results suggest that HER-HNS with optimum size for cellular uptake (50 nm) and active targeting (herceptin) affected considerably in cancer therapy.

In order to interrogate anticancer drug delivery using HER-HNS-CPT, CPT dissolved in PBS and DMSO (20 ng mL^{-1}) was inserted on SK-BR-3 cells. In **Figure 37A**, CPT in PBS incubated cells were not stained by PI, and the cells sustained their shapes. However, cells incubated with CPT in DMSO were dual-stained with aV and PI, and shapes of the cells changed

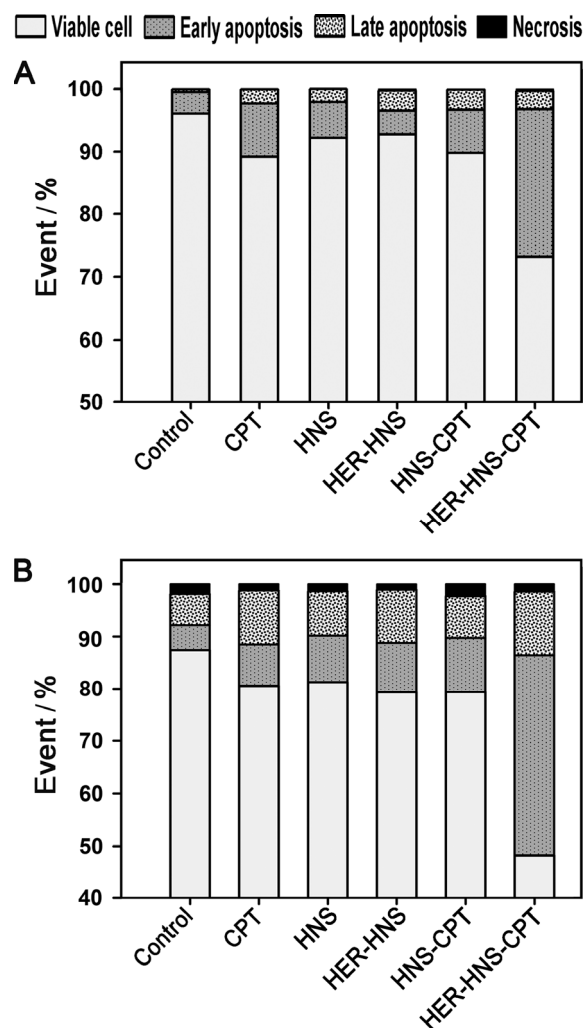


Figure 36. Quantitative assessment of apoptosis and necrosis conducted by flow cytometry analysis with aV and PI double staining. SK-BR-3 was incubated with $25 \mu\text{g mL}^{-1}$ of the nanospheres or the same concentration of CPT in PBS (50 ng mL^{-1}) for A) 24 h and B) 48 h. Each experiment was performed in triplicate.

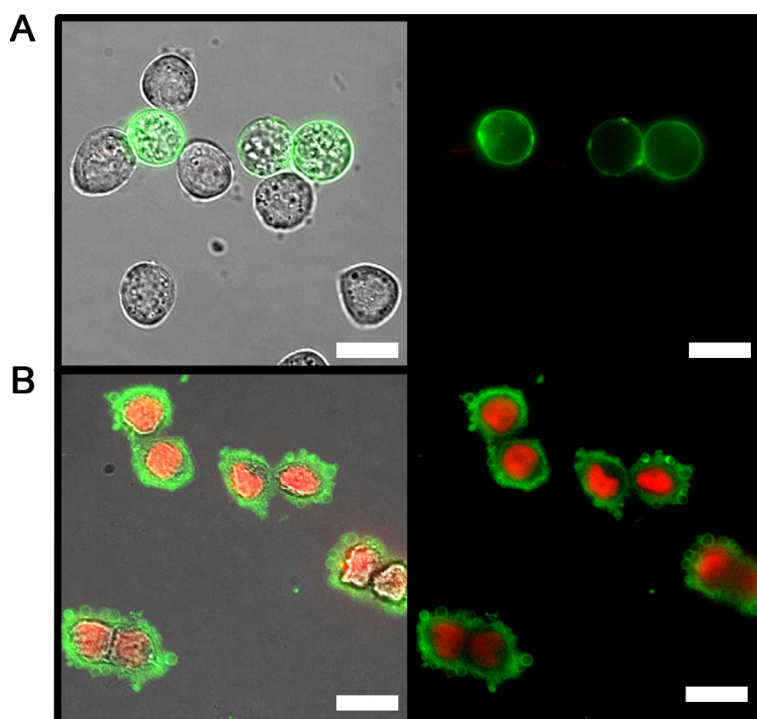


Figure 37. Live cell fluorescent images of SK-BR-3 cells incubated with A) CPT suspension in 0.1 M PBS, and B) CPT dissolved in DMSO. Apoptotic and necrotic cells were stained with aV and PI. DIC images were acquired at the same time, corresponding to the fluorescent images (Scale bars: 20 μ m).

from round to shrunken round, which indicated typical apoptosis features (**Figure 37B**). In addition, blebs on the plasma membrane were one of the characteristics to identify apoptosis. As confirmed by FACS analysis, cell death was mainly originated from apoptosis. It was ascribed to the fact that hydrophobic CPT could easily dissolve and migrate to the cells in DMSO, not in PBS. Judging from these results, CPT loaded-HER-HNS could be effective for cancer therapy capable of incorporating hydrophobic drug and delivering to the hydrophobic region of cancer cells.

To investigate cellular uptake of HNS and HER-HNS into the SK-BR-3, ultrastructural observation on the cells treated with HNS and HER-HNS were taken by TEM (**Figure 38**). Due to optimized particle size for cellular uptake, both HNS and HER- HNS were internalized into the cells. Cells still retained their shapes after internalization, which means the HNS and HER-HNS as nanocarriers were biocompatible. Interestingly, a large amount of HER-HNS was confined inside SK-BR-3 while relatively small amount of HNS was located in the cell. The nanospheres appeared to be located in vesicles, and the amount of intracellular HER-HNSs increased considerably compared with that of HNSs. It was important to note that herceptin attachment on HNSs provided efficient uptake into cancer cells.

The viability of HER-HNS-CPT was determined using human breast

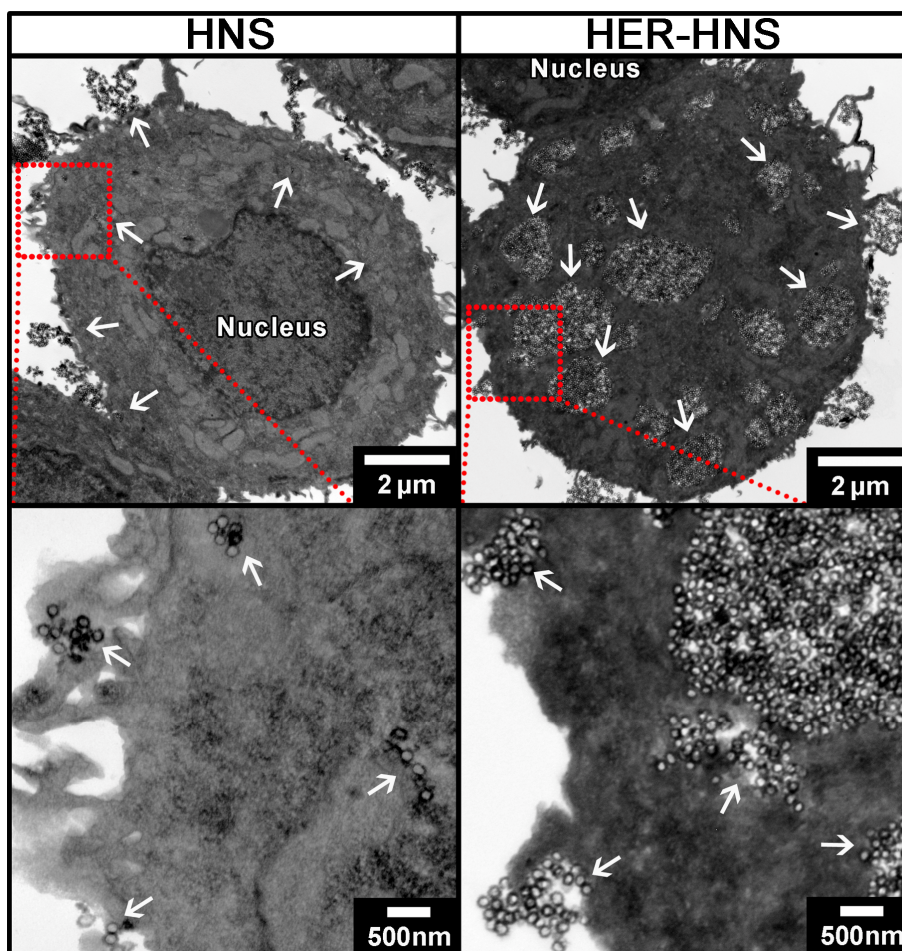


Figure 38. Cellular uptake of HNS and HER-HNS in SK-BR-3 cells ($25 \mu\text{g mL}^{-1}$) for 24 h. TEM images show HNS and HER-HNS internalized in the cells. Lower images display magnified regions bounded by red boxes in the TEM images of HNS and HER-HNS, respectively. White arrows indicate location of HNSs and HER-HNSs.

cancer SK-BR-3 and mouse macrophage RAW264.7 cells to evaluate selective cancer therapy of the HER-HNS-CPT (**Figure 39 and 40**). The production of ATP from nanospheres-treated cells was dose dependent. As the dose of the nanospheres increased, the cell viabilities decreased. In case of HNS and HER-HNS (without CPT condition), the minimum viability was over 90% in both cell lines. It means that CPT-carrier materials have no significant effects on the cell viability. At the same concentration ($100\text{ }\mu\text{g mL}^{-1}$), the viability of SK-BR-3 cells treated with HER-HNS-CPT dropped to 60% compared to those with HNS-CPT was 90%. Although cells incubated with CPT, the viability was over 80% at $100\text{ }\mu\text{g mL}^{-1}$. The differences in viability were originated from selective binding of herceptin and CPT encapsulation. These results are consistent with those of apoptosis/necrosis analysis.

In case of macrophages, different from SK-BR-3 cells, the high toxicity of CPT was observed. This is derived from hydrolyzed CPT (carboxylate form), which was cytotoxic on normal cells and less active to cancer cells [145-149]. However, CPT loaded into HNS or HER-HNS was protected by the nanocarriers, resulting in low toxicity to macrophages. In addition, the viability for SK-BR-3 cells was conducted with the drugs in different medium, DMEM which is used for RAW264.7 cells, and the results

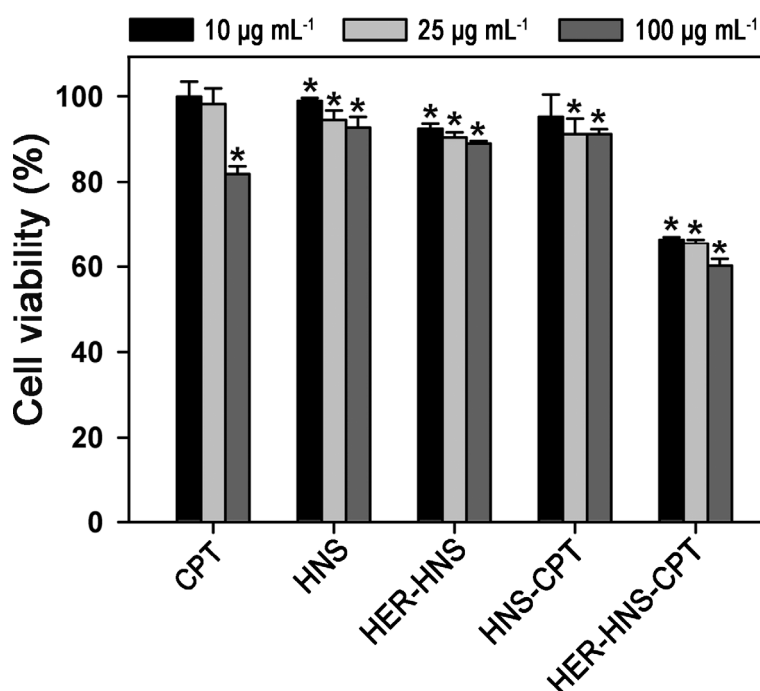


Figure 39. Viability for SK-BR-3 human breast cancer cells incubated with CPT, HNS, HER-HNS, HNS-CPT, and HER-HNS-CPT for 24 h. CPT was used at CPT-equivalent concentrations (20, 50, and 200 ng mL⁻¹). Viability was measured by quantifying the amount of ATP in metabolically active cells. Values exhibit mean \pm SD and each experiment was performed in triplicate. *Statistically significant difference from control ($P < 0.05$).

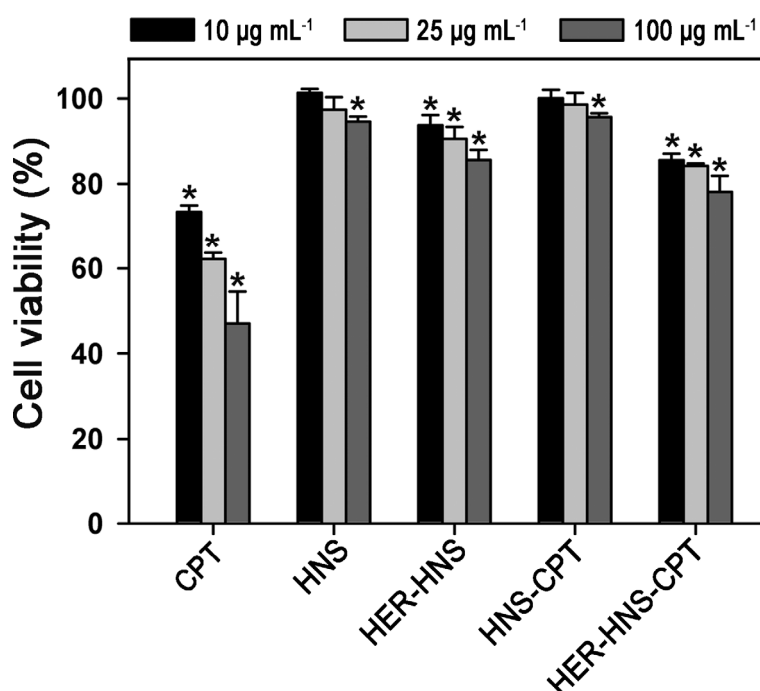


Figure 40. Viability for RAW264.7 mouse macrophage cells incubated with CPT, HNS, HER-HNS, HNS-CPT, and HER-HNS-CPT for 24 h. CPT was used at CPT-equivalent concentrations (20, 50, and 200 ng mL^{-1}). Viability was measured by quantifying the amount of ATP in metabolically active cells. Values exhibit mean \pm SD and each experiment was performed in triplicate. *Statistically significant difference from control ($P<0.05$).

showed very similar tendency to the above-mentioned results (**Figure 41**). It was noteworthy that HER-HNS-CPT demonstrated highly efficient cancer therapy and low toxicity to normal cells simultaneously [150,151].

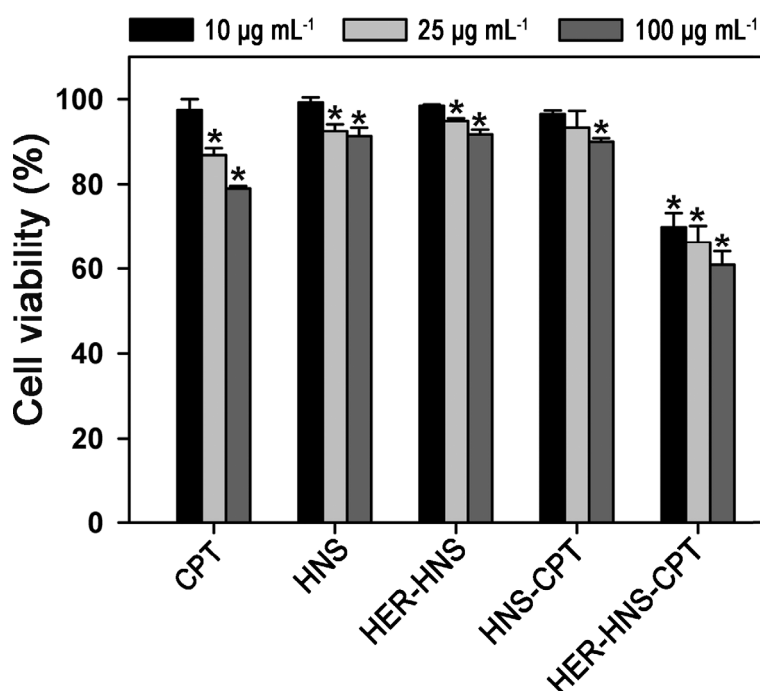


Figure 41. Viability for SK-BR-3 human breast cancer cells incubated with CPT, HNS, HER-HNS, HNS-CPT, and HER-HNS-CPT in DMEM for 24 h. CPT was used at CPT equivalent concentrations (20, 50, and 200 ng mL⁻¹). Viability was measured by quantifying the amount of ATP in metabolically active cells. Values exhibit mean \pm SD and each experiment was performed in triplicate. *Statistically significant difference from control ($P < 0.05$).

3.3 Ba-doped SiO₂/TiO₂ hollow nanospheres for efficient electrorheological fluid

3.3.1 Fabrication of Ba-doped SiO₂/TiO₂ hollow nanospheres from SiO₂/TiO₂ core/shell nanospheres

Ba-doped SiO₂/TiO₂ hollow nanospheres (Ba-HNSs) were easily fabricated from SiO₂/TiO₂ core/shell nanospheres. The SiO₂/TiO₂ core/shell nanospheres were prepared by the same method for SNTCNs except that triethylamine, nitrogen dopant was not used. Transformation from the SiO₂/TiO₂ core/shell nanospheres into the Ba-HNSs is described in **Figure 42**. In aqueous alkaline solution with sonication treatment, the SiO₂/TiO₂ core/shell nanospheres were transformed into HNSs *via* the reversible process of dissolution and re-deposition of SiO₂. Basic condition with high temperature and pressure at interface between SiO₂ core and TiO₂ shell by sonication enables the SiO₂ core to be dissolved by weakening siloxane bonds and coordinating hydroxide ion to Si atoms. In contrast, TiO₂ shell is not etched due to its chemical inertness. Dissolved SiO₂ re-deposits on the porous TiO₂ shell, and consequently, the SiO₂/TiO₂ core/shell nanospheres are transformed into HNSs, which was reported previously [142]. Simultaneously, Ba²⁺ ion can diffuse to SiO₂ and TiO₂, and then react with

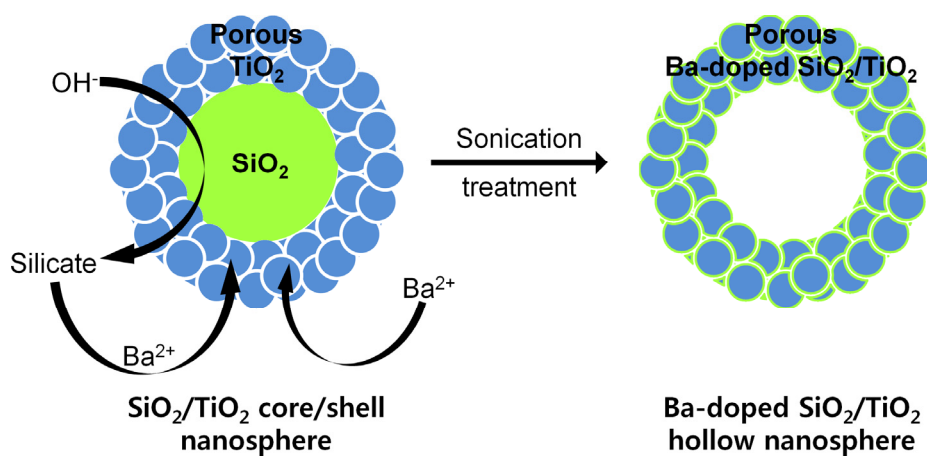


Figure 42. Schematic illustration for fabrication of Ba-HNSs from SiO₂/TiO₂ core/shell nanospheres.

them forming BaSiO_3 and BaTiO_3 under high temperature and pressure generated by sonication treatment [152-155].

Typical TEM images of the $\text{SiO}_2/\text{TiO}_2$ core/shell nanospheres and the Ba-HNSs are shown in **Figure 43**. The all $\text{SiO}_2/\text{TiO}_2$ core/shell nanospheres were in spherical shape and had an average diameter of approximately 45 nm. Rough surface of the core/shell nanospheres indicates that the shell is comprised of small TiO_2 nanoparticles and is porous in consequence. It is also confirmed by a type IV hysteresis of nitrogen adsorption-desorption isotherm of the $\text{SiO}_2/\text{TiO}_2$ core/shell nanospheres (**Figure 44**). The Ba-HNSs had spherical shape with hollow core and an average diameter of them was approximately 50 nm. The Ba-HNSs exhibited rougher surface and larger diameter, which was induced by re-deposition of SiO_2 on TiO_2 shell. A type IV hysteresis was also appeared in nitrogen adsorption-desorption isotherm of the Ba-HNSs. However, the Ba-HNSs showed increased nitrogen adsorption-desorption volume in comparison with the $\text{SiO}_2/\text{TiO}_2$ core/shell nanospheres due to hollow interior.

Although shape of the Ba-HNS is very similar to that of HNS (**Figure 45**), there is a great difference between elements constituting Ba-HNSs and HNSs. EDX analysis shows that while Ti, Si, O, and Ba elements are present in Ba-HNS, only Ti, Si, and O elements are detected in HNS (**Figure 46**),

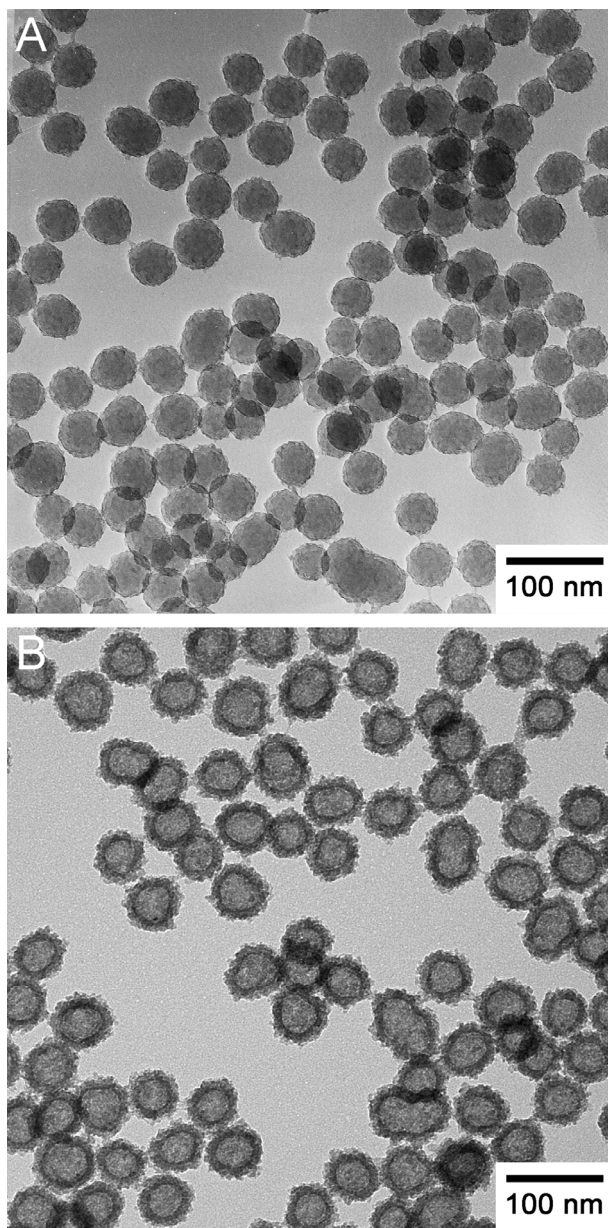


Figure 43. TEM images of (A) the SiO₂/TiO₂ core/shell nanospheres and (B) the Ba-HNSs.

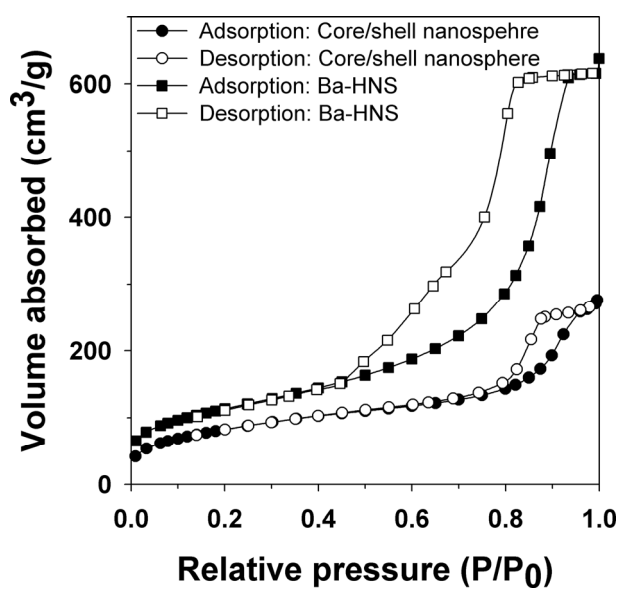


Figure 44. Nitrogen adsorption isotherm of the SiO₂/TiO₂ core/shell nanospheres and the Ba-HNSs.

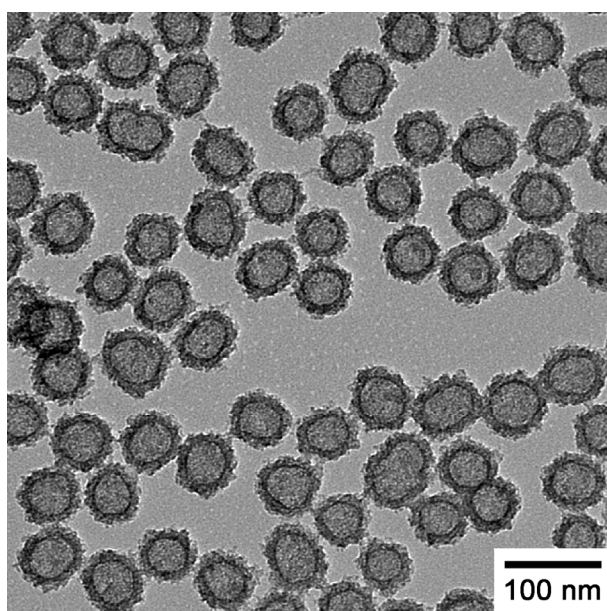


Figure 45. TEM images of the HNPs fabricated by the same method for Ba-HNSs except that Ba^{2+} ions were alternated with NH_4^+ ions.

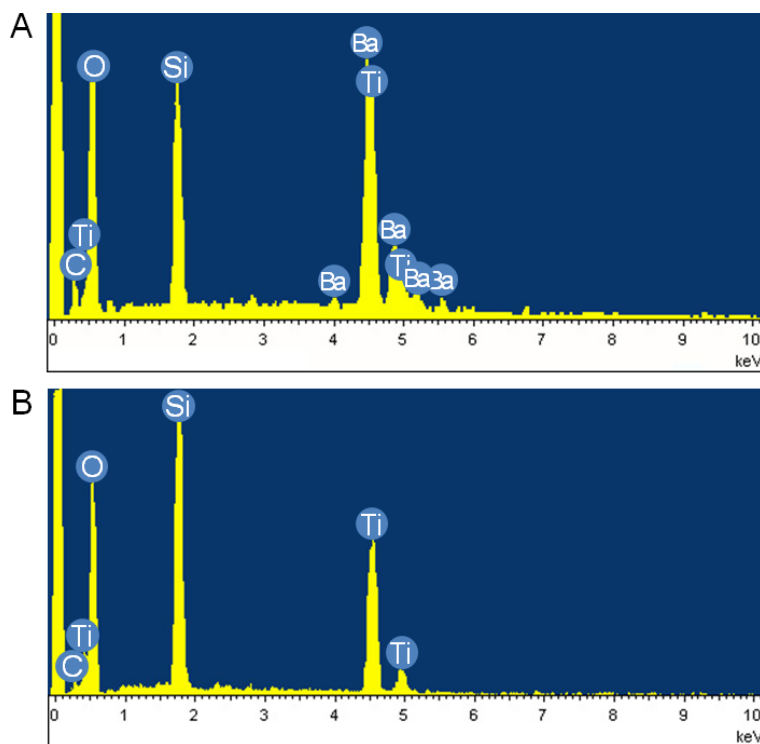


Figure 46. EDX spectra of (A) Ba-HNSs and (B) the SiO₂/TiO₂ core/shell nanospheres. The signal of carbon originated from the carbon tape to fix the samples.

and atomic ratio of Ti to Si is almost identical in Ba-HNS and HNS (**Table 4**). It means that barium was successfully doped into HNS. XRD pattern of the Ba-HNSs also confirms that they are comprised of BaTiO₃ (JCPDS Card No. 75-0211) and BaSiO₃ (JCPDS Card No. 26-1402) originated from doping barium into TiO₂ and SiO₂ respectively (**Figure 47**). The Ba-HNSs exhibit XRD pattern which includes peaks of BaTiO₃ and BaSiO₃, while the HNSs have an amorphous pattern. XPS analysis shows more apparent information about the presence of BaTiO₃ and BaSiO₃ in the Ba-HNSs. **Figure 48** exhibits full-scale XPS spectra and Ba 3d photoelectron spectra of Ba-HNSs and HNSs. Compared to the spectrum of HNSs, there are clear peaks of Ba 3d around 779.5 eV and 795.0 eV in that of the Ba-HNSs, which implies the existence of BaTiO₃ [156]. Besides the Ba 3d photoelectron spectra, Ti 2p and O 1s photoelectron spectra also indicate the presence of BaTiO₃. Only one peak of Ti 2p_{3/2} is detected at 459.1 eV in the XPS spectrum of HNSs, while large peak and small peak are detected at 458.0 eV corresponding to BaTiO₃ and 459.1 eV corresponding to TiO₂, respectively (**Figure 49**) [156,157]. This result suggests that the majority of TiO₂ are changed into BaTiO₃ during formation of hollow nanospheres from SiO₂/TiO₂ core/shell nanospheres in Ba(OH)₂ aqueous solution. O 1s photoelectron spectra of the Ba-HNSs and the HNSs support this fact.

Table 4. Elemental contents of Ba-HNS and HNS by EDX analysis. Carbon and oxygen contents were excluded because they originated from carbon tape to fix Ba-HNS and HNS.

Sample	Ti	Si	Ba
	/atomic %	/atomic %	/atomic %
Ba-HNS	36.18	33.49	30.33
HNS	50.77	49.23	0

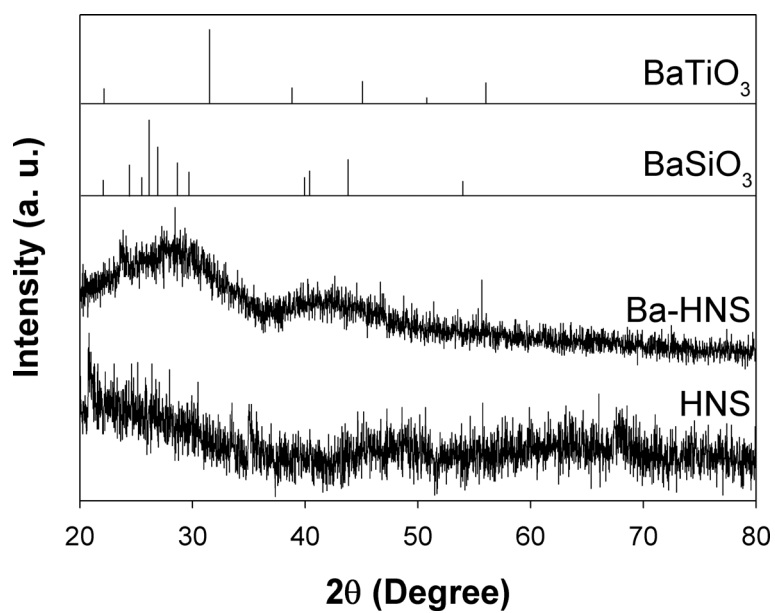


Figure 47. XRD patterns of the Ba-HNSs and the HNSs.

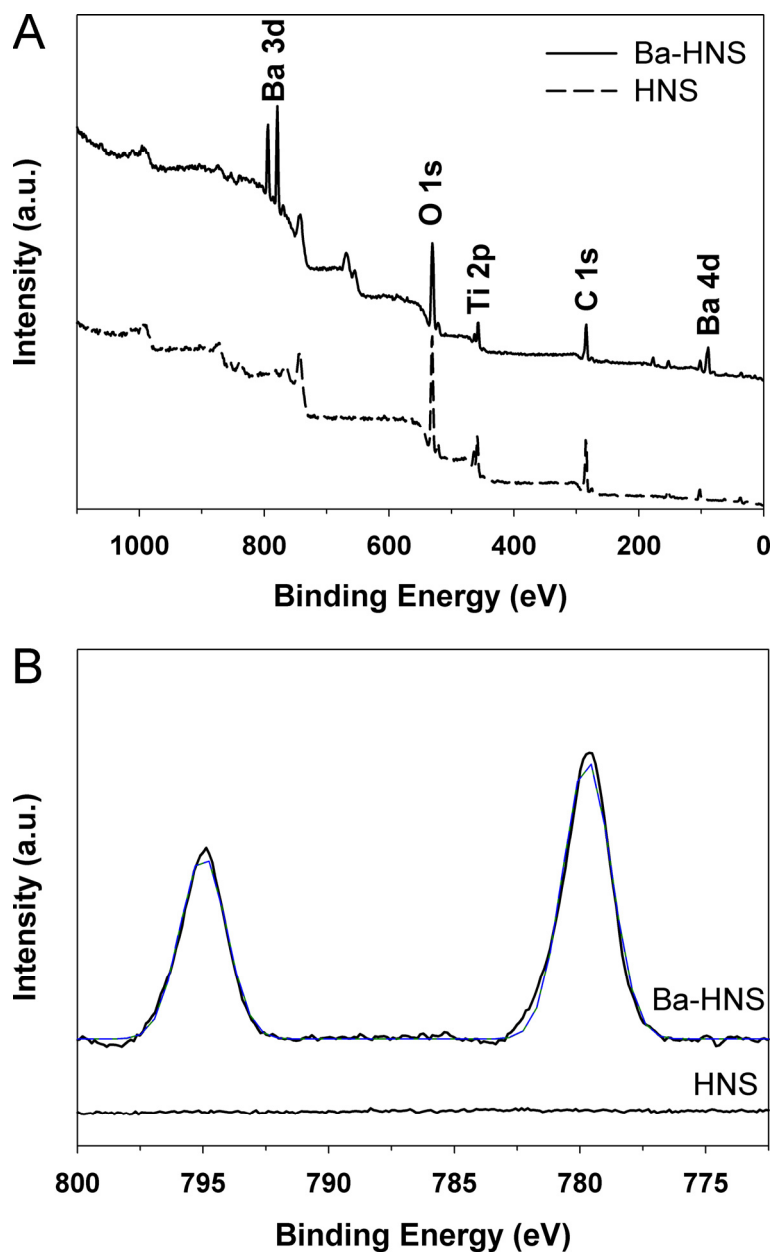


Figure 48. (A) Full-scale X-ray photoelectron spectroscopy spectra and (B) Ba 3d photoelectron spectra of the Ba-HNSs and the HNSs.

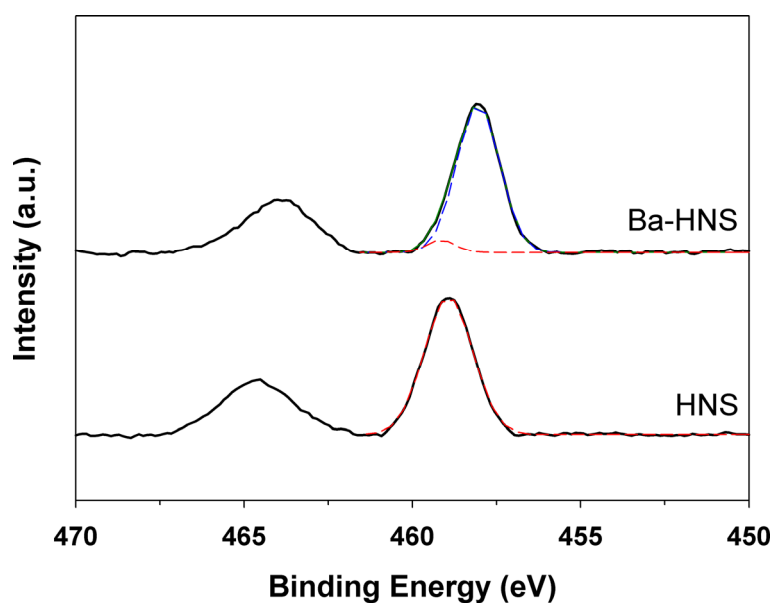


Figure 49. Ti 2p photoelectron spectra of the Ba-HNSs and the HNSs. Red and blue spectra are assigned to TiO_2 and BaTiO_3 , respectively.

Because both Ba-HNS and HNS have Ti-O-Ti, Si-O-Ti, and Si-O-Si bonds of TiO₂ and SiO₂, there are signals at 530.8 eV, 531.9 eV, and 532.6 eV (corresponding to Ti-O-Ti, Si-O-Ti, and Si-O-Si bonds in composite of TiO₂ and SiO₂, respectively) in O 1s photoelectron spectra of the Ba-HNSs and the HNSs [158]. O 1s photoelectron spectra of the Ba-HNSs show one more signal at 529.5 eV originated from BaTiO₃ (**Figure 50**). In Si 2p photoelectron spectra of the samples, the HNSs have only SiO₂ signal at 102.7 eV, while the Ba-HNSs exhibit both SiO₂ and BaSiO₃ signals at 102.7 eV and 101.6 eV, respectively (**Figure 51**) [159,160]. Considering the XPS spectra of the samples, barium was successfully doped into TiO₂ and SiO₂ during formation of Ba-HNSs from SiO₂/TiO₂ core/shell nanospheres.

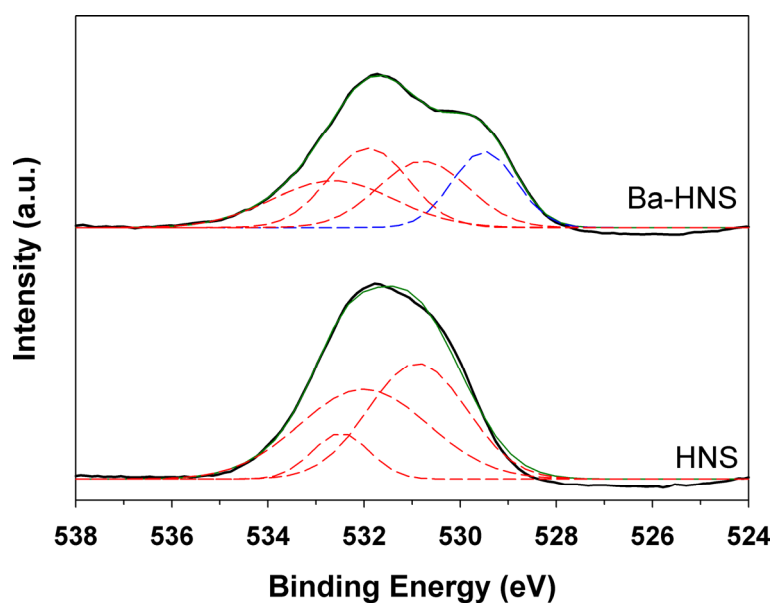


Figure 50. O 1s photoelectron spectra of the Ba-HNSs and the HNSs. Red and blue spectra are assigned to $\text{SiO}_2/\text{TiO}_2$ composite and BaTiO_3 , respectively.

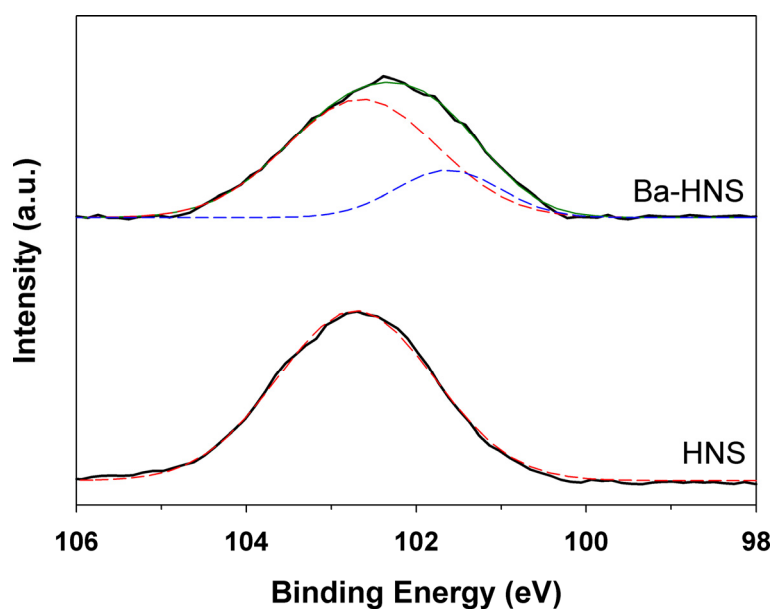


Figure 51. Si 2p photoelectron spectra of the Ba-HNSs and the HNSs. Red and blue spectra are assigned to SiO₂ and BaSiO₃, respectively.

3.3.2 Fabrication of ER fluid based on Ba-doped SiO₂/TiO₂ hollow nanospheres

ER fluids were prepared by mixing each nanostructured material including Ba-HNSs, HNSs, and commercial BaTiO₃ nanopowders with silicon oil (poly(methylphenylsiloxane)). All nanopowders were dried in vacuum oven at 60 °C for 24 h to remove moisture in pore of the nanomaterials. Volume fraction of the nanopowders in silicon oil suspension was from 5 volume percentage (vol%) to 25 vol%. **Figure 52** displays the ER fluids based on 25 vol% of Ba-HNSs and commercial BaTiO₃ nanopowders. The suspension of Ba-HNSs shows much better miscibility than that of commercial BaTiO₃ nanopowders. It was possible to increase volume fraction of the Ba-HNSs up to 25 vol%, while it was impossible for the BaTiO₃ nanopowders. It is induced by a low uniformity and a large amount of agglomeration of the commercial BaTiO₃ nanopowders (**Figure 53**), compared to those of the Ba-HNSs. Miscibilities of the HNSs with silicon oil were similar to that of the Ba-HNSs due to nearly identical shapes and textures of them.

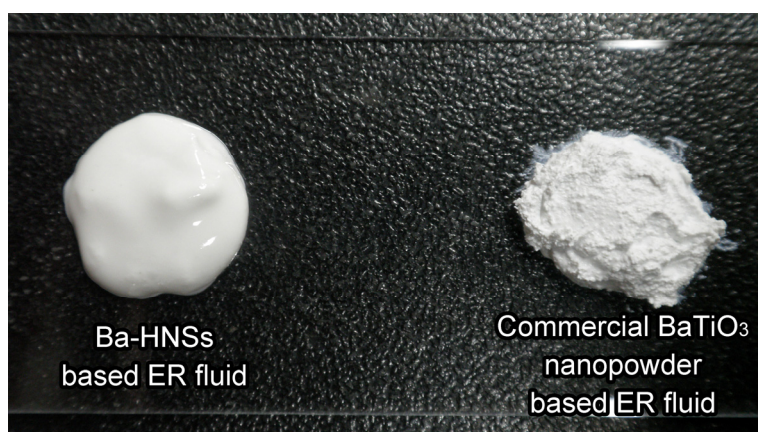


Figure 52. Photograph of ER fluids based on 25 vol% of Ba-HNSs and commercial BaTiO₃ nanopowders.

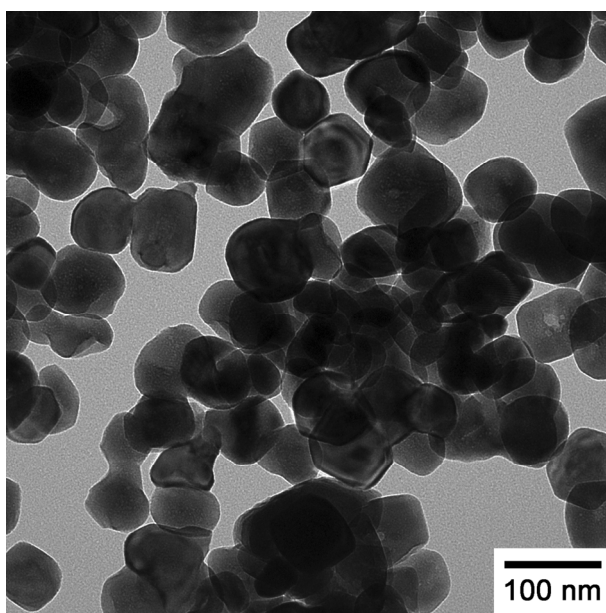


Figure 53. TEM image of the commercial BaTiO₃ nanopowders.

3.3.3 Electrorheological properties of ER fluid based on Ba-doped SiO₂/TiO₂ hollow nanospheres

The Ba-HNSs in ER fluid showed fibrous structures under electrical field in a short time. Optical microscope images of ER fluid based on Ba-HNSs exhibit this phenomenon (**Figure 54**). In the optical images, fibrous structures of Ba-HNSs were definitely shown along the applied electrical field. In a few tens of milliseconds, the randomly dispersed nanospheres transformed into the net-like and dense fibril structures, which could result in high viscosity and resulting yield stress. **Figure 55** displays the relationship of volume fraction and yield stress for ER fluids based on Ba-HNSs, HNSs, and BaTiO₃ nanopowders. With increasing volume fraction of these nanoparticles, the yield stress increased in all ER fluids. In particular, the ER fluids of Ba-HNSs and HNSs displayed dramatic increase of yield stress as a function of volume fraction of the nanospheres. Under electric field strength (5 kV/mm), the maximum shear stress values of the ER fluids based on Ba-HNSs, HNSs, and BaTiO₃ nanopowders (25 vol%) were approximately 180, 150, and 8 kPa, respectively. In particular, the ER fluid consists of Ba-HNSs exhibited the highest shear stress value. The dependency of volume fraction originated from the formation of fibril structure [161]. As the number of nanoparticles increased, the electrostatic

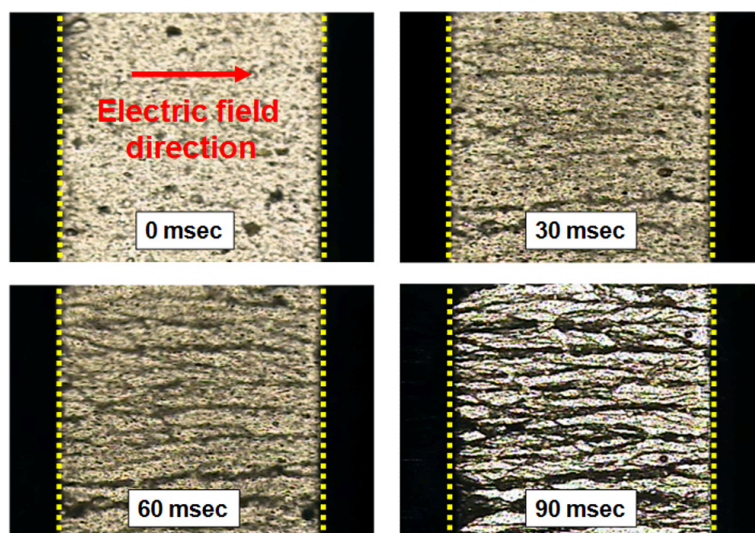


Figure 54. Microscope images of electrorheological chain formation in ER fluid of Ba-HNSs (5 vol% in silicon oil) under an applied electric field of 1 kV/mm. The gap between two electrodes was fixed to 1.0 mm.

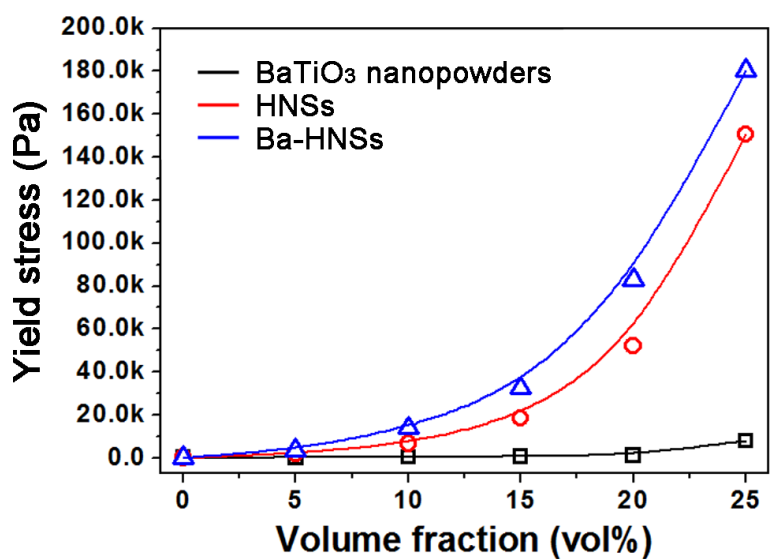


Figure 55. Dynamic yield stress as a function of volume fraction for ER fluids based on the Ba-HNSs, the HNSs and the Ba-TiO₃ nanopowders under 5 kV/mm of electric field strength. The fitting lines serve to guide the eye.

interaction between nanoparticles was improved. The suspensions with high volumetric fraction could be expected to form more dense and rigid chain-like structure, resulting high yield stress. It is noteworthy that higher volume fraction of Ba-HNSs and HNSs than 25 vol% is possible, which allows much stronger yield stress under electric field. The relationship between the shear stress and the electric field strength is also investigated (**Figure 56**). The shear stress value is directly proportional to the electric field strength. This proportional tendency is concerned with the chain-like structures formed by induced electrostatic interaction. The structural stability and the rigidity of chain-like structures are strongly affected by applied electric field strength. Under high electric field, the ER materials can be highly polarized and linked together to form the chain-like structures. Thus, highly-connected structures under high electric field provide the sufficient electrostatic interaction which counteracts the hydrodynamic force under shear flow, and possesses high shear stress value [162].

To check responsibility of ER fluids, switching the applied electric field were carried out. **Figure 57** indicates the change in the shear stress of ER fluids based on Ba-HNSs and HNSs under switching on and off electrical field. Result of the ER fluid based on BaTiO₃ nanopowders were excluded due to very low shear stress of it in comparison with the other ER

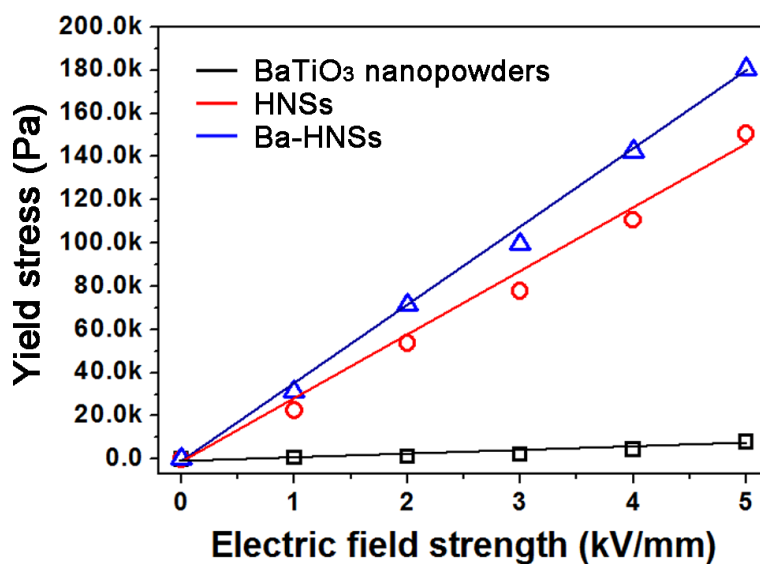


Figure 56. Dynamic yield stress of ER fluids based on the Ba-HNSs, the HNSs and the Ba-TiO₃ nanoparticles as a function of electric field strength (25 vol% in silicon oil). The fitting lines serve to guide the eye.

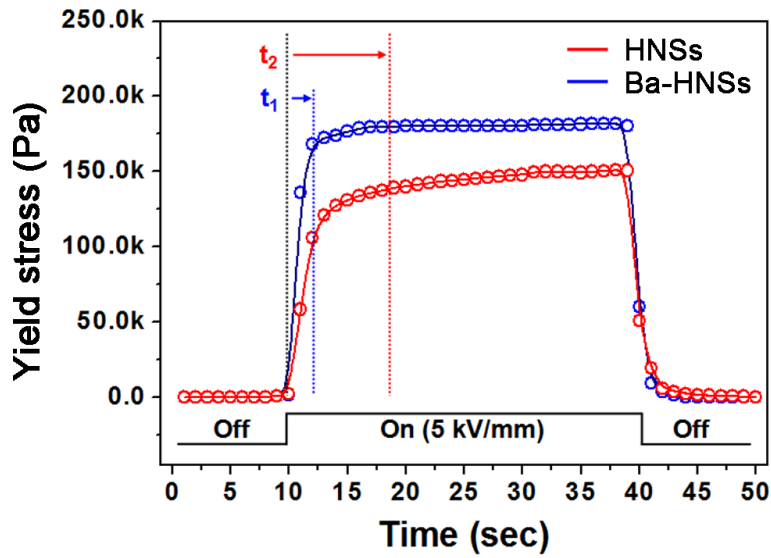


Figure 57. Change in the shear stress of ER fluids based on the Ba-HNSs and the HNSs (25 vol% in silicon oil) under switching on and off the applied electric field. Applied electric field is switched on and off alternately. t_1 and t_2 are times it takes to reach 90 % of maximum shear stress under electric field of 5 kV/mm.

fluids. In a few seconds, yield stress increased and decreased in both ER fluids with electrical on and off. Particularly, the ER fluid based on Ba-HNSs showed a rapid increase of the shear stress ($t_1 = ca. 2$ s), compared to the ER fluid based on HNSs ($t_2 = ca. 8$ s). This fast response implied that Ba-HNSs in silicon oil form fibrous structures in a short time under electric field, which is important factor to be applied for a practical use.

In evaluation of ER properties, the ER fluid based on Ba-HNSs exhibited very high shear stress, efficiency, and fast response under electric field. These superior ER properties are mainly originated from unique structure of Ba-HNSs. As mentioned above, the Ba-HNSs have porous shell consists of $BaTiO_3$, SiO_2 , and small amount of $BaSiO_3$ with high interfacial area. High surface and interface area in the Ba-HNSs produces more surface sites for charge carrier (originated from the activated pore wall, such as defects and impurities due to doping ions [163]) accumulation [164,165] and the high concentration of charge carriers at the interface or surface regions increases the interfacial polarizability of the nanospheres under high electric field, which allows higher ER activity [166,167]. For this reason, both ER fluids based on Ba-HNSs and HNSs have much stronger shear stress under high electric field than the ER fluid based on $BaTiO_3$ nanopowders. Second factor for excellent ER properties of the ER fluid based on Ba-HNSs is

intrinsic high dielectric constant of BaTiO_3 [168]. High dielectric constant is intimately associated with strong particle polarization [169,170]. The high dielectric constant of BaTiO_3 enabled the ER fluid based on Ba-HNSs to show higher shear stress and faster response under electric field, compared to the ER fluid based on HNSs.

Chapter 4 Conclusions

The suggested synthetic route, colloidal nanoparticle template approach successfully endowed various inorganic nanomaterials with deliberated nanostructure. Furthermore, prepared nanomaterials exhibited the superior property in each application field owing to customized design of nanomaterials. The subtopics could be concluded in the view point of subtopics as follows;

1. SNTCNs with uniform diameter were successfully fabricated using SiO_2 template sol-gel method. The doped nitrogen contents of SNTCNs under various synthetic conditions were investigated by XPS and DRS, and optimum condition for nitrogen doping was found. SNTCN250 prepared under this condition showed the highest nitrogen doping level and visible light absorption. In addition, the SNTCN250 has high surface area due to low calcination temperature. These characteristics provide the SNTCN250 with high photocatalytic activity for decomposition of methylene blue under visible light irradiation and TOC in comparison with P-25, commercial TiO_2 nanopowder. Through it, optimum temperature of the calcination proved to be important factor for photodecomposition activity of N- TiO_2 . In addition,

SiO₂ template sol-gel method allows mass production of SNTCNs with diverse size by changing diameter of SiO₂ template. Importantly, these SNTCNs could be used for practical applications such as coating process, polymer composites, liquid suspensions, and so on.

2. Monodisperse silica/titania hollow nanoparticles with uniform diameter of *ca.* 50 nm were successfully fabricated and modified with monoclonal antibody for active targeting. Furthermore, a large amount of hydrophobic CPT for anticancer drug was loaded into HER-HNS. Novel drug delivery strategy using the HER-HNS provides several clues about intracellular drug delivery for anticancer therapy: a) simple antibody modification, easy drug loading procedure, and high loading capacity for hydrophobic CPT, b) High selectivity for cancer cells due to herceptin conjugation on HNSs (active targeting), c) Excellent cellular internalization originated from monodispersity and optimum size (50 nm) of HNSs (passive targeting and minimizing ‘binding site barrier effect’), d) Improved delivery efficacy of CPT into cancer cells due to low drug leakage, e) Low toxicity to normal cells owing to encapsulation of CPT with HNSs. Practically, HER-HNS-CPT showed highly efficient cancer therapy and low toxicity to normal cells simultaneously. Considering these facts, drug delivery system applying

HER-HNS-CPT offers a new direction for a hydrophobic anticancer drug carrier and can be expanded to practical applications with further studies.

3. Ba-HNSs were readily synthesized from $\text{SiO}_2/\text{TiO}_2$ core/shell nanospheres by sonication-mediated etching in $\text{Ba}(\text{OH})_2$ aqueous solution. The ER fluid based on Ba-HNSs exhibited excellent ER properties including very high shear stress, efficiency, and fast response under electric field. These superior ER properties are originated from unique structure of Ba-HNSs and intrinsic high dielectric properties of BaTiO_3 in the Ba-HNSs. High surface and interface area in the Ba-HNSs produces more surface sites for charge carrier accumulation which increases the interfacial polarizability of the nanospheres under high electric field, giving higher ER activity. In addition, intrinsic high dielectric constant of BaTiO_3 in the Ba-HNSs enables the ER fluid based on Ba-HNSs to show higher shear stress and faster response under electric field.

In summary, various inorganic nanomaterials based on SiO_2 and TiO_2 were simply fabricated using colloidal nanoparticle template approach. This synthetic method was proper for controlling physical parameter. $\text{SiO}_2/\text{TiO}_2$ core/shell and hollow nanospheres were prepared for various applications

controlling their physical and chemical properties by doping, etching, sonication treatment, surface modification, etc. These nanospheres showed versatile and superior performances in many applications such as photocatalyst, drug delivery system, and ER fluid. The method for fabrication of various $\text{SiO}_2/\text{TiO}_2$ core/shell and hollow nanospheres could be utilized to synthesize other metal oxides core/shell and hollow nanospheres for many application fields including energy conversion devices, catalyst supports, nanosized reactors, chemical/bio sensors, contrast mediums, and so on.

References

- [1] G. Schmid, *Nanoparticles*, Wiley-VCH, 2004.
- [2] C. P. Poole, F. J. Owens, *Introduction to nanotechnology*, Wiley-VCH, 2003.
- [3] G. A. Ozin, A. C. Arsenault, *Nanochemistry: A Chemical approach to nanomaterials*, RSC publishing, 2005.
- [4] G. Cao, Y. Wang, *Nanostructures and Nanomaterials: Synthesis, Properties, and Applications*, World Scientific, 2010.
- [5] S. Mukhopadhyay, *Nanoscale Multifunctional Materials: Science & Applications*, Wiley, 2011.
- [6] OV Salata, *Journal of Nanobiotechnology* **2004**, 2, 3.
- [7] C. Buzea, I. Pacheco, K. Robbie, *Nanomaterials and Nanoparticles: Sources and Toxicity*, Biointerphases, 2007.
- [8] W. P. Halperin, *Reviews of Modern Physics* **1986**, 58, 533.
- [9] S. Shingubara, *Journal of Nanoparticle Research* **2003**, 5, 17.
- [10] A. Gedanken, *Ultra Sonochemistry* **2004**, 11, 47.
- [11] D. G. Shchukin, D. Radziuk, H. Möhwald, *Annual Review of Materials Research* **2010**, 40, 345.
- [12] J. Jang, *Adv. Polym. Sci.* **2006**, 199, 189.
- [13] *Colloid*, Britannica Online Encyclopedia, <http://www.britannica.com/Ebchecked/topic/125898/colloid>, 2009.
- [14] C. B. Murray, C. R. Kagan, M. G. Bawendi, *Science* **1995**, 270, 1335.

- [15] F. X. Redl, K. S. Cho, C. B. Murray, S. O'brien, *Nature* **2003**, 423, 968.
- [16] E. V. Shevchenko, D. V. Talapin, N. A. Kotov, S. O'brien, C. B. Murray, *Nature* **2006**, 439, 55.
- [17] A. E. Saunders, B. A. Korgel, *ChemPhysChem* **2005**, 6, 61.
- [18] I. Gur, N. A. Fromer, M. L. Geier, A. P. Alivisatos, *Science* **2005**, 310, 462.
- [19] D. J. Shaw, *Introduction to colloid and surface chemistry*, Butterworth Heinemann, 1999.
- [20] C. R. Martin, *Science* **1994**, 266, 1961.
- [21] V. Cepek, C. R. Martin, *Chem. Mater.* **1999**, 11, 1363.
- [22] M. Steinhart, J. H. Wendorff, A. Greiner, R. B. Wehrspohn, K. Nielsch, J. Schilling, J. Choi, U. Gosele, *Science* **2002**, 1997, 296.
- [23] L. Kicken, M. Neurock, D. Mei, *J. Phys. Chem. B* **2005**, 109, 3759.
- [24] J. Jang, B. Lim, *Angew. Chem. Int. Ed.* **2003**, 42, 5600.
- [25] J. Jang, Y. Nam, H. Yoon, *Adv. Mater.* **2005**, 17, 1382.
- [26] J. Jang, J. Ha, B. Lim, *Chem. Commun.* **2006**, 1622.
- [27] J. Jang, J. Bae, *Sens. Actuator B-Chem.* **2007**, 122, 7.
- [28] H. Yoon, M. Choi, K. J. Lee, J. Jang, *Macromol. Res.* **2008**, 16, 85.
- [29] F. Caruso, R. A. Caruso, H. Mohwald, *Science* **1998**, 282, 1111.
- [30] X. W. Lou, L. A. Archer, Z. Yang, *Adv. Mater.* **2008**, 20, 3987.
- [31] H. J. Fan, U. Gosele, M. Zacharias, *Small* **2007**, 3, 1660.
- [32] Y. Yin, R. M. Rioux, C. K. Erdonmez, S. Hughes, G. A. Somorjai, A. P. Alivisatos, *Science* **2004**, 304, 711.
- [33] T. Zhang, J. Ge, Y. Hu, Q. Zhang, S. Aloni, Y. Yin, *Angew. Chem. Int. Ed.* **2008**, 120, 5890.

- [34] X. W. Lou, L. A. Archer, Z. Yang, *Adv. Mater.* **2008**, *20*, 3987.
- [35] K. An, T. Hyeon, *Nanotoday* **2009**, *4*, 359.
- [36] J. Jang, B. Lim, *Angew. Chem. Int. Ed.* **2003**, *42*, 5600.
- [37] S. Y. Chang, L. Liu, S. A. Asher, *J. Am. Chem. Soc.* **1994**, *116*, 6739
- [38] M. Giersig, T. Ung, L. M. Liz-Marza'n, P. Mulvaney, *Adv. Mater.* **1997**, *9*, 570.
- [39] W. Tjandra, P. Ravi, J. Yao, K. C. Tam, *Nanotechnology* **2006**, *17*, 5988.
- [40] F. Ye, H. Guo, H. Zhang, X. He, *Acta Biomaterialia* **2010**, *6*, 2212.
- [41] E. González, J. Arbiol, V. F. Puntes, *Science* **2011**, *334*, 1377.
- [42] J. G. Railsback, A. C. Johnston-Peck, J. Wang, J. B. Tracy, *ACS Nano* **2010**, *4*, 1913.
- [43] R. K. Iler, *The Chemistry of Silica*, Plenum Press, 1979.
- [44] D. Zhao, J. Feng, Q. Huo, N. Melosh, G. H. Fredrickson, B. F. Chmelka, G. D. Stucky, *Science* **1998**, *279*, 548.
- [45] B. G. Trewyn, I. I. Slowing, S. Giri, H.-T. Chen, V. S.-Y. Lin, *Acc. Chem. Res.* **2007**, *40*, 846.
- [46] D. S. Shephard, T. Maschmeyer, B. F. G. Johnson, J. M. Thomas, G. Sankar, D. Ozkaya, W. Zhou, R. D. Oldroyd, R. G. Bell, *Angew. Chem. Int. Ed. Engl* **1997**, *36*, 2242.
- [47] I. I. Slowing, B. G. Trewyn, S. Giri, V. S.-Y. Lin, *Adv. Func. Mater.* **2007**, *17*, 1225.
- [48] I. I. Slowing, J. L. Vivero-Escoto, C.-W. Wu, V. S.-Y. Lin, *Advanced Drug Delivery Reviews* **2008**, *60*, 1278.
- [49] J. Jamieson, B. Olinger, *Pressure Temperature Studies of Anatase*,

- Brookite, Rutile and TiO₂ II: A discussion*, Mineralogical Notes, 1969.
- [50] N. N. Greenwood, A. Earnshaw, *Chemical Principles 6th Ed.*, Oxford: Pergamon, 2009.
- [51] D. Hanaor, C. Sorrell, *J. Mater. Sci.* **2011**, *46*, 855.
- [52] K. Hashimoto, H. Irie, A. Fujishima, *Jpn. J. Appl. Phys.* **2005**, *44*, 8269.
- [53] Md. K. Nazeeruddin, R. Humphry-Baker, P. Liska, M. Grätzel, *J. Phys. Chem. B* **2003**, *107*, 8981.
- [54] I. Robel, V. Subramanian, M. Kuno, P. V. Kamat, *Jpn. J. Am. Chem. Soc.* **2006**, *128*, 2385.
- [55] K. Shankar, G. K. Mor, H. E. Prakasham, O. K. Varghese, C. A. Grimes, *Langmuir* **2007**, *23*, 12445.
- [56] X. Chen, C. Burda, *J. Am. Chem. Soc.* **2008**, *130*, 5018.
- [57] K. Awazu, M. Fujumaki, C. Rockstuhl, J. Tominaga, H. Murakami, Y. Ohki, N. Yoshida, T. Watanabe, *J. Am. Chem. Soc.* **2008**, *130*, 1676.
- [58] N. Kakuta, N. Goto, H. Ohkita, T. Mizushima, *J. Phys. Chem. B* **1999**, *103*, 5917.
- [59] K. Katsumata, C.E.J. Cordonier, T. Shichi, A. Fujishima, *J. Am. Chem. Soc.* **2009**, *131*, 3856.
- [60] Wang, K. Maeda, X. Chen, K. Takanabe, K. Domen, K.Y. Hou, X. Fu, M. Antonietti, *J. Am. Chem. Soc.* **2009**, *131*, 1680.
- [61] S. Yuan, L. Yua, L. Shi, J. Wua, J. Fang, Y. Zhao, *Catal. Commun.* **2009**, *10*, 1188.
- [62] L. Zhang, D. He, P. Jiang, *Catal. Commun.* **2009**, *10*, 1414.
- [63] S. Guo, Z. Wu, H. Wang, F. Dong, *Catal. Commun.* **2009**, *10*, 1766.

- [64] S. G. Kumar, L. G. Devi, *J. Phys. Chem. A* **2011**, *115*, 13211.
- [65] G. S. Mital, T. Manoj, *Chinese Sci. Bull.* **2011**, *56*, 1639.
- [66] Y. N. Tan, C. L. Wong, A. R. Mohamed, *ISRN Materials Science* **2011**, doi:10.5402/2011/261219.
- [67] R. Levinson, P. Berdahl and H. Akbari, *Sol. Energy Mater. Sol. Cells* **2006**, *89*, 319.
- [68] T. Umebayashi, T. Yamaki, H. Itoh and K. Asai , *Appl. Phys. Lett.* 2002, *81*, 454.
- [69] J. Wang, T. Ma, G. Zhang, Z. Zhang, X. Zhang, Y. Jiang, G. Zhao, P. Zhang, *Catal. Commun.* 2007, *8*, 607.
- [70] X. Chen and C. Burda, *J. Am. Chem. Soc.* 2008, *130*, 5018.
- [71] Z. Zhou, J. Wang, S. Zhou, X. Liu, G. Meng, *Catal. Commun.* 2008, *9*, 568.
- [72] L. G. Devi, S. G. Kumar, B. N. Murthy, N. Kottam, *Catal. Commun.* 2009, *10*, 794.
- [73] F. Chen, W. Zou, W. Qu, J. Zhang, *Catal. Commun.* 2009, *10*, 1510.
- [74] X. Z. Li, F. B. Li, *Environ. Sci. Technol.* **2001**, *35*, 2381.
- [75] A. Yamakata, T. Ishibashi, H. Onishi, *J. Phys. Chem. B* **2002**, *106*, 9122.
- [76] D. C. Hurum, K. A. Gray, *J. Phys. Chem. B* **2005**, *109*, 977.
- [77] R. H. Müller, K. Mäder, S. Gohla, *Eur. J. Pharm. Biopharm.* **2000**, *50*, 161.
- [78] M. Vallet-Regí, A. Rámila, R. P. del Real, J. Pérez-Pariente, *Chem. Mater.* **2001**, *13*, 308.

- [79] K. S. Soppimath, T. M. Aminabhavi, A. R. Kulkarni, W. E. Rudzinski, *J. Control. Release* **2005**, *109*, 977.
- [80] D. Moinard-Checot, Y. Chevalier, S. Briançon, H. Fessi, S. Guinebretière, *J. Nanosci. Nanotechnol.* **2006**, *6*, 2664.
- [81] D. Peer, J. M. Karp, S. Hong, O. C. Farokhzad, R. Margalit, R. Langer, *Nat. Nanotechnol.* **2007**, *2*, 751.
- [82] H. J. Choi, M. S. Jhon, *Soft Matter* **2009**, *5*, 1562.
- [83] W. Wen, X. Huang, P. Sheng, *Soft Matter* **2008**, *4*, 200.
- [84] T. Hao, *Adv. Mater.* **2001**, *13*, 1847.
- [85] R. Shen, X. Wang, Y. Lu, D. Wang, G. Sun, Z. Cao, K. Lu, *Adv. Mater.* **2009**, *In press*.
- [86] X. Niu, M. Zhang, J. Wu, W. Wen, P. Sheng, *Soft Matter* **2009**, *5*, 576.
- [87] W. Wen, X. Huang, S. Yang, K. Lu, P. Sheng, *Nat. Mater.* **2003**, *2*, 727.
- [88] W. Wen, X. Huang, P. Sheng, *Appl. Phys. Lett.* **2004**, *85*, 299.
- [89] B.-X. Wang, X.-P. Zhao, Y. Zhao, C.-L. Ding, *Compos. Sci. Technol.* **2007**, *67*, 3031.
- [90] C. Burda, Y. Lou, X. Chen, A. C. S. Samia, J. Stout, J. L. Gole, *Nano Lett.* **2003**, *3*, 1049.
- [91] M. Okada, Y. Yamada, P. Jin, M. Tazawa and K. Yoshimura, *Thin Solid Films* **2003**, *442*, 217.
- [92] M. Sathish, B. Viswanathan, R. P. Viswanath, C. S. Gopinath, *Chem. Mater.* **2005**, *17*, 6349.
- [93] Y. Wang, G. Zhou, T. Li, W. Qiao, Y. Li, *Catal. Commun.* **2009**, *10*, 412.
- [94] Y. Xie, Q. Zhao, X. J. Zhao, *Catal. Lett.* **2007**, *118*, 231.

- [95] Y. Wang, L. Cai, Y. Xia, *Adv. Mater.* **2005**, *17*, 473.
- [96] G. Li, C. Liu, Y. Liu, *J. Am. Ceram. Soc.* **2007**, *90*, 2667.
- [97] X. Li, K. Lv, K. Deng, J. Tang, R. Su, J. Sun, L. Chen, *Mat. Sci. Eng. B* **2009**, *158*, 40.
- [98] B. Peng, F. Tang, D. Chen, X. Ren, X. Meng and J. Ren, *J. Colloid. Interface Sci.* **2009**, *329*, 62.
- [99] Y. Li, Z. Sun, J. Zhang, K. Zhang, Y. Wang, X. Chen, S. Zhu and B. Yang, *J. Colloid. Interface Sci.* **2008**, *325*, 567.
- [100] H. Wang, M. Zhou, F. Yang, J. Wang, Y. Jiang, Y. Wang, H. Wang and Q. Li, *Chem. Mater.* **2009**, *21*, 404.
- [101] A. L. Bodley, T. A. Shapiro, *Proc. Natl. Acad. Sci.* **1995**, *92*, 3726.
- [102] F. M. Muggia, I. Dimery, S. G. Arbuck, *Ann. NY. Acad. Sci.* **1996**, *803*, 213.
- [103] P. B. Arimondo, C. Bailly, A. S. Boutorine, V. A. Ryabinin, A. N. Syniakov, J.-S. Sun, T. Garestier, C. Hélène, *Angew. Chem. Int. Ed.* **2001**, *40*, 3045.
- [104] D. Sriram, P. Yogeewari, R. Thirumurugan, T. R. Bal, *Nat. Prod. Res.* **2005**, *19*, 393.
- [105] K. Cheng, N. J. Rahier, B. M. Eisenhauer, R. Gao, S. J. Thomas, S. M. Hecht, *J. Am. Chem. Soc.* **2005**, *127*, 838.
- [106] W. Wu, R. Li, X. Bian, Z. Zhu, D. Ding, X. Li, Z. Jia, X. Jiang, Y. Hu, *ACS Nano* **2009**, *3*, 2740.
- [107] J. Fassberg, V. J. Stella, *J. Pharm. Sci.* **1992**, *81*, 676.
- [108] M. Potmesil, *Cancer Res.* **1994**, *54*, 1431.

- [109] Z. Mi, T. G. Burke, *Biochemistry* **1994**, *33*, 10325.
- [110] G. P. Adams, R. Schier, A. M. McCall, H. H. Simmons, E. M. Horak, R. K. Alpaugh, J. D. Marks, L. M. Weiner, *Cancer Res.* **2001**, *61*, 4750.
- [111] T. M. Allen, *Nat. Rev. Cancer* **2002**, *2*, 750.
- [112] W. Jiang, B. Y. S. Kim, J. T. Rutka, W. C. W. Chan, *Nat. Nanotechnol.* **2008**, *3*, 145.
- [113] W.-K. Oh, S. Kim, M. Choi, C. Kim, Y. S. Jeong, B.-R. Cho, J.-S. Hahn, J. Jang, *ACS Nano* **2010**, *4*, 5301.
- [114] S. Kim, W.-K. Oh, Y. S. Jeong, J.-Y. Hong, B.-R. Cho, J.-S. Hahn, J. Jang, *Biomaterials* **2011**, *32*, 2342.
- [115] K. Di, Y. Zhu, X. Yang, C. Li, *J. Colloid Interface Sci.* **2006**, *294*, 499.
- [116] J. Zhang, X. Gong, C. Liu, W. Wen, P. Sheng, *Phys. Rev. Lett.* **2008**, *101*, 194503.
- [117] Y. Qiao, X. Zhao, *Colloid. Surface. A* **2009**, *340*, 33.
- [118] V. Pavlinek, P. Saha, O. Quadrat, J. Stejskal, *Langmuir* **2000**, *16*, 1447.
- [119] K. Negita, Y. Misono, T. Yamaguchi, J. Shinagawa, *J. Colloid Interface Sci.* **2008**, *321*, 452.
- [120] H. J. Choi, M. S. Jhon, *Soft Matter* **2009**, *5*, 1562.
- [121] J.B. Yin, X.P. Zhao, *Chem. Mater.* **2004**, *16*, 321.
- [122] B. Wang, X. Zhao, *Adv. Funct. Mater.* **2005**, *15*, 1815.
- [123] J.P. Zhao, *J. Phys. Chem. B* **2005**, *109*, 4824.
- [124] L. Xiang, X. Zhao, *J. Colloid Interface Sci.* **2006**, *296*, 131.
- [125] Y. Zhao, B. Wang, C. Ding, X. Zhao, *J. Appl. Polym. Sci.* **2008**, *110*, 3763.

- [126] C.H. Hong, H.J. Choi, J.H. Kim, *J. Mater. Sci.* **2008**, *43*, 5702.
- [127] Y. Cheng, X. Liu, J. Guo, F. Li, G. Xu, P. Cui, *Nanotechnology* **2009**, *20*, 055604.
- [128] R. C. Kanu, M. T. Shaw, *J. Rheol.* **1998**, *42*, 657.
- [129] J.E. Martin, J. Odinek, T.C. Halsey, R. Kamien, *Phys. Rev. E* **1998**, *57*, 756.
- [130] Y. Qi, W. Wen, *J. Phys. D: Appl. Phys.* **2002**, *35*, 2231.
- [131] W. Stöber, A. Fink, *J. Colloid. Interface Sci.* **1968**, *26*, 62.
- [132] X. Gao, Y. Cui, R. M. Levenson, L. W. K. Chung, S. Nie, *Nat. Biotechnol.* **2004**, *22*, 969.
- [133] S. C. Wuang, K. G. Neoh, E.-T. Kang, D. W. Pack, D. E. Leckband, *Biomaterials* **2008**, *29*, 2270.
- [134] L.-D. Chen, J. Liu, X.-F. Yu, M. He, X.-F. Pei, Z.-Y. Tang, Q.-Q. Wang, D.-W. Pang, Y. Li, *Biomaterials* **2008**, *29*, 4170.
- [135] H. Irie, Y. Watanabe, K. Hashimoto, *J. Phys. Chem. B* **2003**, *107*, 5483.
- [136] J. Yu, J. Wang, J. Zhang, Z. He, Z. Liu, X. Ai, *Mater. Lett.* **2007**, *61*, 4984.
- [137] X. Qui, Y. Zhao, C. Burda, *Adv. Mater.* **2007**, *19*, 3995.
- [138] R. Asahi, T. Morikawa, T. Ohwaki, K. Aoki, T. Taga, *Science* **2001**, *293*, 269.
- [139] S. S. Soni, M. J. Henderson, J. Bardeau, A. Gibaud, *Adv. Mater.* **2008**, *20*, 1493.
- [140] J. Marugan, M. Lopez-Munoz, R. Grieken, J. Aguado, *Ind. Eng. Chem. Res.* **2007**, *46*, 7605.

- [141] Y. Yao, G. Li, S. Ciston, R. M. Lueptow, K. A. Gray, *Environ. Sci. Technol.* **2008**, *42*, 4952.
- [142] M. Choi, C. Kim, S. O. Jeon, K. S. Yook, J. Y. Lee, J. Jang, *Chem. Commun.* **2011**, *47*, 7092.
- [143] T. Zhang, J. Ge, Y. Hu, Q. Zhang, S. Aloni, Y. Yin, *Angew. Chem., Int. Ed.* **2008**, *47*, 5806.
- [144] J. Lu, M. Liong, J. I. Zink, F. Tamanoi, *Small* **2007**, *3*, 1341.
- [145] C. G. Moertel, A. J. Schutt, R. J. Reitemeier, R. G. Hahn, *Cancer Chemother. Rep.* **1972**, *56*, 95.
- [146] J. A. Gottlieb, J. K. Luce, *Cancer Chemother. Rep.* **1972**, *56*, 103.
- [147] F. M. Muggia, P. J. Creaven, H. H. Hansen, M. H. Cohen, O. S. Selawry, *Cancer Chemother. Rep.* **1972**, *56*, 515.
- [148] P. J. Creaven, L. M. Allen, F. M. Muggia, *Cancer Chemother. Rep.* **1972**, *56*, 573.
- [149] B. C. Giovanella, H. R. Hinz, A. J. Kozielski, J. S. Stehlin Jr, R. Silber, M. Potmesil, *Cancer Res.* **1991**, *51*, 3052.
- [150] M. Shi, K. Ho, A. Keating, M. S. Shoichet, *Adv. Funct. Mater.* **2009**, *19*, 1689.
- [151] J. Lu, M. Liong, Z. Li, J. I. Zink, F. Tamanoi, *Small* **2010**, *6*, 1794.
- [152] G. Pfaff, *J. Eur. Ceram. Soc.* **1991**, *8*, 35.
- [153] J. G. Lisoni, C. H. Lei, T. Hoffmann, V. M. Fuenzalida, *Surf. Sci.* **2002**, *515*, 431.
- [154] S.K. Tripathy, T. Sahoo, M. Mohapatra, S. Anand, R.P. Das, *Mater. Lett.* **2005**, *59*, 3543.

- [155] J. Liu, J. Xu, R. Che, H. Chen, Z. Liu, F. Xia, *J. Mater. Chem.* **2012**, 22, 9277.
- [156] K. Mimura, K. Hiramatsu, M. Moriya, W. Sakamoto, S. Kawado, Y. Uesu, T. Yogo, *J. Nanopart. Res.* **2010**, 12, 1933.
- [157] M. C. Blanco López, G. Fournalis, F. L. Riley, *J. Eur. Ceram. Soc.* **1998**, 18, 2183.
- [158] G. Lassaletta, A. Fernandez, J. P. Espinos, A. R. Gonzalez-Elipe, *J. Phys. Chem.* **1995**, 99, 1484.
- [159] B. M. Reddy, B. Chowdhury, P. G. Smirniotis, *Appl. Catal. A-Gen.* **2001**, 211, 19.
- [160] S. Bender, R. Franke, E. Hartmann, V. Lansmann, M. Jansen, *J. Hormes, J. Non.-Cryst. Solids* **2002**, 298, 99.
- [161] Y. Cheng, X. Liu, J. Guo, F. Liu, Z. Li, G. Xu, P. Cui, *Nanotechnology* **2009**, 20, 055604.
- [162] H. Yan, Z.-J. Liao, H.-J. Mao, B. Zhang, X. Zhu, *J. Appl. Polym. Sci.* **2006**, 101, 638.
- [163] J. B. Yin, X. P. Zhao, *Chem. Mater.* **2004**, 16, 321.
- [164] W. V. Gool, *Principles of Defect Chemistry of Crystalline Solids*, Academic: New York, 1966.
- [165] D. R. Gamola, A. W. Schubring, B. L. Mueller, F. E. Filisko, *J. Mater. Res.* **1996**, 11, 144.
- [166] J. B. Yin, X. P. Zhao, *Chem. Phys. Lett.* **2004**, 398, 393.
- [167] J. B. Yin, X. P. Zhao, *J. Phys. Chem. B* **2006**, 110, 12916.
- [168] G. Arlt, D. Hennings, G. de With, *J. Appl. Phys.* **1985**, 58, 1619.

- [169] J.P. Huang, K.W. Yu, *Chem. Phys. Lett.* **2004**, 333, 347.
- [170] K. Kim, D. Stroud, X.T. Li, D.J. Bergman, *Phys. Rev. E* **2005**, 71, 031503.

초 록

어느 한 개 이상의 차원이 100 나노미터 이하인 물질을 나노물질이라 한다. 이러한 나노물질은 매우 높은 부피 대비 표면적비로 인해 독특한 성질을 갖게 된다. 나노물질의 독특한 성질은 전자기기, 광학기기, 에너지 관리, 표면 개질, 건축, 정보기술, 의학, 약학 등 여러 분야에 이용되고 있다. 따라서 지난 몇 십 년 동안 기존의 물질을 나노물질로 만들기 위한 노력이 계속되어 왔다.

최근에는 크기를 줄여 나노물질을 만드는 것보다는 나노구조체를 디자인하고 제조하는 것이 연구 주제로 각광받고 있다. 나노구조체의 제조와 디자인은 앞에서 언급한 여러 분야에서의 성능 향상뿐만 아니라 새로운 기능을 추가하는 것도 가능하다. 이러한 나노구조체 중 대표적인 형태가 코어/셀 나노입자와 중공 나노입자이다.

코어/셀 나노입자는 가운데의 코어 입자와 이를 둘러싸는 이중의 물질로 이루어진 물질이다. 코어를 코팅하는 것을 통해 콜로이드 간의 상호작용을 이해함과 동시에 이를 이용하여 콜로이드에 안정성을 조절하는 것이 가능하다. 다양한 코어물질에 이중의 적합한 물질을 입힘으로써 사용 목적에 적합한 물질을 제조할 수 있다. 코어물질을 통해 코어/셀 나노입자에 다양한 색, 형광, 자성, 약물저장공간 등을 도입하는 것이 가능하다. 그리고 코팅하는 물질을 변화시킴으로써 코어/셀 나노입자의 표면 전하, 관능기, 반응성 등을 조절할 수 있고, 이로 인해 입자의 안정성,

분산성을 향상시킬 수 있다. 이러한 이유로 코어/셀 나노입자는 여러 응용 분야에서 중요한 위치를 차지하고 있다.

중공 나노입자는 코어가 빈 공간인 코어/셀 나노입자의 특별한 한 종류이다. 중공 나노입자의 비어있는 부분은 입자의 낮은 밀도, 높은 표면적을 가능하게 하고, 또한 굴절률, 기계적 성능, 열적 내구성, 투과성 등을 조절할 수 있게 해준다. 중공 나노입자의 이러한 성질은 촉매, 코팅, 복합체, 화장품, 염료, 잉크, 인공세포, 충전제 등으로 사용하기에 적합하다. 이외에도 스마트 약물을 위한 약물 전달 물질로도 사용될 수 있다.

본 논문에서는 실리카/티타니아 코어/셀 구형나노입자와 중공 구형나노입자를 제조하고 이를 응용하는 것에 초점을 두고 있다. 콜로이드 실리카를 주형으로 이용하여 실리카/질소가 도핑된 티타니아 코어/셀 구형나노입자, 실리카/티타니아 중공 구형나노입자, 바륨이 도핑된 실리카/티타니아 중공 구형나노입자를 제조하였다. 제조된 구형나노입자들은 각각 유기물 분해를 위한 광촉매, 표적지향 약물전달체, 효율적인 전기유변유체에 응용되었다. 이들 구형나노입자들은 각각의 응용에 적합하고 최적의 성능을 낼 수 있도록 디자인되고 제조되었다.

주요어: 나노물질; 나노입자; 콜로이드; 코어/셀 구형나노입자; 중공 구형나노입자; 실리카; 티타니아; 바륨티타네이트; 광촉매; 약물전달; 전기유변유체.

학 번: 2007-23081

감사의 글

관악에 들어온 지 10년의 세월이 흘렀습니다. 10년이면 강산이 변한다는 말이 있듯이 그 동안 학교의 모습은 많이 변했습니다만, 여전히 추억이 깃든 장소는 캠퍼스 곳곳에 남아있습니다. 이 곳 서울대학교 화학생물공학부에 입학하여 대학 생활을 통해 많은 것들을 배울 수 있었지만, 대학원 생활은 학부과정에서 얻을 수 없었던 전공 지식, 인간관계, 책임감 등에 대해 배울 수 있었던 매우 소중한 배움의 장소였습니다. 짧은 글이지만 이 글을 통해서 대학원 생활에 도움을 주신 분들에게 감사를 표하고자 합니다.

우선 대학원 과정 동안 부족한 저를 열정적으로 지도하여주신 장정식 교수님께 감사 드립니다. 교수님께서 평소 강조하시고 몸소 보여주신 긍정적이고 성실한 자세와 연구에 대한 열정은 저의 앞으로의 인생에 있어 커다란 선물이라 생각합니다. 교수님의 가르침으로 인해 저는 자신감을 가지고 사회로 나갈 수 있게 되었습니다. 앞으로도 교수님의 가르침을 잊지 않고 꾸준히 정진하여 큰 인물이 될 수 있도록 노력하겠습니다. 또한 바쁘신 가운데에도 부족한 논문을 심사하여 주시고 좋은 말씀으로 지도하여주신 조재영 교수님, 김영규 교수님, 이종찬 교수님, 임순호 박사님께도 감사를 드립니다.

실험실 생활을 하면서 많은 시간을 같이 보냈던 선배•후배들에게도 고마운 마음을 표하고 싶습니다. 제가 실험실에 들어와 한 명의 연구자로 되기까지 많이 가르쳐주시고 조언을 아끼지 않으신 사수 문정이형이 기억에 남습니다. 지금은 미국에서 포닥생활을 하시고 계신 경진이형의 샤프한 모습도 생각나네요. 가끔 식 실험실 후배들을 위해 날리시던 독설이 그립습니다. 그리고 문정이형, 경진이형과 함께 99학번 트리오의 한 축을 이루셨던

진용이형, 실험실 막바지에 졸업할 때 많은 도움을 주셔서 감사합니다. 실험실 동기로서 형처럼, 때로는 친구처럼 많은 도움을 주신 완규형과 사훈이형께도 감사를 드립니다. 지금은 졸업해서 실험실에는 없지만 실험실에서 많은 시간을 같이 보내고 많은 도움을 주신 은유형, 혜영누나, 준혁이형 모두 감사한 사람들입니다. 후배들을 위해 쓴 소리를 마다 않던 주영이, 항상 열정적으로 연구하는 오석이형, 경희대에서 열심히 연구하는 경환이형 모두 고맙습니다. 회식자리에서 항상 멋진 목소리로 모두를 즐겁게 해준 예비 가수 오현택이, 재미있는 이야기로 모두를 즐겁게 해준 수다쟁이 근영이형, 형들의 짓궂은 장난을 재미있게 받아주는 뚜옹-선주 덕분에 즐거운 실험실 생활을 보낼 수 있어서 고맙습니다. 쉽지 않은 연구 주제인 염료감응형 태양전지를 같이 연구하고 저를 도와주었던 선혜, 은우형, 송희, 수임이에게도 고맙다는 말을 하고 싶습니다. 그리고 태양전지 연구에 있어 어려운 시기에 저만 먼저 졸업해서 미안한 마음이 많이 듭니다. 모두들 열심히 연구하고 있으니 좋은 결과가 나올 것으로 기대합니다. 성훈이형, 유정누나, 준섭이형, 민규, 승애, 충현, 현영, 상민, 준기, 종민, 인규, 동훈, 윤선이 모두 좋은 사람들인데 많은 이야기를 나누지는 못해서 아쉽습니다. 고분자재료실험실 같은 좋은 곳에 들어올 수 있었던 것을 행운으로 여기고 교수님과 선배들로부터 많은 것을 배우고 졸업하길 바랍니다.

짧은 기간이었지만 많은 가르침을 주셨던 성균관대의 임병권 교수님과 유태경 박사님께도 감사의 마음을 표하고 싶습니다. 임병권 교수님 밑에서 같이 생활했던 거한이와 태영이 모두 좋은 후배들이었는데, 많이 도와주지 못해 아쉽습니다. 지금처럼 계속 열정을 가지고 임병권 교수님과 유태경 박사님으로부터 많은 가르침을 받아 각자의 꿈을 이뤘으면 합니다.

대학원 생활 때문에 바빠서 자주 만나지 못하고 연락하지 못했지만 저에게 많은 힘을 주었던 고등학교 친구인 정수와 재호, 희창이에게도 고마운 마음을 표하고 싶습니다. 특히 정수와 재호는 힘들 텐데도 자주 서울에 올라와 만나러 와서 기억에 많이 남습니다. 거의 비슷한 시기에 사회에 나가게 되었는데 모두 하는 일이 잘 풀리기를 바랍니다.

좋은 실험실 후배이자 사랑하는 사람인 소진이에게는 이 글을 통해 말할 수 없을 만큼 많은 도움을 받았습니다. 같은 연구자로서 그리고 사랑하는 사람으로써 많은 조언과 따끔한 충고, 위로를 아끼지 않았고, 그로 인해 힘든 시기를 무사히 넘길 수 있었습니다. 이제부터는 제가 받았던 것 이상으로 많은 사랑과 도움을 주고 싶습니다.

마지막으로 가족들에게 감사의 글을 올리고 싶습니다. 부모님께는 특별한 감사를 드립니다. 최선을 다하고 노력하는 삶으로 항상 모범이 되시고 저를 위해 많은 희생을 해주셨기에 삶의 방향을 잃지 않고 지금까지 올 수 있었습니다. 공부를 한다는 핑계로 아직까지 제대로 효도도 못해 매우 죄송하며, 앞으로는 효자가 되도록 노력하겠습니다. 지금 자신의 꿈을 위해 바쁜 시간을 보내는 진희는 힘든 시간마다 격려를 해주었던 동생입니다. 바쁘고 힘든 시간을 보내는 동생에게 많은 도움이 되지 못해 미안한 마음이 앞섭니다. 앞으로는 형으로써 많은 도움을 주려고 합니다. 또한 항상 저를 격려해주셨던 할아버지와 할머니, 그리고 많은 친척분들께도 감사의 인사를 드립니다.

2012. 6. 20

관악을 내려가며

김찬희 드림